

國立交通大學

電子物理研究所

博士論文

微結構鐵磁系統的磁矩翻轉和磁電傳輸性質



Magnetization Reversal and Magneto-transport in
Patterned Ferromagnetic Systems

研究生：鍾廷翊

指導教授：許世英

中華民國九十八年五月

微結構鐵磁系統的磁矩翻轉和磁電傳輸性質
Magnetization Reversal and Magneto-transport in Patterned
Ferromagnetic Systems

學生:鍾廷翊

Student: Ting-Yi Chung

指導教授:許世英博士

Advisor: Dr. Shih-Ying Hsu

國立交通大學



A Dissertation

Submitted to Department of Electrophysics

College of science

National Chiao Tung University

in Partial Fulfillment of the Requirements

for the Degree of

Doctor of Philosophy

in

Electrophysics

May 2009

Hsinchu, Taiwan, Republic of China

中華民國九十八年五月

Magnetization Reversal and Magneto-transport in Patterned Ferromagnetic Systems

Student: Ting-Yi Chung

Advisor: Dr. Shih-Ying Hsu

Department of Electrophysics
National Chiao Tung University
Hsinchu 300, Taiwan

Abstract

We present the magnetization reversal and magneto-transport in patterned ferromagnetic systems where the dimensions and lateral shape of samples play significant roles.

In the investigation of micromagnetism, in-plane magnetoresistance (MR) and in-field magnetic force microscopy (MFM) on a series of permalloy (Py) planar wires were performed. Here, the wire length and thickness are kept constant, $20\mu\text{m}$ and 30nm , respectively. The width of the wire spans from 10 to $0.1\mu\text{m}$. The magneto-transport behavior and magnetic configuration are quite different regarding their widths, corresponding to the aspect ratio. For wire of large width ($w > 2\mu\text{m}$), remanent state is a multi-domain configuration, the magnetization reversal is via the well-known domain expansion and all behaviors are under expectation. We focus on the narrow wire with $w < 2\mu\text{m}$ to explore the micromagnetic configuration of the so called “single domain” wire in which the abrupt switch of magnetization reversal occurs. According to their behaviors, we catalog them into three regions. For wire with width less than $0.5\mu\text{m}$, a typical single domain state with moment along the long axis is observed. The moment barely rotates and switches suddenly to the opposite direction when magnetic field reaches the switching field. The other two kinds of wire have clear domains in both ends at remanence. When wire width is between 1.2 and $2\mu\text{m}$, both end domain regions expand to the whole volume of the wire with increasing magnetic field in the opposite direction. A 180° cross-tie like wall forms right before switching. When wire width is between 0.5 and $1.2\mu\text{m}$, the expansion of end domains does not extend to the whole volume before switching resulting in a spatial dependent in-plane MR behavior. Moreover, angular dependence of the

switching field of wires less than $1.2\mu\text{m}$ can be described using Aharoni model under the consideration of curling for the ellipsoid. When a wire width less than $0.3\mu\text{m}$, the condition for curling mode is no longer fulfilled, there are deviation at large angles. We find that the magnetization reversal for all narrower wires ($w < 1.2\mu\text{m}$) originates from the same mechanism of local nucleation and the propagation of the domain wall.

In the study of the angular dependence of Néel wall resistance, we create the centipede-like Py structure which consists of a central wire with numerous orthogonally bisecting finger wires. All Py wires were designed to have a single domain structure at remanence and high anisotropy by the geometric control. The remanent domain at the junction between the central and finger wires is determined by the anisotropy constants of both wires and hence, variable angles of Néel wall can be achieved. Developing a simple resistance-in-series model in corporation with the anisotropic MR effect, the analyses of the longitudinal and transverse MRs of the centipede-like structure give the domain wall resistance. Our results show that the Néel wall resistance is about $\text{m}\Omega$ and decreases with decreasing the relative angle between two domains.



微結構鐵磁系統的磁矩翻轉和磁電傳輸性質

學生:鍾廷翊

指導教授:許世英博士

國立交通大學電子物理所

大綱

此篇論文探討在鐵磁微結構中的磁矩翻轉和磁電傳輸性質，樣品的尺度和形狀在這些微結構中扮演著重要的角色。

在研究微磁學時，我們以平行膜面磁阻的量測和施加磁場下觀察磁區的磁力顯微來從事一系列鎳鐵合金毫微米線的磁矩翻轉研究，這一系列毫微米線的線長和厚度分別固定為 20 微米和 30 奈米，線寬則由 10 微米變化至 0.1 微米，線寬的改變將造成磁電傳輸行為和磁區結構有截然不同的結果。當線寬大於 2 微米是屬於多磁區結構，磁區翻轉是藉由已確知的磁區擴張來完成，而對應的磁相關行為也是可預期的，此篇論文將針對線寬小於 2 微米屬於所謂單一磁區的毫微米線研究其微磁結構，根據磁翻轉行為，單一磁區的毫微米線又可被區分為三種類型，當線寬小於 0.5 微米，在未達到磁瞬間翻轉場前，磁矩幾乎都平躺於長軸，只有在超過磁翻轉場後，磁矩才瞬間翻轉至反向，其餘的兩種類型，在零磁場時，線的兩端都有漩渦封閉磁區結構，對於線寬介於 1.2 和 2 微米，位於線兩端的磁區結構會隨著反向外加磁場的增加而擴及至樣品整體，在瞬間翻轉前會觀察到類似於 180 度 cross-tie 的磁區壁結構，當線寬介於 0.5 和 1.2 微米，磁區擴張則不會擴及至樣品整體，導致在樣品不同部位觀察的磁電阻行為有明顯的差異，此外，當線寬小於 1.2 微米，瞬間翻轉磁場與磁場相對毫微米線角度的相互關係可以被建構在 curling 翻轉方式的 Aharoni 模型描述，當線寬小於 0.3 微米，

由於幾何形狀已經不完全符合 curling 翻轉方式的考量，使得大角度的數據和模型有明顯的偏離，我們發現當線寬小於 1.2 微米時，磁矩翻轉都是透過局部的翻轉搭配磁區壁的移動來完成。

以我們對毫微米線的了解也進一步的研究 Néel 磁區壁電阻，我們設計了一系列類似蜈蚣的多腳樣品，包含了許多相互垂直的鎳鐵毫微米線，這些線都因幾何形狀的選擇而有單一磁區結構和高異向性。如此一來，位於兩線交錯區的零磁場下磁矩方向將決定於這兩線的異向性能比值，因此創造不同角度的 Néel 磁區壁，利用簡單的電阻串聯模型配合異向性磁阻來分析磁場平行電流和磁場垂直電流的磁阻結果，磁區壁電阻即可被估算出來。我們發現 Néel 磁區壁電阻大約是毫歐姆且隨著磁區壁兩邊磁區的相對角度變小而變小。



致 謝

向上天祈求，

心智成熟

上天賜與我一次又一次的失敗試驗

向上天祈求，

思考周全

上天賜與我一次又一次的錯誤嘗試

向上天祈求，

心平氣和

上天賜與我六年的時間磨練

六年來

要感謝的人好多好多

只好謝天了



CONTENTS

List of Tables	i
List of Figures	iii
1 Introduction.....	1
2 Theoretical Background.....	5
2-1 Energy consideration of domain formation.....	5
2-1-1 Fundamental magnetic energies.....	7
2-1-2 Domain structure in wires.....	12
2-2 Magnetization reversal in wires.....	17
2-2-1 Magnetization reversal by Uniform rotation.....	19
2-2-2 Nonuniform magnetization reversal.....	23
2-3 Magnetoresistance of ferromagnetic wires.....	25
2-3-1 Anisotropic magnetoresistance.....	26
2-3-2 Domain wall resistance.....	28
3 Experimental Details.....	34
3-1 Device fabrication.....	34
3-1-1 Photolithography.....	36
3-1-2 Electron beam lithography.....	38
3-2 Measurement techniques.....	40
3-2-1 Magnetoresistance measurement.....	40
3-2-2 Magnetic domain observation.....	42
3-3 Characteristics of permalloy ($\text{Ni}_{80}\text{Fe}_{20}$) samples.....	45
3-3-1 Magnetization hysteresis loop.....	46
3-3-2 Resistivity of permalloy wires.....	47
4 Experimental Results and Discussion.....	50
4-1 Remanent domain structure in individual wires.....	50
4-1-1 Geometrical description.....	51
4-1-2 Domain structure.....	53
4-2 Magnetization reversal in individual wires.....	55
4-2-1 Magnetoresistance and in field MFM images.....	57
4-2-2 Analysis of Magnetoresistance.....	66
4-2-3 Discussion of Magnetization reversal Mechanisms.....	70

4-3 Domain wall resistance in the centipede-like structures	85
4-3-1 Magnetoresistance	89
4-3-2 Planar Hall effect.....	93
4-3-3 Analysis of domain wall resistance	95
5 Conclusions and Future work	104
5-1 Summary.....	104
5-2 Future work.....	106



List of Tables

1 Qualitative comparison between different domain observation methods.....	43
2 Parameters of numerous samples.....	82
3 Summary of other DWMR studies.....	88



List of Figures

2-1 Domain structures related to the dimension.....	6
2-2 Demagnetizing factors of a prolate ellipsoid.....	11
2-3 Theoretical domain diagram of a prolate ellipsoid.....	14
2-4 A formation of a flux closure pattern in a rectangle.....	16
2-5 Theoretical expectation of the reversal mechanisms.....	19
2-6 Energy diagram based on Stoner-Wohlfarth model.....	22
2-7 Angular dependence of switching fields.....	24
2-8 Angular dependence of resistivities of AMR and PHE.....	28
2-9 Numerical spin orientation in a domain wall.....	29
3-1 SEM images of a typical device	35
3-2 SEM images of a typical photolithography pattern.....	37
3-3 Electron beam lithography patterns.....	39
3-4 Force diagram of MFM.....	45
3-5 Magnetization hysteresis loops of permally samples.....	47
3-6 Resistivity as a function of permalloy wire widths.....	48
4-1 The topography of our permalloy wires.....	52
4-2 Remanent domain diagram of permally wires.....	54
4-3 A SEM image of a typical permally wire device.....	58
4-4 Angular dependence of saturated sheet resistances	60
4-5 MR curves of a 10 μm wide wire.....	61
4-6 LMR curves and MFM images for a 10 μm wide wire	63
4-7 MR curves of a 0.43 μm wide wire.....	64
4-8 MR curves measured at different parts of a 0.43 μm wide wire.....	65

4-9 MR curves of a $1.9\mu\text{m}$ wide wire.....	66
4-10 Uniaxial anisotropic constants as a function of wire widths.....	68
4-11 Irreversible parts of LMR curves.....	70
4-12 In-field MFM images of a series of permalloy wires.....	71
4-13 LMR curves of wires with $w=1.2\mu\text{m}$ and $1.5\mu\text{m}$	73
4-14 LMR curves of wires with $w=0.7\mu\text{m}$ and $1\mu\text{m}$	74
4-15 In-field MFM images of a $1.3\mu\text{m}$ wide permalloy wire	77
4-16 Length occupation ratio of the end domain versus wire widths.....	79
4-17 Theoretical fit of $H_{sw}(\theta)$	82
4-18 $H_{sw}^{\theta=0}$ versus wire widths.....	83
4-19 A SEM image of one typical centipede-like sample.....	89
4-20 LMR and TMR of one centipede-like sample.....	92
4-21 TMR and PHE in low magnetic field.....	94
4-22 Saturated TMR resistance as a function of pitch widths.....	96
4-23 Domain wall profile in centipede-like samples.....	97
4-24 Angular dependence of the intrinsic domain wall resistance.....	98

1 Introduction

In recent years, a tremendous improvement has been made in the field of the fabrication of high quality thin films and multilayered magnetic materials, as well as the capability to pattern these films in nanoscale devices. This progress is geared towards novel magnetic recording media and sensors. By reducing the dimension of devices to be smaller than the mean free path, the effect of spin dependent scattering will be enhanced in transport resulting in the discovery of the giant magnetoresistance (GMR) in 1988 and subsequent the tunneling magnetoresistance in 1995. Based on these effects the sensitivity of read sensors for hard-disk recording has been greatly improved. With the ability to control the single atomic layer films, the interface anisotropy is able to overcome the demagnetizing energy and induces a stable perpendicular magnetization in the magnetic recording media. Following on the successful implementation, Hitachi introduced the first terabyte hard drive making a milestone for the industry in 2007. Besides a major step forward in the magnetic hard disk drives, there is a race to develop the magnetic random access memory (MRAM) due to the potential advantages such as low power consumption, fast random access, high storage density, infinite endurance, and non-volatility. Several leading semiconductor companies continually develop their MRAM circuits. The MRAM product, a 4-Mbit stand alone memory, was commercialized by Freescale in 2006. The electromigration due to the high current density for writing fields and the coupling of the stray fields in high dense arrays may be lead to failure in programming. Subsequently in order to solve the writing problem in MRAM, a new root for writing magnetic information is proposed according to the spin transfer effect. The magnetization orientation could be controlled by direct transfer of spin angular

momentum by a spin polarized current. The amplitude of the spin torque is proportional to the injection current density, so that the writing current decreases with increasing the storage density. This is an important advantage of spin transfer over field-induced writing. This topic has attracted much attention in the recent years. The world's two largest memory chip manufacturers, Samsung and Hynix, have agreed to join hands to develop the next generation of MRAM, Spin Transfer Torque MRAM (STT-MRAM) in 2008. On the other hand, in order to achieve a high storage density, the dimensions of a single storage cell must be reduced to the micrometer or even nanometer scale. As a result, this advancement in the technology has encouraged a large number of fundamental studies designed to further understand the novel physical phenomena of the micromagnetism when the dimensions of a magnetic system are reduced to approach certain characteristic lengths. Many of these characteristics are governed by minimization of total energy under the consideration of domain size, domain wall (DW) width, and exchange length. Therefore the identification of the magnetic configuration of ferromagnetic elements in the micrometer and the nanometer lateral length scales, as well as the investigation of their associated dynamic behavior, have been intensively studied in the last decade. Furthermore, the spin transfer effect in domain wall motion induced by short pulse current is regarded as a method of improving the power dissipation in MRAM. However, the intrinsically spin-dependent scattering when the conduction electrons pass through a domain wall is still ambiguous. The sign and magnitude of the resistance due to the DW are still under controversy.

The aim of this thesis is to investigate the effect of reduction in dimensions of wires on the equilibrium magnetic configuration in the presence of magnetic field, together with the effect on magnetic switching behavior. In an enable experimental

access of the magnetic configuration, spatially resolved magnetic techniques were employed. To conduct the investigation in the magnetization reversal, low temperature magnetotransport measurements were carried out. Consequently, according to the results of the individual wire, a novel centipede-like pattern was created to explore the intrinsically spin-dependent scattering when conduction electrons pass through the domain wall regimes.

This thesis is organized as follows:

In **Chapter 2**, we introduce the domain theory starting from the basically magnetic energies. For planar wires, the evolution of domain structures with varying dimension is discussed theoretically based on two kinds of approximations, elliptical shape and two dimensional thin film. Consequently, the theoretical predictions of the magnetization reversal for a single domain sample are given. Finally, several theories about the domain wall scattering are mentioned.

Chapter 3 gives a brief description of the fabrication of our samples, including two kinds of lithography. The employed experimental setups about the low temperature magnetoresistance measurement and the magnetic force microscopy are introduced in the end of this chapter. The principle of the spatially resolved magnetic technique used to directly observe domain structure is described.

Experimental results about three related topics are reported in **Chapter 4**. In the first part of this chapter, the influences of geometrical factors on the remanent domain structure for planar wires are presented. The domain structure diagram is compared with the expectation of domain theory. The investigation of the magnetization reversal for planar wires using magnetotransport measurements and domain images is demonstrated in the second part of this chapter. Magnetoresistance is analyzed in detail to explore the magnetization reversal mechanism and the switching behavior. At

the end of this chapter, a centipede-like pattern is created to study the dependence of the intrinsic domain wall resistance on the spatial variation of moments in domain walls. The magnetoresistances and the Planar Hall resistance for this pattern are shown. Subsequently, a simple resistance-in-series model is developed to estimate domain wall resistances.

The thesis closes with a summary of the study together with a recommendation of potential future work in **Chapter 5**.



2 Theoretical Background

In this chapter, we first introduce domain formation of a wire according to the energy consideration. The fundamental magnetic energies and how to arrange the magnetization in the constraint of the lowest total energy are discussed. Magnetization reversal for a wire is theoretically expected to be completed via several modes. That is strongly influenced by the dimensions and the lateral shape of samples. These modes will be presented in the second part of this chapter. Then, how these modes influence transport properties are mentioned, especially on two major magnetoresistance effects.

2-1 Energy consideration of domain formation

Magnetic domain is one region which has a uniform arrangement of magnetic moments. This idea was first postulated by Weiss [1] although the term “domain” was not introduced until much later [2]. Essentially, this idea was brought up to explain why the some tens of MOe molecular field does not fully saturate the material, as well as why ferromagnetic materials can simultaneously have zero average magnetization and non-zero local magnetization. To answer this requires the assumption that the sample was made up of various uniform magnetic regions, called “domains”.

A stable magnetic domain is the state with the lowest energy. In other words, a competition of energies determines the final configuration. The essential origins of energies are considered from the intrinsic properties of the material, such as the saturation magnetization and the structure of the crystal. These can be manipulated by the deposition processes. In addition, the size and the shape of a sample also play important roles as the dimensions are comparable to certain characteristic lengths. For example, magnetic free poles can be ignored in a ferromagnetic disk of infinite

diameter. Because of the existence of ferromagnetic exchange coupling between spins, the spins naturally arrange themselves in the same direction, forming a single domain. However, as the diameter decreases, an increase in the magnetic free poles at the disk boundary causes the system energy to increase. In order to effectively lessen the density of the free poles, the formation of the multi-domain is necessary thereby reducing the system energy. When the disk size decreases to the domain size ($\sim\mu\text{m}$), but is still larger than the domain wall width ($\sim\text{nm}$), the closure configuration will be in the most stable state which is called the vortex state. As the disk size is reduced to below the domain wall width, the single domain state will reoccur. This sample size induced domain structure transition is illustrated in Fig. 2-1. As for a rectangle, when the width decreases to the domain size, the domain structure will be transited from multi-domain to the closure domain. This structure is similar to the vortex but has domains and domain walls because the magnetic moment favors to lie with straight edges.

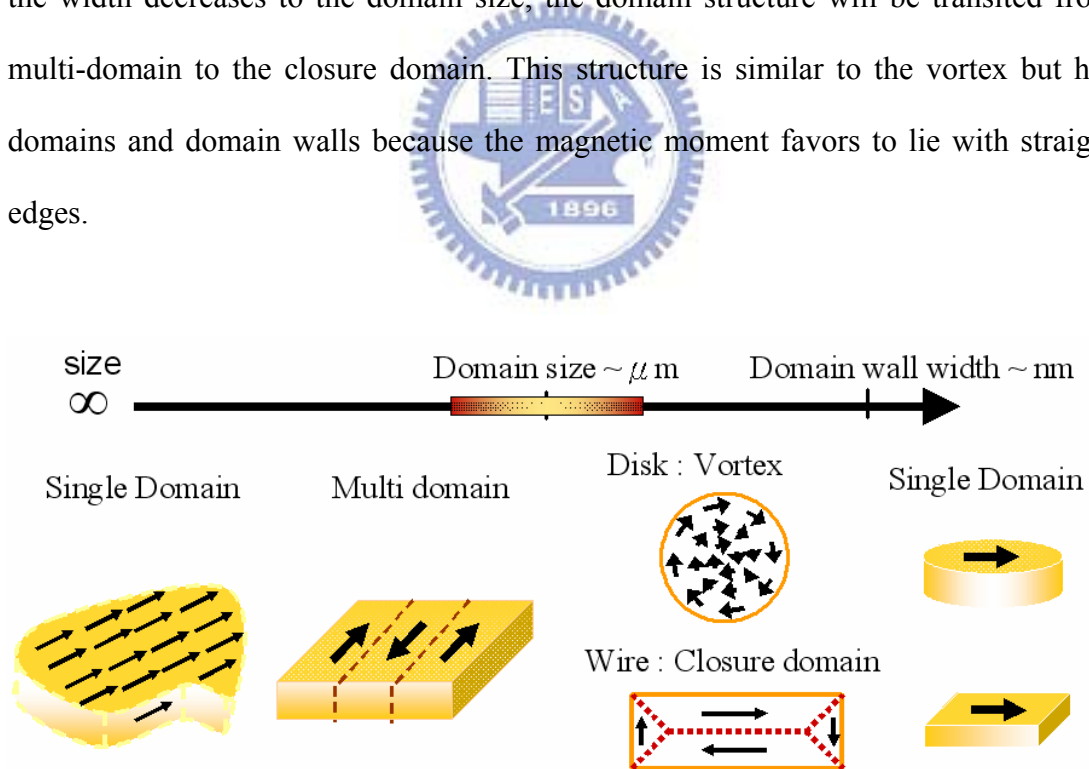


Fig 2-1: Schema of domain structure related to the dimensions of a disk and a wire.

2-1-1 Fundamental magnetic energies

In this section, several magnetic energies are introduced [1], including exchange (E_{ex}), magnetostatic (E_{mag}), anisotropy (E_{ani}), and Zeeman (E_Z). In principle, domain formation results from the competition between these energy terms and magnetization hysteresis loop can be calculated by minimizing the sum of these energies.

Exchange energy

The origin of E_{ex} is the spin-spin and spin-orbital interactions. The sum of all interactions is reduced using symmetry rules and orbital overlap to generate an effective spin-spin interaction. The exchange interaction is in short range and assumes that only interactions with the nearest neighbors are important. E_{ex} can be described in terms of the exchange constant C . The energy per unit volume can be determined for a specific crystal lattice using:

$$E_{ex} = C \int_{-\infty}^{\infty} \frac{1}{2} [(\vec{\nabla} m_x)^2 + (\vec{\nabla} m_y)^2 + (\vec{\nabla} m_z)^2] dv \quad (2-1)$$

where $C = 2JS^2c/a$, J is the exchange integral linking the atomic spins S and a is lattice constant. $\vec{M} = m_x \hat{i} + m_y \hat{j} + m_z \hat{k}$ is the magnetization vector. For ferromagnetic materials, J is positive and the lowest energy state occurs when the spins are parallel to each other. c is a geometric factor associated with the crystal structure of the material ($c = 1$ for S.C., $c = 2$ for B.C.C., $c = 4$ for F.C.C., $c = 2\sqrt{2}$ for H.C.P.).

If one ferromagnet is in contact with another, an exchange interaction may couple these two media. The coupling strength can not be derived from the bulk properties, but depending on the interface. This interfacial exchange energy can be in

comparison with the bulk exchange and can be described by the following expression:

$$E_{ex} = sC_1(1 - \vec{m}_1 \cdot \vec{m}_2) + sC_2[1 - (\vec{m}_1 \cdot \vec{m}_2)^2] \quad (2-2)$$

Here \vec{m}_1 and \vec{m}_2 are the unit magnetization vectors of two materials at the surface, C_1 and C_2 are the coupling constant [3]. s is the area of the interface. This energy plays an important role only in the multilayer and trilayer systems [4].

Anisotropic energy

From classical point of view, the spin of each atom is isotropic and hence, its energy does not depend on the direction in space. In reality, most spins may lie along a preferable direction, especially for some magnetic materials. The energy of a ferromagnet may depend on the direction of the magnetization relative to the structural axes of the material and is called as the anisotropic energy. This energy could be classified to crystalline anisotropy and induced anisotropy. The latter describes the effects of deviations from ideal symmetry as for example because of lattice defects or partial atomic ordering. The former results from spin-orbital interaction which depends on the crystal structure. Because of the arrangement of atoms in crystalline materials, on certain axes, overlapping by the electron clouds is more serious. On these axes, the stronger spin-orbital interaction causes the crystalline fields to be created and the magnetization along certain orientations is energetically preferred. In the case of a simple cubic crystal, the crystal anisotropic energy (E_{cry}) can be written as:

$$E_{cry} \approx \nu K_1[m_x^2 m_y^2 + m_y^2 m_z^2 + m_x^2 m_z^2] + \nu K_2 m_x^2 m_y^2 m_z^2 \quad (2-3)$$

where K_i is the crystalline anisotropy constant for the i th term, ν is the volume of the body. The value of constant K_i is almost in the range of 10^5erg/cm^3 for different

materials. $K_I > 0$ for Fe, the easy axes along (100), while $K_I < 0$ for Ni and the easy axes are along the body diagonals (111).

Another anisotropic energy term applies only to the surface magnetization was first introduced by Néel [5]. In a structurally isotropic medium, the surface anisotropy energy (E_s) can be expressed to first order as:

$$E_s = \nu K_s [1 - (\vec{m} \cdot \hat{n})^2] \quad (2-4)$$

where \hat{n} is the surface normal and \vec{m} is the unit magnetization vector at the surface. The order of magnitude of coefficient K_s is between 1 and 0.1 erg/cm² [6]. For bulk samples, the effect of surface anisotropy is negligible because the surface magnetization is coupled by exchange forces to the bulk magnetization. It becomes important for thin film and nanoparticle systems.

External field (Zeeman) energy

E_Z is simply the energy of the magnetization in an externally applied magnetic field. This energy has its minimum when the magnetization is along the external field and can be expressed as:

$$E_Z = - \int \vec{M} \cdot \vec{H}_{external} dv \quad (2-5)$$

Stray field (demagnetizing) energy

The origin of the E_{mag} is the dipole-dipole interaction. For certain uniform magnetic bodies, they must have magnetic fluxes of M that terminate on their surfaces. From the Maxwell's equations, the stray field (or the demagnetizing field H_d) will be generated by the non-zero divergence of the magnetization M . This energy can be given by:

$$E_{mag} = -\frac{1}{2} \int_{sample} \vec{M} \cdot \vec{H}_d dv \quad (2-6)$$

This energy is positive and the integral expresses the energy of a dipole Mdv in the field H_d created by the other dipole. The factor of 1/2 is there to keep off double counting over the dipoles.

In a uniformly magnetized ellipsoid, the demagnetizing field H_d is uniform and linearly related to the magnetization by the symmetrical demagnetizing tensor N_d , namely, $H_d = -N_d M_s$. N_d can be diagonalized if the magnetization points to a principle axis. For a general ellipsoid with $a > b > c$, where a , b , and c are the ellipsoid semi-axes, the demagnetizing factors along the semi-axes are N_a , N_b , and N_c , respectively. The demagnetizing factor N_a is given by the integral [7]:

$$N_a = 2\pi abc \int_0^\infty [(a^2 + \eta)\sqrt{(a^2 + \eta)(b^2 + \eta)(c^2 + \eta)}]^{-1} d\eta \quad (2-7)$$

η is an arbitrary variable. Analogous expressions apply to N_b and N_c . The sum of all three factors is always equal to 4π .

◆ Sphere ($a = b = c$). $N_a = N_b = N_c = 4\pi/3$ (2-8)

◆ Prolate ellipsoid ($a \gg b = c$). This ellipsoid is often seen as an approximation for a nanowire with circular cross section. When the aspect ratio is defined as $m = a / c$, its demagnetizing factors are given by

$$N_a = 4\pi \frac{1}{m^2 - 1} \left[\frac{m}{2(m^2 - 1)^{1/2}} \ln\left(\frac{m + (m^2 - 1)^{1/2}}{m - (m^2 - 1)^{1/2}}\right) - 1 \right] \quad (2-9)$$

$$N_b = N_c = 4\pi \frac{m}{2(m^2 - 1)} \left[m - \frac{1}{2(m^2 - 1)^{1/2}} \ln\left(\frac{m + (m^2 - 1)^{1/2}}{m - (m^2 - 1)^{1/2}}\right) \right]$$

◆ Slender ellipsoid ($a \gg b > c$). This ellipsoid is often seen as an approximation for nanowires deposited into templates with noncircular cross sections. Its demagnetizing factors are given by

$$\begin{aligned}
 N_a &= 4\pi \left(\frac{bc}{a^2}\right) \left[\ln\left(\frac{4a}{b+c}\right) - 1\right] \\
 N_b &= 4\pi \left(\frac{c}{b+c}\right) - \frac{1}{2} \left(\frac{bc}{a^2}\right) \ln\left(\frac{4a}{b+c}\right) + \frac{bc(3b+c)}{4a^2(b+c)} \\
 N_c &= 4\pi \left(\frac{b}{b+c}\right) - \frac{1}{2} \left(\frac{bc}{a^2}\right) \ln\left(\frac{4a}{b+c}\right) + \frac{bc(b+3c)}{4a^2(b+c)}
 \end{aligned} \tag{2-10}$$

Because the demagnetizing energy is strongly influenced by the shape and has a uniaxially anisotropic character, it is often called shape anisotropy. Fig. 2-2 shows the calculation of the demagnetizing factors of the prolate ellipsoid which is dependent on the aspect ratio. When the nanowire has the high ratio of wire length to radius, it can be approximately regarded as the prolate ellipsoid with the high aspect ratio. In this case, the demagnetizing factor along the hard axis, perpendicular to the wire axis, equals 2π , and the demagnetization factor along the easy axis, parallel to the wire axis, is 0. Thus, the difference of the shape anisotropic energy between the two axes is πM_s^2 .

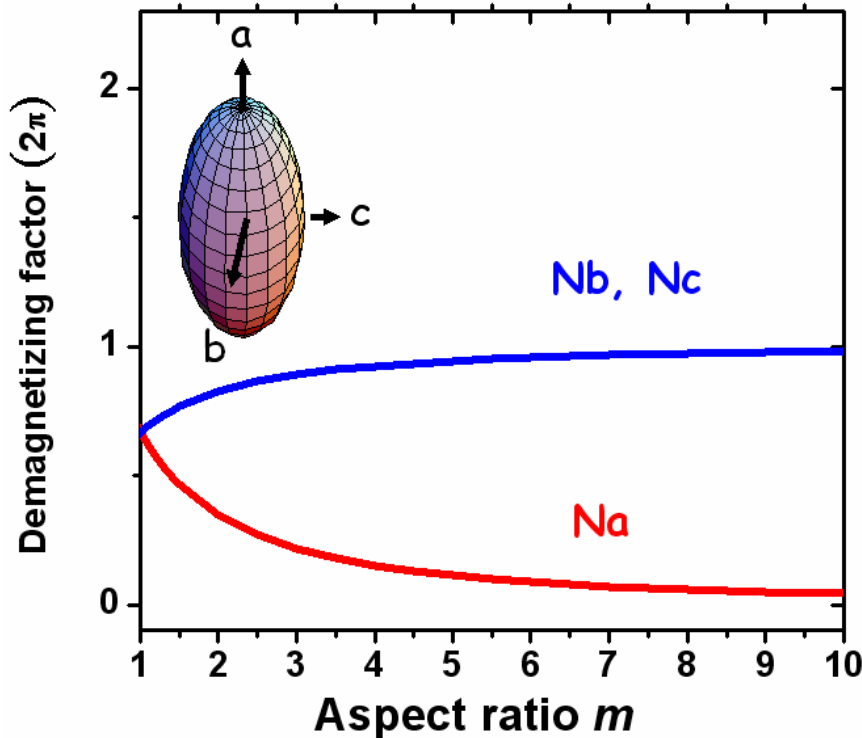


Fig 2-2: The demagnetizing factor N_d of a prolate ellipsoid as a function of its aspect ratio.

2-1-2 Domain structure in wires

In this section, we discuss remanent domain structure of a wire under the consideration of minimizing the total energy. If the entire magnetization of a wire is uniformly aligned with the long axis, which is also the easy axis of the crystalline anisotropy, the exchange and the crystalline anisotropy energy are both zero. The magnetostatic energy is maximized since the magnet acts like a single giant dipole. In order to minimize the total energy, a reduction of the magnetostatic energy is necessary and hence, the closure domain forms naturally. Both anisotropy and exchange energies increase due to the domain wall regions but the magnetostatic energy decreases significantly. It seems that the total energy can be further reduced by the formation of an additional domain, but at cost of an increase in the other energy. The formation of domain structure is strongly influenced by the dimensions and the shape of a wire. Later, we discuss theoretically domain structure of a wire by an approximation of a prolate ellipsoid with geometrical factors of a wire. For a prolate ellipsoid, the boundary between single domain and non-uniform states can be analytically determined. As for the case of a thin film element with sharp corners, we discuss domain structure based on the two dimensional approximation in theoretical aspect.

Prolate ellipsoidal approximation

We regard a wire as a prolate ellipsoid and initially assume that the entire magnetization is aligned uniformly with the long axis, which is also the easy axis of the crystalline anisotropy. The magnetostatic energy calculated by Eqs. (2-6) and (2-9) can be written as:

$$E_{uniform} = E_{mag} = \frac{1}{2} N_a M_s^2 v \quad (2-11)$$

where v is the volume. When the magnetization is non-uniform, it is difficult to evaluate the magnetostatic energy exactly, but it may often be sufficient to have a reliable estimate for its value between two bounds. Brown has devised a rather general method for finding both upper and lower bounds [1,8]. To obtain such a lower bound, the magnetostatic energy is replaced by

$$E_{mag} \geq E_{LB} = \int_{sample} \vec{M} \cdot \nabla \Phi \, dv - \frac{1}{8\pi} \int_{space} (\nabla \Phi)^2 \, dv' \quad (2-12)$$

M is the actual distribution for which the magnetostatic energy is to be calculated and the $H'' = -\nabla \Phi$ is the true field due to some other distributions. Φ is the scalar potential. The first integral is over the ferromagnetic body and the second integral is over the whole space. This expression was proven to be smaller than the actual magnetostatic energy of any distribution. It provides a lower bound to the magnetostatic energy of a given magnetization distribution M , in terms of an arbitrary field H'' . Here we choose H'' as the field of a uniformly magnetized ellipsoid and lead to

$$E_{LB} = \frac{1}{2} v M_s^2 [N_a \langle m_a \rangle^2 + N_b \langle m_b \rangle^2 + N_c \langle m_c \rangle^2] \quad (2-13)$$

where $m_{a,b,c}$ is the component of a unit vector in the prime axis and $\langle m_{a,b,c} \rangle = (1/v) \int m_{a,b,c} \, dv$. Now considering the constraint $m_a^2 + m_b^2 + m_c^2 = 1$ and using the Lagrangian multiplier method to find the minimum of E_{LB} . Moreover, Brown claimed that the state of lowest energy of a ferromagnetic body, whose size is less than a certain critical size, is one of uniform magnetization. Therefore, for any distribution of M whose magnetostatic energy is always larger than $E_{uniform}$, as well as

$E_{LB} \geq E_{uniform}$. From this inequality we can obtain the critical size which marks the boundary between uniform and non-uniform states.

$$L_{critical} = \frac{q}{M_s} \sqrt{\frac{C}{N_a}} \quad (2-14)$$

where q is the smallest solution of the Bessel functions and is related to the aspect ratio m of the prolate ellipsoid. $q = 1.8412 + 0.48694/m - 0.11381/m^2$. The red dashed line in Fig 2-3 is the critical length versus the aspect ratio for a permalloy ellipsoid by Eq. (2-14). The saturated magnetization $M_s = 830 \text{ emu/cm}^3$ and the exchange constant $C = 2.1 \times 10^{-6} \text{ erg/cm}$ were used. These two parameters are suitable for a confined structure and will be discussed in the section 3-3. The magnetization prefers to align uniformly for a wire with a high aspect ratio. While at a fixed aspect ratio, the uniform state would be observed in a shorter wire.

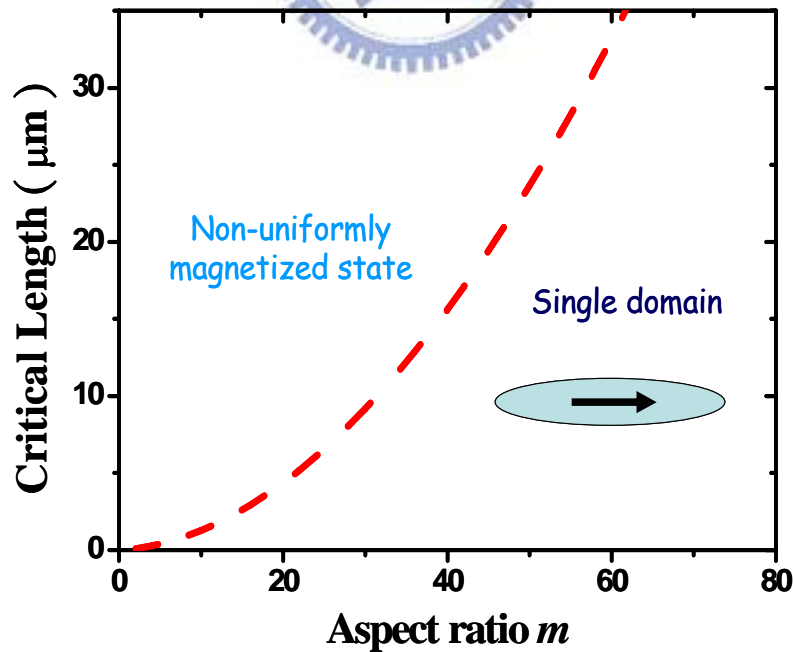


Fig 2-3: The theoretically domain diagram of a prolate ellipsoid as a function of the aspect ratio and the critical length.

Edge induced domain

For a rectangular thin film element, there are straight edges and sharp corners resulting in different domain configuration from an ellipsoid. The calculation of magnetostatic energy is complex and the numerical evaluation is usually used. The induced domain appears at the corner, due to the magnetic pole avoidance. Here, the edge induced domain in a wire is discussed based on a two-dimensional approximation which is suitable for a thin film of a soft magnetic material.

If the dimension of a rectangular thin film element with zero crystalline and induced anisotropy is much larger than the single domain limit, a flux closure magnetization configuration with vanishing magnetostatic energy may be favored. In such a pattern, the magnetization lies parallel to the film surface and is diverging free in the interior and at the edges. Therefore, domains and domain walls can be obtained under the consideration of the boundary conditions and the principle of pole avoidance. Van den Berg developed a comprehensive analysis on the prediction of the possible range of these domains and the position of domain walls for such thin film elements with arbitrary shape [9]. He proved that a stray field free magnetization pattern can be constructed when following the below conditions.

- Take circles that touch the edges at two (or more) points and lie otherwise completely within the figure. The centers of all such circles form the domain walls.
- If a circle touches the edges in more than two points, its centre forms a domain wall junction.
- In every circle the magnetization direction must be perpendicular to each touching radius.

For a rectangle, the domain pattern can be illustrated as a flux closure structure which is the well known Landau-Lifshitz pattern. In Fig. 2-4, the circles marked 1, 2, and 3 touch at least two points at the edge and lie completely within the rectangle.

Their centers $1'$, $2'$, and $3'$, respectively, are located at the domain walls. Moreover, circle 2 is touching the edge at three points implying that its center $2'$ coincides with a domain-wall junction. As for the circles 4 and 5, they are touching two edge points; however, they are lying only partly within the object, so that centers $4'$ and $5'$ are not at domain walls. Following the third condition, the magnetization direction must to be perpendicular to each touching radius resulting in the closure pattern.

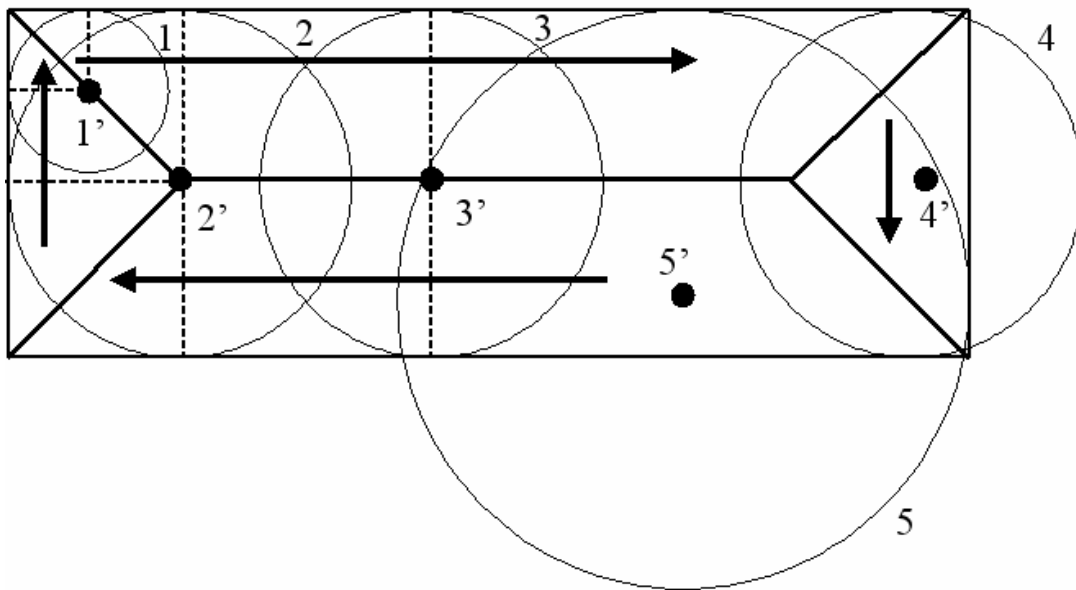


Fig 2-4: A formation of a flux closure pattern in a rectangle.

Subsequently, we try to find the energy gain by the flux closure domain relative to the single domain state, and below which sample size the flux closure domain become unstable, taking into account the domain wall energy. For a uniformly magnetized rectangular thin film element, the total energy is simply the E_{mag} . Although a thorough calculation of E_{mag} is necessary to be approached by the finite element calculation [10], we regard the rectangle as a prolate ellipsoid and use Eq. (2-11) to make calculations much easier. A flux closure domain may carry a zero net magnetization and hence, the total energy is the only domain wall energy and can be written as: $E_{FC} = [(2\sqrt{2} - 1)w + l] \cdot t \cdot \gamma$ where w , l , and t are the width, length, and

thickness of a rectangle, respectively. γ is the domain wall energy per unit area. The single domain limit $L_{critical}$ is obtained by equating the domain wall energy with Eq. (2-11), as following:

$$L_{critical} = \frac{l}{\left(\frac{1}{2} N_a M_s^2 l / \gamma \right) - (2\sqrt{2} - 1)} \quad (2-15)$$

The single domain limit is thus determined by the interplay between the domain wall energy and the magnetostatic energy.

2-2 Magnetization reversal in wires

Magnetization reversal is a process which refers to the variation of magnetic configuration under magnetic fields, pulse currents, and pulse fields, etc. The process in thin films and bulks has been widely investigated. Recent advantages in the nanofabrication methods have made the possibility of studying the magnetism at small length scale.

In our study, we focus on the reversal process of a wire. For a wide wire, these typical reversal mechanisms of a thin film, such as the nucleation and annihilation of domains and propagation of domain walls still play an important role in the reversal process. When a wire width is less than the critical length, the single domain is an energetically favorable state. The question of magnetization reversal mechanisms for such wire is whether the magnetic moment rotation is always in unison. Brown provided a set of differential equations from minimizing the additional energy contributed from the magnetization perturbation and claimed that the eigenfunctions of these equations are the state of system during reversal and the eigenvalues are the

switching fields (H_{sw}) at which field the magnetization has a significant change[11]. The physical system will choose the one yielding the least H_{sw} since the mode is more achievable. For a prolate ellipsoid, three eigenmodes are proposed such as the following: coherent rotation, magnetization curling, and magnetization buckling.

Their magnetization arrangements and the theoretical anticipation of the relationship between the H_{sw} and the wire width are presented in Fig. 2-5. In the coherent rotation mode, all magnetic moments remain parallel to each other during the reversal process. By contrast, the buckling mode and the curling mode have a zigzag configuration in the plane and a vortex structure in the cross-section, respectively. The switching field appears to be uncorrelated with dimensions for coherent rotation. The switching field decreases with increasing wire width as a reciprocal relation when the reversal is completed via the magnetization curling. A threshold between both is the exchange length $\ell_{ex}, 2\sqrt{C}/M_s$. For a semi-wire width larger than ℓ_{ex} , the reversal occurs through curling. While a semi-wire width is smaller than ℓ_{ex} , the coherent rotation is expected by the Stoner–Wohlfarth model [12]. Because the buckling mode occurs only in a narrow-sized interval, these two modes are usually seen as the only switching modes that can occur.

Later, several reports using the micro-magnetic simulation method show that the complete magnetization moment rotation during the reversal is not always uniform. The magnetization reversal can occur through a creation of domain wall pairs and then sweep across a wire [13-15]. Furthermore, a number of studies show that thermal fluctuation can activate magnetization reversal resulting in a non-uniformly spatial magnetization distribution [16,17].

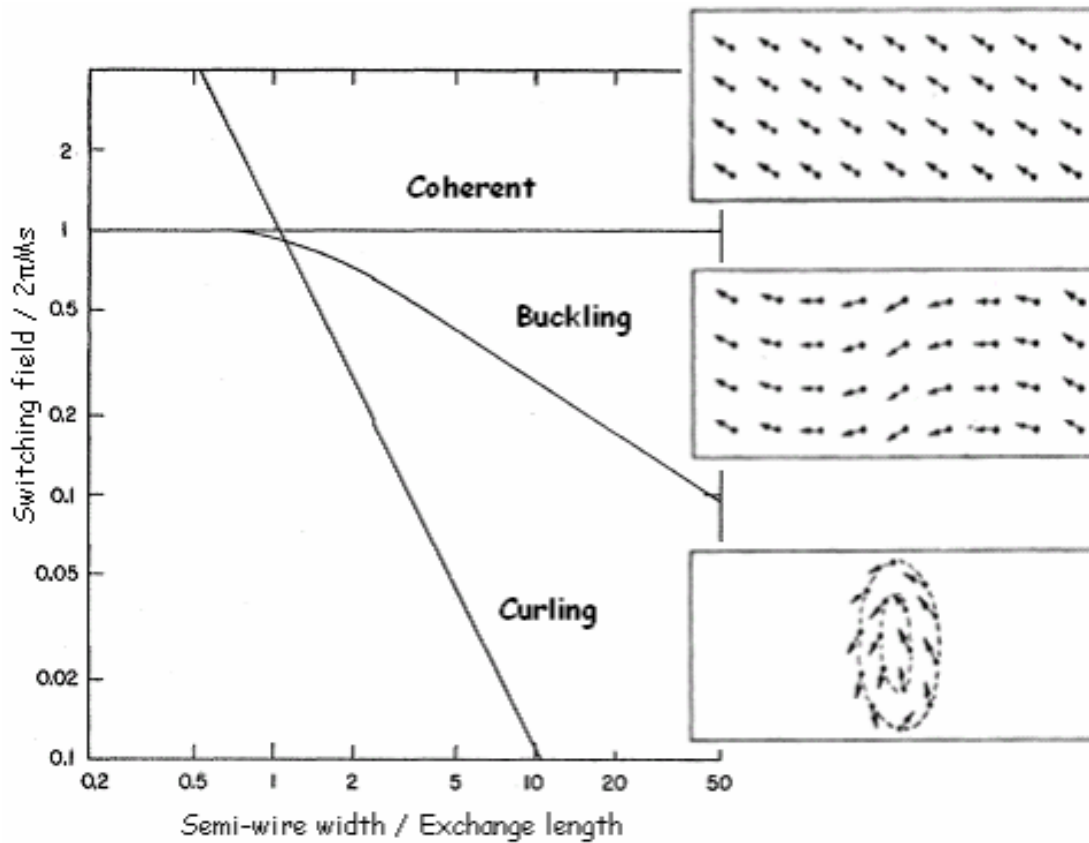


Fig 2-5: (Left) Theoretical plot of the reduced switching field as a function of the reduced semi-wire width for the coherent rotation, the magnetization curling, and the magnetization buckling. (Right) Illustration of magnetization reversal for the corresponding mechanism [18].

2-2-1 Magnetization reversal by Uniform rotation

Coherent rotation – Stoner Wohlfarth model

The magnetic moment rotates in the same angle everywhere and it is therefore known as the coherent rotation mode. It can be expressed in terms of the classic Stoner-Wohlfarth model [12]. In this model, a particle is assumed that exchange energy holds all spins tightly parallel to each other and there is a uniaxial anisotropy. Then, during the magnetization reversal the total energy consists of only E_{ani} and E_Z .

For a simply second-order uniaxial anisotropy, the total energy can be written as:

$$E_{total} = vK_u \sin^2 \phi - vM_s H \cos(\theta - \phi) \quad (2-16)$$

where ϕ and θ are the angles of magnetization and applied field with respect to the easy axis of magnetization, respectively. K_u is the uniaxial anisotropic constant. When the applied field is zero, the E_{total} exhibits a periodicity of π . There are minima and maxima at $\phi = n\pi$ with $n=0,1,2,\dots$ and $0.5,1.5,2.5,\dots$, respectively. The magnetization always lies along the easy axis at remanence. As illustrated in Fig. 2-6, the E_{total} is plotted as a function of θ , H , and ϕ according to Eq. (2-16). The magnetization reversal is determined by the local minimum and derivative of E_{total} . Here, we consider three different orientations of magnetic field relative to the easy axis. Let us start with the simple case that magnetic field is along the easy axis ($\theta=0^\circ$), as shown in Fig. 2-6(b). At remanence, magnetic moment is along the easy axis and E is a local minimum at $\phi = 0^\circ$. As the magnetic field is reversed, although E_{total} increases, the local minimum of E_{total} remains at $\phi = 0^\circ$ before reaching the H_{sw} . Until the magnetic field is equal to H_{sw} , $\phi = 0^\circ$ becomes a local maximum and magnetic moment rotate suddenly by 180° . For a new local minimum of E_{total} at $\phi = 180^\circ$ with further increasing magnetic field, the moment stays at $\phi = 180^\circ$. In another extreme case that magnetic field is perpendicular to the easy axis ($\theta=90^\circ$) as shown in Fig. 2-6(c). The magnetization is along the direction of the applied field when the applied field is large enough to saturate the magnetization, implying that $\phi = 90^\circ$ is the local minimum of the E_{total} . With reducing the applied field, $\phi = 90^\circ$ is no longer the local minimum, resulting in smooth rotation of magnetization until along the easy axis ($\phi = 0^\circ$ or 180°). There are two possible paths toward $\phi = 0^\circ$ or 180° , due to both paths are equivalent. The last case is that magnetic field is

neither along nor perpendicular to the easy axis. As shown in Fig. 2-6(a), the magnetic field makes an angle of 30° with respect to the easy axis. At remanence, magnetic moment is along the easy axis and E is a local minimum at $\phi = 0^\circ$. As the magnetic field is reversed, the local minimum of E moves slightly from $\phi = 0^\circ$ to $\phi = 30^\circ$ with increasing magnetic field resulting from the competition of the shape anisotropy and magnetic field. When the magnetic field is equal to H_{sw} , the magnetic moment switches to an angle $\phi = 150^\circ$, where has the lowest energy. Fig. 2-6(a) shows this switching behaviors indicated by the dashed line.

The switching field can be calculated by the analysis of the stability of the total energy. For given values of θ and H , the magnetization lies at an angle ϕ where the energy is a minimum locally. The magnetization direction must fulfill that the first derivative of E_{total} with respect to ϕ is zero. Using the reduced field $h = H/(2K_u/M_s)$ and the reduced magnetization $m = M/M_s = \cos(\theta - \phi)$, this equation can be written as:

$$2m(1-m^2)^{0.5} \cos 2\theta + (1-2m^2) \sin 2\theta = \pm 2h(1-m^2)^{0.5} \quad (2-17)$$

The magnetization hysteresis loop can be calculated from this equation by solving for m as a function of h . Then, H_{sw} as a function of θ can be obtained when $\partial h/\partial m = 0$ and $\partial^2 E_{total}/\partial \phi^2 > 0$, and can be written as:

$$H_{sw} = \frac{2K_u}{M_s} (\cos^{2/3} \theta + \sin^{2/3} \theta)^{-3/2} \quad (2-18)$$

A polar plot of reduced $H_{sw}(\theta)$ shown in Fig. 2-7 by the solid line is the famous Stoner-Wohlfarth astroid. There is four-fold symmetry of $H_{sw}(\theta)$. H_{sw} is a maximum when the applied field is parallel and perpendicular to the easy axis and is a minimum at $\theta=45^\circ \pm 90^\circ$, implying the magnitude of H_{sw} can be significantly reduced as

operating at this point. This concept has been used in the writing process of MRAM.

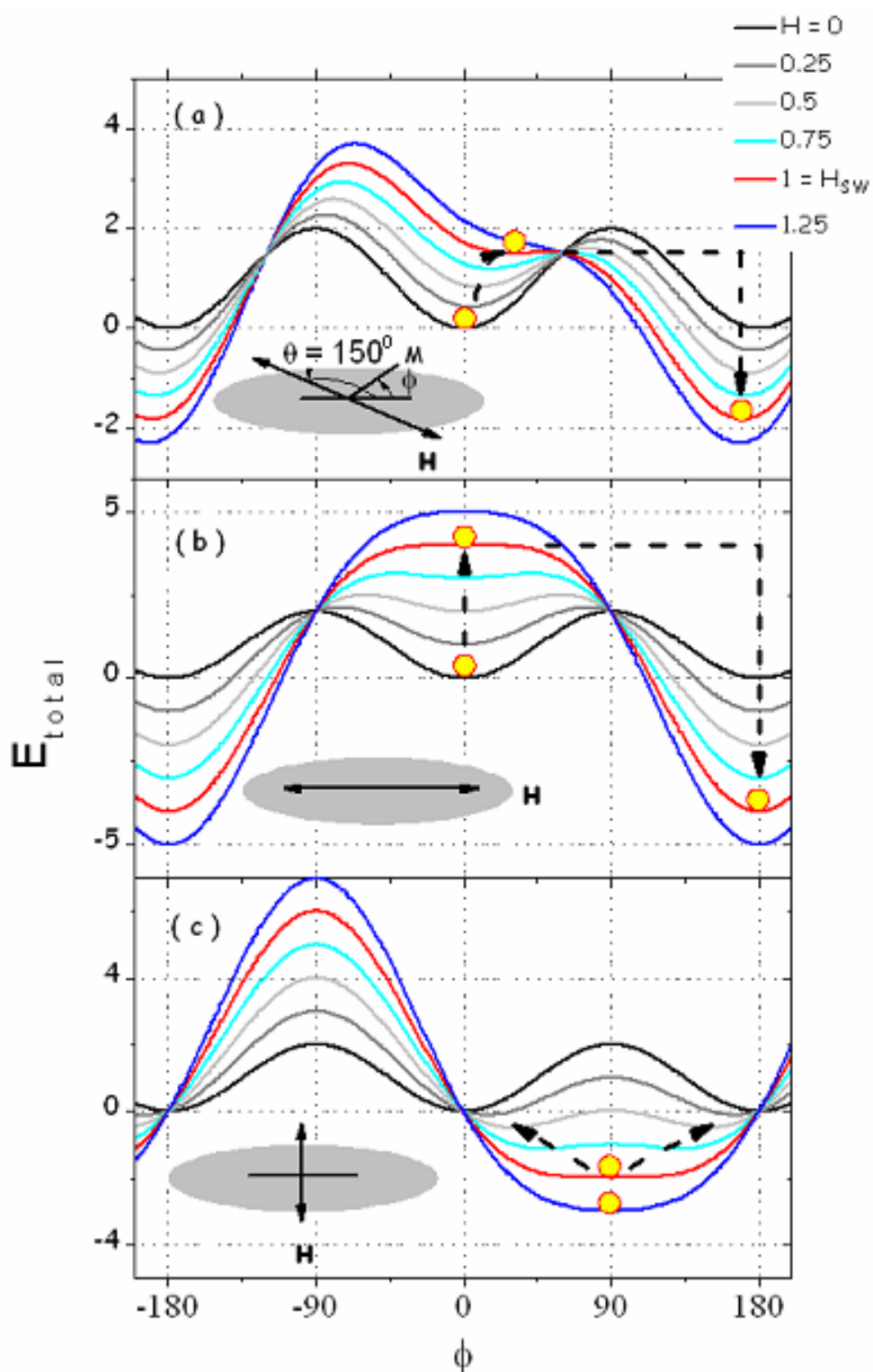


Fig 2-6: The total energy as a function of the magnetization angle for several magnetic field values based on Stoner-Wohlfarth model. (a) $\theta = 150^\circ$ (b) $\theta = 0^\circ$ (c) $\theta = 90^\circ$.

2-2-2 Nonuniform magnetization reversal

As seen in Fig. 2-5, magnetization should reverse by coherent rotation for small samples. For larger samples, nonuniform reversal modes are more likely. Two principal nonuniform reversal modes of an ellipsoid are curling mode and buckling mode. The latter was identified only in a narrow-sized interval. We ignore it here because of its minor importance. The former is discussed in the following.

Magnetization Curling

Curling mode assumes that the magnetization direction rotates in a plane perpendicular to the anisotropy axis of the wire, effectively reducing the stray field. The feature of this mode has been presented in Fig. 2-5. Although analytical solutions of the magnetization hysteresis loop by curling mode are not available. Aharoni assumed that magnetic moments rotate uniformly before switching and solved the Brown's differential equations based on the curling mode to obtain the angular dependence of the switching field for a prolate ellipsoid [19]. The relation is given by

$$H_{sw} = \frac{2\pi M_s (2D_a - \frac{k}{S^2})(2D_c - \frac{k}{S^2})}{\sqrt{(2D_a - \frac{k}{S^2})^2 \sin^2 \theta + (2D_c - \frac{k}{S^2})^2 \cos^2 \theta}} \quad (2-19)$$

where $D_a = N_a/4\pi$ and $D_c = N_c/4\pi$ are the demagnetizing factors of a prolate ellipsoid along the major and minor axes, respectively, which are presented in section 2-1-1. The parameter S is the reduced radius: $S = 2r/\ell_{ex}$, r is the minor semi-width. $k = q^2/\pi$ where q is the same geometrical factor used in Eq. (2-14). The switching field for several values of S as a function of θ is plotted as dashed lines in Fig 2-7. In the case of $S=2$, switching field of magnetization curling is a minimum when the applied

field is parallel to the easy axis and has an increasing trend when the magnetic field is applied approaching the hard axis. As we can see, the switching field of magnetization curling is less than coherent rotation when $\theta < 45^\circ \pm 90^\circ$, implying the reversal occurs via magnetization curling at small angle but via coherent rotation at large angle. The amount of the angle with the reversal completed via coherent rotation increases with decreasing S . For $S < 1$, the reversal is completely through the coherent rotation and the switching field is given by the Stoner-Wohlfarth model.

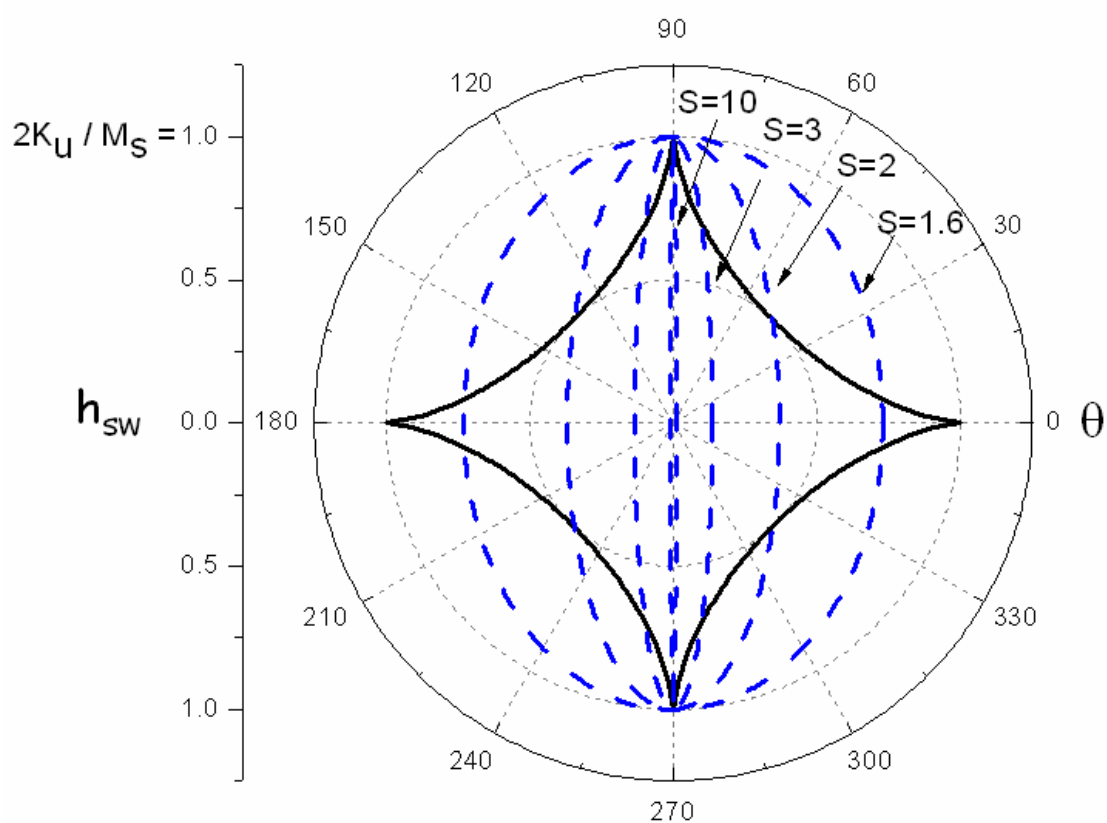


Fig 2-7: Angular dependence of the switching field of a prolate ellipsoid for several reduced radii S . For $S < 1$, the switching field is given by the Stoner-Wohlfarth model and is presented by the solid line.

Propagation of domain walls


In section 2-1-2, we mentioned that the edge domain of a thin film element exists based on the principle of pole avoidance. Even for a rectangle with a high aspect ratio of a near single domain state, the edge domain is still observed. The behavior of these domain structures in applied fields have been theoretically investigated by Bryant and Suhl [20]. Their initial ideal was that the magnetic charges induced in an applied field should be distributed as in the analogous electrostatic problem. The magnetic charges are expected at the edges of the element like the electric charges reside on the surfaces of a conductor. Once the distribution of these magnetic charges is known, the domain pattern can be calculated numerically for any field. As for a rectangle with a uniform magnetization for almost all volume except both ends, the propagation and the annihilation of domain walls play a major role during the magnetization reversal. The angular dependence of the switching field may be appropriately expected by $1/\cos\theta$, according to the projection of the magnetic field on the wire axis [21].

2-3 Magnetoresistance of ferromagnetic wires

The definition of magnetoresistance (MR) is the change in the resistance induced by an applied magnetic field. There are a number of different kinds of MR, such as Lorentz magnetoresistance (LMR), anisotropic magnetoresistance (AMR), giant magnetoresistance (GMR), colossal magnetoresistance (CMR), and domain wall magnetoresistance (DWMR), each with a different origin. Among them, AMR and DWMR have a major contribution for a single layer ferromagnetic specimen. Focusing on these two kinds of MR, their origin and behavior are discussed as follows.

2-3-1 Anisotropic magnetoresistance

The resistance of a material depends on its state of magnetization. This phenomenon is called magnetoresistive effect. The origin of the magnetoresistive effect in semiconductors and normal metals is the influence of the Lorentz force on the current path, with a result that the resistance is proportional to the square of the magnetic field. Apart from the ordinary magnetoresistive effect in semiconductors and normal metals, there is another effect in transition metals due to the spin-orbital interaction. In this effect the resistance depends on the orientation of the magnetization with respect to the direction of the electric current. The effect is often called the anisotropic magnetoresistance (AMR), which was first discovered by Kelvin [22].



It is convenient to explain AMR effect by taking into account the existence of the spin-orbital coupling and the anisotropic scattering mechanism of s and d electrons. In the case of the magnetic field direction with an angle relative to the current direction, the spin orbital interaction causes the resultant perturbed d-electron wave function to have a complex dependence on the angle. The transition probability of s electron to d orbital is large for electrons traveling parallel to the magnetic field. In the transition metal, the band structure is split into two different sub-bands of different orientations of the electron spins. When the 3d band is not fully filled, the transition of 4s electrons to 3d band is probable. The current of 4s electrons with smaller effective mass predominates the transport. The 3d electrons with large effective mass have low mobility. If there is a large transition probability of 4s electrons to 3d band, the increase of 3d electrons in the conduction current results in the decrease of conductance. Thus, when the current is parallel to the magnetic field direction, the

large transition probability leads to large resistance.

For a single crystalline metal with saturated magnetization, the Ohm's law is described by the following expression $\vec{E}_i = \rho_{ij}(\vec{M})\vec{J}_j$, where \vec{E} is the electric field, \vec{J} is the current density, and ρ is the tensor of the resistivity. Taking into account the crystal symmetry, Thomas obtained the resistivity tensor for a simple case that the magnetic field is in the film plane (x-y plane) [23]:

$$\begin{bmatrix} \rho_t \sin^2 \phi + \rho_l \cos^2 \phi & \frac{1}{2} \Delta \rho \sin 2\phi & \rho_H \sin \phi \\ \frac{1}{2} \Delta \rho \sin 2\phi & \rho_t \cos^2 \phi + \rho_l \sin^2 \phi & -\rho_H \cos \phi \\ -\rho_H \sin \phi & \rho_H \cos \phi & \rho_t \end{bmatrix} \quad (2-20)$$

where ρ_t and ρ_l are the resistivity at the current direction perpendicular and parallel to the magnetization direction, respectively. $\Delta \rho = \rho_l - \rho_t$. ρ_H is the Hall coefficient. ϕ is an angle between the orientation of the magnetization and the current direction. When the current is in the x-axis, the resistivity in the x-axis is described by the expression.

$$\rho_{xx}(\phi) = \rho_t + \Delta \rho \cos^2 \phi \quad (2-21)$$

It is the general formula of AMR effect. The resistivity in the y-axis is written as

$$\rho_{xy}(\theta) = \frac{1}{2} \Delta \rho \sin 2\phi \quad (2-22)$$

It is the so-called Planar Hall effect. The angular dependences of resistivity for both effects are presented in Fig.2-8. Both cases show an periodicity of π . AMR and PHE have maxima at $\phi = n\pi$ with $n=0,1,2\dots$ and $0.25,1.25,2.25\dots$, respectively, and minima with $n=0.5,1.5,2.5\dots$ and $0.75,1.75,2.75\dots$, respectively.

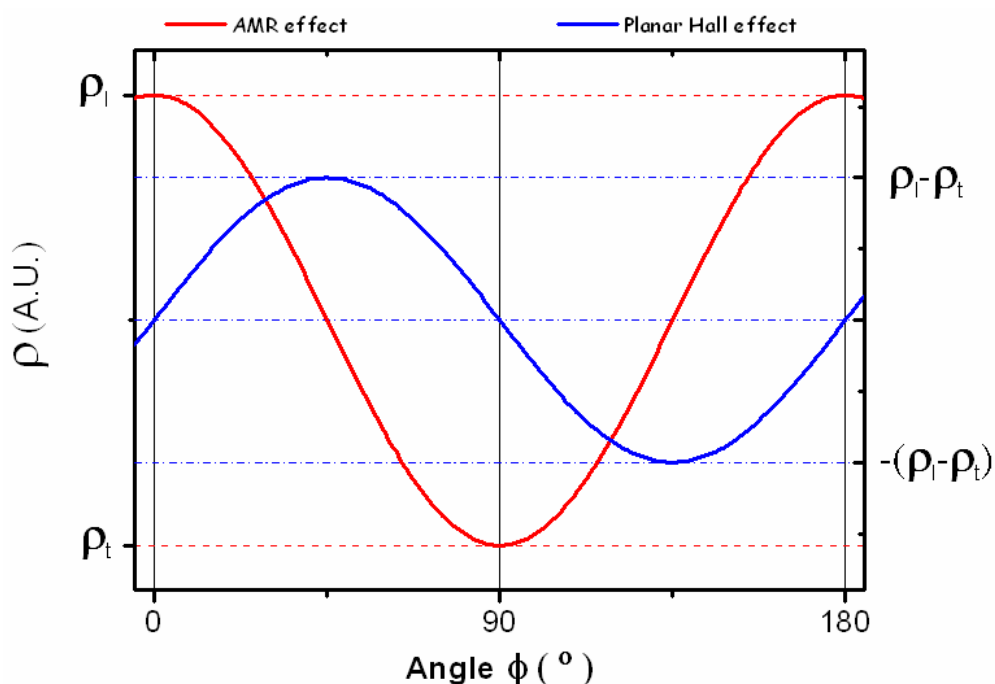


Fig 2-8: Schematic plot of the angular dependences of the resistivities, AMR (red) and PHE (blue), respectively.

2-3-2 Domain wall resistance

Domain wall resistance arises from the scattering when electric current passes through a domain wall. In general cases, the contribution of DW scattering to the MR is concealed by conventional sources of low temperature MR such as AMR and LMR in a ferromagnetic system. In order to isolate DWR, it is necessary to create artificial domain walls using a unique pattern such as adding a neck to the wires [24], designing zigzag structures [25], forming a striped domain by thickness modulation [26] or exchange biases [27], and implementing an elaborate magnetic field history process [28]. Although DWR was observed in various systems, both positive [24-28] and negative [29] values were reported with their theoretical justifications [30-32]. Up to now, the sign and the magnitude of the DWR and the fundamental mechanisms of DW scattering are still controversial. In this section, we introduce the historical

theories about the positive DWR.

Spin mistracking effect

The intrinsic DWR arising from the spin polarized current passing through a domain wall has been developed by two methods, semi-classical and fully quantum mechanical, to predict the magnitude of this effect. When electrons pass through a domain wall, the electron spin will precess around the rotating exchange field and lags behind in orientation with respect to the local magnetization, as seen in Fig. 2-9. Viret estimated the average of this angle via the exchange field rotating through in half of a Larmor precession. He treated the spin vector classically and found that the mean free path depends on the spin-dependent scattering rate and the cosine of the behind angle [33]. Then, DWMR can be written as:

$$\frac{\Delta R_{DW}}{R} = \frac{2P}{(1-P)^2} \left(\frac{h v_f}{D E_{ex}} \right)^2 \quad (2-23)$$

P is the spin-dependent scattering ratio, v_f is the Fermi velocity, D is the domain wall width, and h is Planck constant. For the example of Ni, the value of DWMR predicted by this semi-classical model is about 4×10^{-5} and follows the $\sim 1/D^2$ relation.

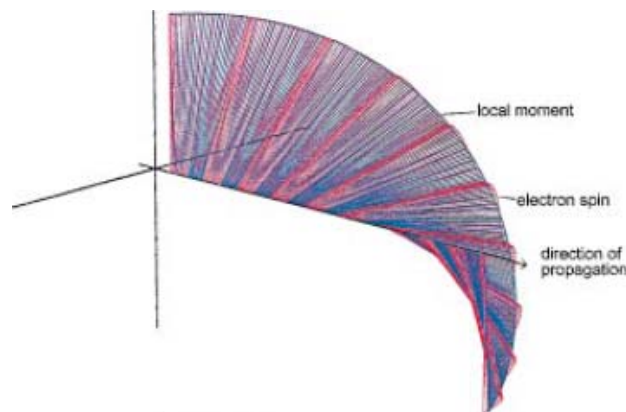


Fig 2-9: Numerical simulation of the spin trajectory for the electron spin transiting through domain walls in Ni. The electron spin orientation is showed in red and the local exchange field variation in blue [31].

Levy and Zhang rebuilt this model by replacing the simple rotating frame with a fully quantum mechanical analysis [30]. In their analysis, they used the same Hamiltonian that is used to describe the GMR in a magnetic multilayer. In addition to the potential and the kinetic energy terms, there is a spin dependent term involving the spin operator and the local magnetization distribution. When the magnetization is uniform, the Hamiltonian can be diagonalized along any chosen axis by making a rotation of the spin operator using the rotation operator. The resulted Hamiltonian can be recovered to the same form. However, when the magnetization is not uniform, like in the domain wall region, there is an extra term in the Hamiltonian as carrying on the diagonalisation. This extra term arises from a perturbation of the wavefunctions and becomes the source of an extra resistance. In a one-dimensional Bloch or Néel domain wall where the angle change of unit length $\theta(x) = x\pi/D$, implying that magnetic moment rotate linearly from one direction to the opposite direction through the wall width D , two useful formulas were found, corresponding to two basic measurement geometries, CIW and CPW where the current flow parallel and perpendicular to the wall, respectively. Eqs. (2-24) and (2-25) describe the DWMR in the conditions.

$$\left(\frac{\Delta R_{DW}}{R}\right)_{CIW} = \frac{\xi^2 (\rho_{\uparrow} - \rho_{\downarrow})^2}{5 \rho_{\uparrow} \rho_{\downarrow}} \quad (2-24)$$

$$\left(\frac{\Delta R_{DW}}{R}\right)_{CPW} = \frac{\xi^2 (\rho_{\uparrow} - \rho_{\downarrow})^2}{5 \rho_{\uparrow} \rho_{\downarrow}} \left[3 + \frac{10\sqrt{\rho_{\uparrow} \rho_{\downarrow}}}{\rho_{\uparrow} + \rho_{\downarrow}}\right] \quad (2-25)$$

$\rho_{\uparrow\downarrow}$ is the resistivity for spin \uparrow and \downarrow of the ferromagnet. $1/\rho = 1/\rho_{\uparrow} + 1/\rho_{\downarrow}$ is the conductivity of the ferromagnet without domain walls. The mistracking parameter $\xi = \pi\hbar^2 k_F / 4mDJ$, J is the exchange splitting energy. If one wants to obtain a large DWR, it is necessary to make ξ as large as possible, one way that this can be achieved is to have a narrow wall. For the example of Co, the value of DWMR

predicted by this model is 0.3-1.8% for a CIW case and 2-11% for a CPW case, and DWR also follows the $\sim 1/D^2$ relation.



References:

1. A. Aharoni, *Introduction to the Theory of Ferromagnetism*, Oxford University Press, Oxford, 2000.
2. B. D. Cullity, *Introduction to magnetic materials*, Addison-Wesley publishing company, 1972.
3. P. Bruno, Phys. Rev. B **52**, 411 (1995).
4. J. Slonczewski, J. Magn. Magn. Mat. **150**, 13 (1995).
5. L. Néel, C. R. Acad. Sci. Paris **237**, 1468 (1953).
6. D. S. Chuang, C. A. Ballantine, and R. C. O'Handley, Phys. Rev. B **49**, 15084 (1994).
7. J. A. Osborn, Phys. Rev. **67**, 351 (1945).
8. A. Aharoni, J. Appl. Phys. **63**, 5879 (1988).
9. H. A. M. van den Berg, IBM J. Res. Dev. **33**, 540 (1989).
10. P. Rhodes and G. Rowlands, Proc. Leeds Phil. Soc. **6**, 191 (1954).
11. W. F. Brown, Phys. Rev. **105**, 1479 (1957).
12. E. C. Stoner and E. P. Wohlfarth, Philos. Trans. R. Soc. London, Ser. A **240**, 599 (1948) [reprinted in IEEE Trans. Magn. **27**, 3475 (1991)].
13. R. Ferre', K. Ounadjela, J. M. George, L. Piraux, and S. Dubois, Phys. Rev. B **56**, 14066 (1997).
14. J. McCord, A. Hubert, G. Schröpfer, and U. Loreit, IEEE Trans. Magn. **32**, 4806 (1996).
15. M. Brands, R. Wieser, C. Hassel, D. Hinzke, and G. Dumpich, Phys. Rev. B **74**, 174411 (2006).
16. J. S. Broz, H. B. Braun, O. Brodbeck, and W. Baltensperger, Phys. Rev. Lett. **65**, 787 (1990).

17. H. B. Braun, Phys. Rev. B **50**, 16501 (1994).
18. E. H. Frei, S. Shtrikman, and D. Treves, Phys. Rev. **106**, 446 (1957).
19. A. Aharoni, J. Appl. Phys. **82**, 1281 (1997).
20. P. Bryant and H. Suhl, Appl. Phys. Lett. **54**, 2224 (1989).
21. F. Cebollada, M. F. Rossignol, D. Givord, V. V. Boas, and J. M. González, Phys. Rev. B **52**, 13511 (1995).
22. W. Thomson, Proc. R. Soc. **8**, 546 (1857).
23. G. Thomas, Physica **45**, 407 (1969).
24. S. Lepadatu and Y. B. Xu, Phys. Rev. Lett. **92**, 127201 (2004).
25. T. Taniyama, I. Nalatani, T. Namikawa, and Y. Yamazaki, Phys. Rev. Lett. **82**, 2780 (1999).
26. W. L. Lee, F. Q. Zhu, and C. L. Chien, Appl. Phys. Lett. **88**, 122503 (2006).
27. D. Buntinx, S. Brems, A. Volodin, K. Temst, and C. V. Haesendonck, Phys. Rev. Lett. **94**, 017204 (2005).
28. U. Ebels, A. Radulescu, Y. Henry, L. Piraux, and K. Ounadjela, Phys. Rev. Lett. **84**, 983 (2000).
29. U. Rüdiger, J. Yu, S. Zhang, A. D. Kent, and S. S. P. Parkin, Phys. Rev. Lett. **80**, 5639 (1998).
30. P. M. Levy and S. Zhang, Phys. Rev. Lett. **79**, 5110 (1997).
31. J. F. Gregg, W. Allen, K. Ounadjela, M. Viret, M. Hehn, S. M. Thompson, and J. M. D. Coey, Phys. Rev. Lett. **77**, 1580 (1996).
32. G. Tatara and H. Fukuyama, Phys. Rev. Lett. **78**, 3773 (1997).
33. M. Viret, D. Vignoles, D. Cole, J. M. D. Coey, W. Allen, D. S. Daniel, and J.F.Gregg, Phys. Rev. B **53**, 8464 (1996).

3 Experimental Details

In the investigation of domain structure and magnetization reversal on micron and sub-micron magnetic structures, we take several experimental techniques. This chapter is divided into two parts. First part is techniques of device fabrication. Second part is the measurement techniques involving magnetoresistance measurement and magnetic domain observation.

3-1 Device fabrication

The micron and sub-micron magnetic samples in the experiment are fabricated using two kinds of lithography techniques. One is Photo-Lithography (PL) which is the standard method of producing devices in the semiconductor industry. The other is electron beam lithography (EBL) which is a flexible technique for creating extremely fine patterns and is used principally in the support of mask making in the integrated circuit industry. Both lithography methods have similar fabrication procedures apart from the exposure source. An electron beam is used in EBL to expose the resist, whereas, in contrast, ultraviolet (UV) light is used in PL. Deposition of materials into the groove of the resist constructed by either EBL or PL is then carried out. Figure 3-1 shows a nanowire device at several levels of magnification so that the photo and e-beam lithography steps are all visible. Au(70nm) and Ti(10nm), which has good adhesion with (100) Si substrates, are stacked sequentially to form the electrode pads as seen in the top left figure. The entire deposition process is employed using thermal evaporation at a base pressure of 2.3×10^{-6} Torr. The dimension of one end of the electrode is about $200\mu\text{m}$ for wire bonding. As extending the other end of the electrode to the center of the device, the dimension is decreased to $5\mu\text{m}$. As for the

analytic pattern in the submicron scale, the EBL is appropriately chosen. The material used in this study is ferromagnetic Permalloy ($\text{Ni}_{80}\text{Fe}_{20}$). Later a brief introduction will be given to the lithography techniques described above together with the recipe used and the results.

The outline of the fabrication process is as follows:

1. Cleave a small chip ($\sim 6\text{mm} \times 6\text{mm}$) from the Si wafer.
2. Pattern, deposit, and anneal the bond pads (photolithography).
3. Pattern and deposit the analytic pattern on μm and sub- μm scales (e-beam lithography).
4. Pattern and deposit the contact pattern which connects the bond pads and the analytic pattern (e-beam lithography).
5. Glue chip to carrier and wire bond the device.

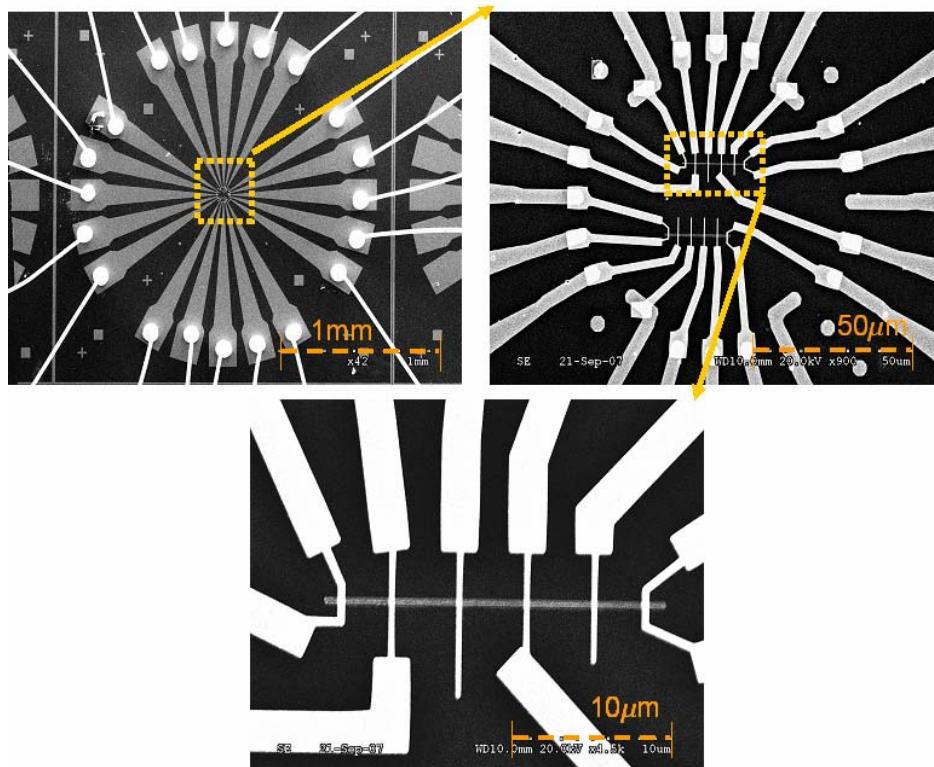


Fig 3-1: SEM images of a typical device at different magnifications. The upper left image shows the bond pad structure with wire bonds. The other two images show the contact and the analytic pattern.

3-1-1 Photolithography

Photolithography is the process of using UV light to transfer geometric shapes on a mask to a light-sensitive chemical on the surface of a substrate. The ideal resolution of this technique is limited by the wavelength of the light that is used. In our experiment, ABM Model 60 DUV/MUV/NearUV Mask Alignment and Exposure System is used. A 500W high pressure mercury arc lamp provides an intensity of around 60mW/cm^2 for h-line (400nm) and around 35mW/cm^2 for i-line (365nm). The i-line is filtered from the spectrum of mercury with the intensity around $20\sim 25\text{mW/cm}^2$ for our process in which the exposure time is $\sim 10\text{sec}$. Attachment between the sample and mask is in contact mode. Using this mode, certain faults of generating patterns during the imprint process, such as the wavy edge and the reduction of the pattern dimension caused by the deficient light dose, can be corrected. The photo-resist AZ5214 is used here. The polarity of this kind of resist can be reversed by a sufficiently exposure energy resulting in the formation of good undercut profiles for the advantage of lift-off step. The extreme resolution of the i-line source limited by the interference is about $\sim 50\text{nm}$. However, the actual conditions, such as the numerical aperture, the sensitivity of the chemical resist, and the method of applying the lift-off technique, cause the best resolution in this procedure to be around $0.6\mu\text{m}$. Fig. 3-2 presents the two SEM images of photo-lithography patterns. The dimension of the outer pads is about $200\mu\text{m}$ and the dimension of the inner leads is about $5\mu\text{m}$. The basic photolithography process recipe I have used is showed in the following.

The photolithography recipe

- ◆ Clean in acetone, alcohol, D.I. water and dry using nitrogen gas.
- ◆ Spin AZ5214 photo-resist, first at 1000rpm for 10sec and then at 5000rpm for 40sec. (This gives a $\sim 1\mu\text{m}$ thick layer.)
- ◆ Soft bake at 90°C for 90sec.
- ◆ Expose at an energy density of $28\text{mW}/\text{cm}^2$ for 1 sec (i-line). (The time required depends on the energy density of the i-line and the thickness of the resist.)
- ◆ Reverse bake at 120°C for 90sec. (A special property of AZ5214 is that the polarity can be reversed from positive to negative.)
- ◆ Perform a flood exposure for 20sec.
- ◆ Develop in AZ400 for ~ 20 sec. Rinse in D.I. water for ~ 5 sec, and then blow dry.
- ◆ Clean any residual resist using O_2 plasma at 800V for 2min.
- ◆ Evaporate the materials and remove the resist by soaking in acetone and agitating using a mild ultrasonic.
- ◆ Finish by rinsing in D.I. water for ~ 3 sec and then blowing dry.

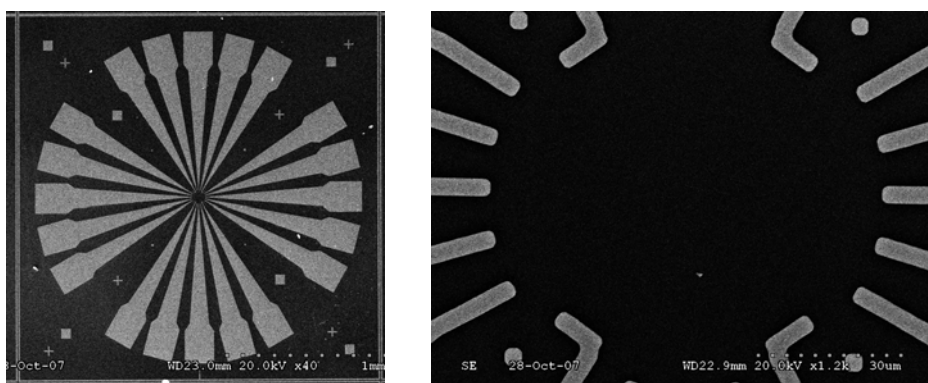


Figure 3-2: SEM images of the typical photolithography pattern at different magnifications, 40(left) and 1200(right).

3-1-2 Electron beam lithography

This technique consists of focusing an electron beam by electron lenses and scanning it across a substrate covered with a resist which is sensitive to the electron dose. The desired patterns are then created on the resist film. The focusing and scanning process is similar to the operation of a CRT display. Compared with the photolithography method, it is capable of very high resolution since the wavelength of an electron ($\sim 0.008\text{nm}$ at 25kV) is smaller than the UV light. It is also highly flexible since no mask is needed, but it is slower than the photo-lithography method. In our experiment, a Hitachi S3000H was used as the SEM system and the pattern generator is Nanometer Pattern Generation System (NPGS). In the SEM system, the electron beam is thermionically emitted from the tungsten hairpin and the beam size, which depends on the accelerating voltage and the lens aberrations, is focused using two sets of condensing lenses together with many apertures to be around $\sim 5\text{nm}$ at 30kV . The magnitude of the emission current is around $100\mu\text{A}$ at initial release. After the electron beam is focused through several apertures and lenses, the magnitude of a beam current is weakened to be about 10pA at the sample surface. A positive resist with a molecular weight of 495K Polymethyl methacrylate (PMMA) is used. It makes an intrinsic roughness $\sim 5\text{-}10\text{nm}$ [1]. Fig. 3-3 shows two kinds of e-beam lithography patterns of disks and wires. The diameter of disks ranges from 1.2 to $0.11\mu\text{m}$ as shown in the left figure. For the planar wire in the right figure, the length is $20\mu\text{m}$ and widths span from 1 to $0.3\mu\text{m}$. The following is our recipe.

The E-beam lithography recipe

1. Clean in acetone, alcohol, D.I. water and dry using nitrogen gas.
2. Spin a 5% solution of 495K PMMA at 6000rpm for 55sec. This gives ~300nm thick layer.
3. Hotplate bake at 180°C for 5min*.
4. Expose the designed pattern using e-beam system (dosage is about 200~300 $\mu\text{C}/\text{cm}^2$ at 20kV).
5. Develop in MIBK: IPA, 1:3 for 75sec. Rinse in IPA at 25~26°C for 25sec, and then in D.I. water for 5sec. Blow dry.
6. Clean any residual resist using Ar plasma at 800V for 2min.
7. Evaporate the materials and remove the resist by soaking in acetone and agitating using a mild ultrasonic.
8. Finish by rinsing in D.I. water for ~ 3sec and then blowing dry.

* In order to create a good undercut profile, a bilayer resist should be used. Before step 2, the P(MMA-MAA) resist which has a lower molecular weight than PMMA is spun as the bottom layer at 3000rpm for 30sec. The wafer was baked at 180°C for 5min and then spun for 1min to cool down.

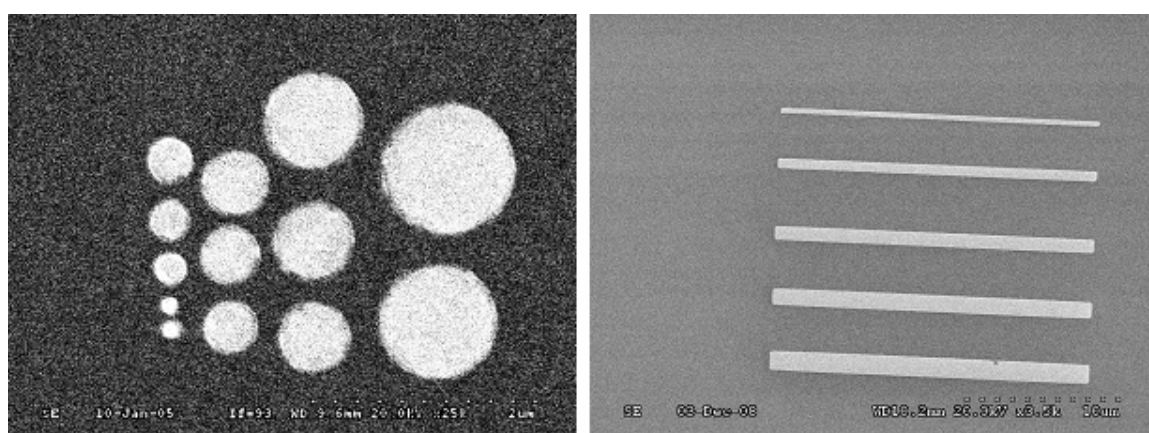


Figure 3-3: Two kinds of electron beam lithography patterns. (Left) Disks have diameters range from 1.2 to 0.11 μm . (Right) Wires with a fixed length of 20 μm have various widths from 1 to 0.3 μm .

3-2 Measurement techniques

3-2-1 Magnetoresistance measurement

The magnetoresistance measurement is performed in a variable temperature ^4He cryostat. Temperature in the range of 1.3 to 300K could be stabilized by the equilibrium of cooling power generated from liquid helium evaporation and heating power produced by a resistive heater. Temperature of samples can be detected by a calibrated GaAlAs diode and be read out using the Neocera temperature controller LTC11. The accuracy of the temperature obtained from the diode could be better than 0.1%. The diode is attached with samples through oxygen-free copper which is a good thermal conductor, resulting in almost zero temperature gradient between samples and diode. The cryostat is set up such that the sample is in the center of an electromagnet. Due to 2'inch gap opening for the cryostat tail, the electromagnet can produce a magnetic field up to 2.3kOe which is limited by a voltage output utilizing a power supply Kepco 36-28 and the saturated magnetization of the electromagnet core. The stability of output current of this power supply in constant current mode may be better than 1mA corresponding to a magnetic field of 0.1Oe. The electromagnet provides a uniform magnetic field environment for a volume of $1 \times 1.2 \times 1.2 \text{ cm}^3$ in the center of the gap, which is much larger than our sample dimensions. The magnitude of the magnetic field is determined by a calibrated InAs hall sensor attached on the gap wall. The read-out uncertainty of this sensor is smaller than 1% for field up to 5kOe. Therefore, a stable, accurate, and uniform magnetic field is well set up for our measurements.

The resistance measurement is carried out using "Linear Research 750 four-wire

AC Resistance Bridge”, which uses a four-wire(lead) ac lock-balance technique. A fixed amplitude 15.9Hz current provided by the ac voltage in series with a high resistive resistor is sent to two current leads of the sample. The voltage across the sample via two voltage leads is drawn back to the bridge to be balanced against an equal and opposite ac voltage. This gives a continuous null signal at the front end amplifier of the bridge’s lock balance circuitry. Knowing the value of the equal and opposite ac voltage gives the value of the sample’s resistance. The four-wire measurement technique eliminates errors that might be caused by leads or sample contact resistance. The ac measurement method eliminates DC thermoelectric voltage errors. Therefore, the voltage resolution can be down to the sub-nanovolt region and the resistance sensitivity is better than 10^{-5} . The analog voltage is then digitized by a digital multimeter Keithley 2000. The data is continuously taken by a computer through the interface IEEE-488.

The purpose of our magnetoresistance measurement is to investigate the static reversal behavior. Each data point was measured at a static state, in a given magnetic field at a constant temperature. When a target magnetic field is reached, we wait for couple seconds to dispel the eddy current and then sample resistances is taken by averaging over six read out values of LR750. During the resistance measurement, temperature and magnetic field are continuously monitored to insure the stability.

3-2-2 Magnetic domain observation

Magnetic domains are normally so small that one must use a microscope to see them. Many methods have been developed to observe them, such as the early **Bitter method**, which is performed by sprinkling extremely fine particles of magnetite on the surface of the specimen and observing the patterns formed by magnetite on the dispersion of the magnetic flux. Another approach is the **Lorentz microscope**, which is conducted by passing an electron beam through the specimen. Owing to the electrons experience the Lorentz force, its trajectory will be deflected by an amount that depends on the magnitude and the direction of the local M_s vector, thereby recognized the location of the domain. A third technique is the **Magneto-optic microscope**, which is carried out by measuring the rotation of polarization of a light during reflection or transmission from a specimen. The amount of the rotation also depends on the direction and the magnitude of the magnetization. **Magnetic force microscope** (MFM) is another tool for the investigation of magnetic domain structure. It was introduced shortly after the invention of atomic force microscope and has then widely used since the early 1990s. We compare these methods and summarize in Table1. Lorentz microscope and MFM have a better spatial resolution but a longer recording time and hence, are general to be used in the static behavior study. Magneto-optic microscope has an extremely short recording time. Therefore, it is used to investigate the dynamic behavior.

	Spatial resolution (nm)	Recording time (sec)	Sample preparation quality requirements
Bitter method	> 50	> 0.5	Low
Lorentz microscope	> 5	> 1	Very high
Magneto-optic microscope	> 100	> 10 ⁻³ > 10 ⁻⁹ (laser)	High
Magnetic force microscope	> 10	> 60	Low

Table 1. Qualitative comparison between different domain observation methods.

In our study, MFM is used. In such scanning probe method the interaction between tip and sample is the most important factor. When the distance between tip and the surface of sample is less than a few angstroms, the repulsive Van der Waals' force (F_v) propels the tip away from the sample. In contrast, an attractive F_v exists when the distance ranges from tens to hundreds of angstroms. When magnetic tips were used to probe the magnetic materials, the long-range magnetic force (F_m) must be included. Fig. 3-4 shows these forces F_v and F_m as function of the tip sample separation distance. As we operate in the far field region, where a resonant magnetic tip is lifted at a height of ~ 50 nm, the gradient of the magnetic force (F_m') is greater than the gradient of the Van der Waals' force (F_v'), leading the magnetic force to dominate the interaction.

Each cantilever has its own characteristic resonant frequency, which depends on its dimensions and the materials. The resonant frequency is the square root of the spring constant k divided by its mass m , $\omega = \sqrt{k_{eff}/m}$. Here, the effective spring constant can be written as $k_{eff} = k - (F_m' + F_v')$. The effective spring constant changes when the force between the tip and the sample has a spatial gradient. The inset in Fig. 3-4 shows that when the resonant frequency shifts, there is a change in the amplitude

at a given frequency. This change in amplitude reflects the change in the force gradient acting on the cantilever. Both frequency and amplitude of the cantilever vibration are monitored as changes in the position of the laser spot incident on the position sensitive photodetector (PSPD). The AC signal from the PSPD is sent to a lock-in amplifier and a DC signal is output proportional to the vibration amplitude. Then the DC signal is compared with the reference amplitude settings to calculate the change in amplitude. In order to maintain the constant vibration amplitude, the change in the amplitude feeds back to the Z controller to raise or lower the Z position of the piezoelectric scanner. The voltage applied to the scanner to maintain constant force gradient is used to generate domain images.

In our experiment, MFM images were taken by Digital Instruments Nanoscope IIIa in the nanostructure laboratory of Dr. J. C. Wu or by Digital Instruments Veeco CP-II in the advance storage thin film laboratory of Dr. C. H. Lai. Using both equipments, the topography and magnetic contrast can be easily separated in tapping/lift mode as a tip is lifted at a height of 70~100nm. Two types of commercial magnetic tips produced by Nanosensors were used. One is a standard hard magnetic tip, PPP-MFMR, which is Si cantilever tip coated with CoCr and has an effective magnetic moment about 10^{-13} emu on the tip. The other is a low moment tip, PPP-LM-MFMR, which has the same feature of the cantilever as the standard tip but has a half thickness of coated Co alloy and a less tip radius (<30nm). There is a weak interaction between this tip and sample and the perturbation and the distortion of domain structures caused by the tip induced stray field can be reduced. Both types of tips have a similar resonant frequency ~ 80 kHz.

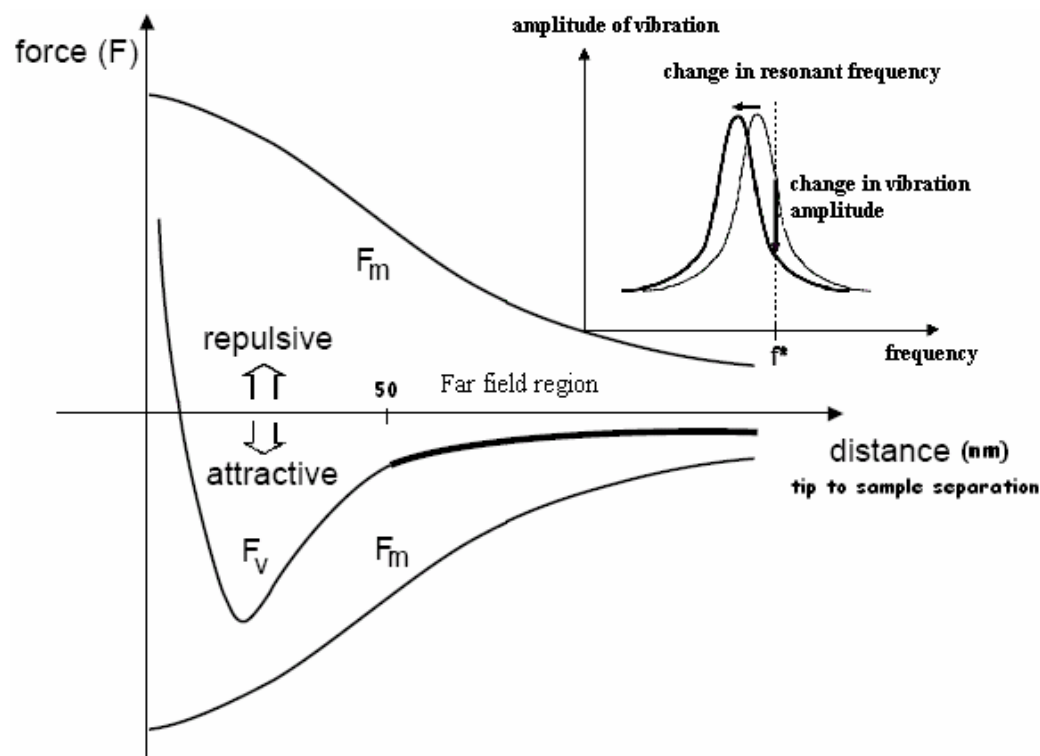


Figure 3-4: Van der Waals' force F_v and magnetic force F_m versus the distance between tip and sample. The inset is a response curve when a resonant cantilever forced an external force.

3-3 Characteristics of permalloy ($\text{Ni}_{80}\text{Fe}_{20}$) samples

Permalloy is a trade name that refers to the iron-nickel alloys containing about 50 to 80 percent of Ni. Its intrinsic properties, such as the Curie temperature (T_c), the saturation magnetization (M_s), the magnetocrystalline constant (K_1), and the magnetostriction constant (λ), depend on the percentage of nickel. In our system, in order to highlight the shape anisotropy, we deliberately select $\text{Ni}_{80}\text{Fe}_{20}$ because it has almost zero magnetostriction and a small magnetocrystalline constant. Some major properties of single crystalline $\text{Ni}_{80}\text{Fe}_{20}$ bulk are listed below [2,3]:

Permalloy (Ni₈₀Fe₂₀)

- ◆ F.C.C.
- ◆ $T_c = 853K$
- ◆ $M_s = 820\text{emu/cm}^3*$
- ◆ Magnetocrystalline $K_I = 2 \times 10^3 \text{erg/cm}^3$
- ◆ Magnetostriction ~ 0
- ◆ Exchange constant $C = 2.1 \times 10^{-6} \text{erg/cm}^{**}$
- ◆ Permeability $\mu \sim 100k$
- ◆ Exchange integral $J_{ex} = 3K_B T_c / 2ZS(S+1) \sim 0.3KT_c \approx 22\text{meV}$
- ◆ Block wall width $\delta = \pi \sqrt{C/2K} \approx 20\text{nm}$
- ◆ Exchange length $l_{ex} = \sqrt{C/4\pi M_s^2} \approx 5\text{nm}$

* We have performed magnetization hysteresis measurement for our permalloy wires to confirm that the saturated magnetization in our samples is close to the bulk.

** The value is for a thin film [3].

In subsequence, we give a brief introduction of some properties for our permalloy wires.



3-3-1 Magnetization hysteresis loop

Two MH loops in Fig. 3-5 were measured by superconducting quantum interference device (SQUID) for a 30nm thick permalloy thin film deposited on a $5.3 \times 3\text{mm}^2$ Si wafer and an array consist of ~ 3600 permalloy wires with $60(L) \times 1.3(W) \times 0.03(T) \mu\text{m}^3$. Coercive fields are ~ 3 and 150Oe for the thin film and the wire array, respectively. Volumetric saturated magnetization density calculated from the loop is $\sim 830\text{emu/cm}^3$ for both samples. The value is very close to that of a bulk.

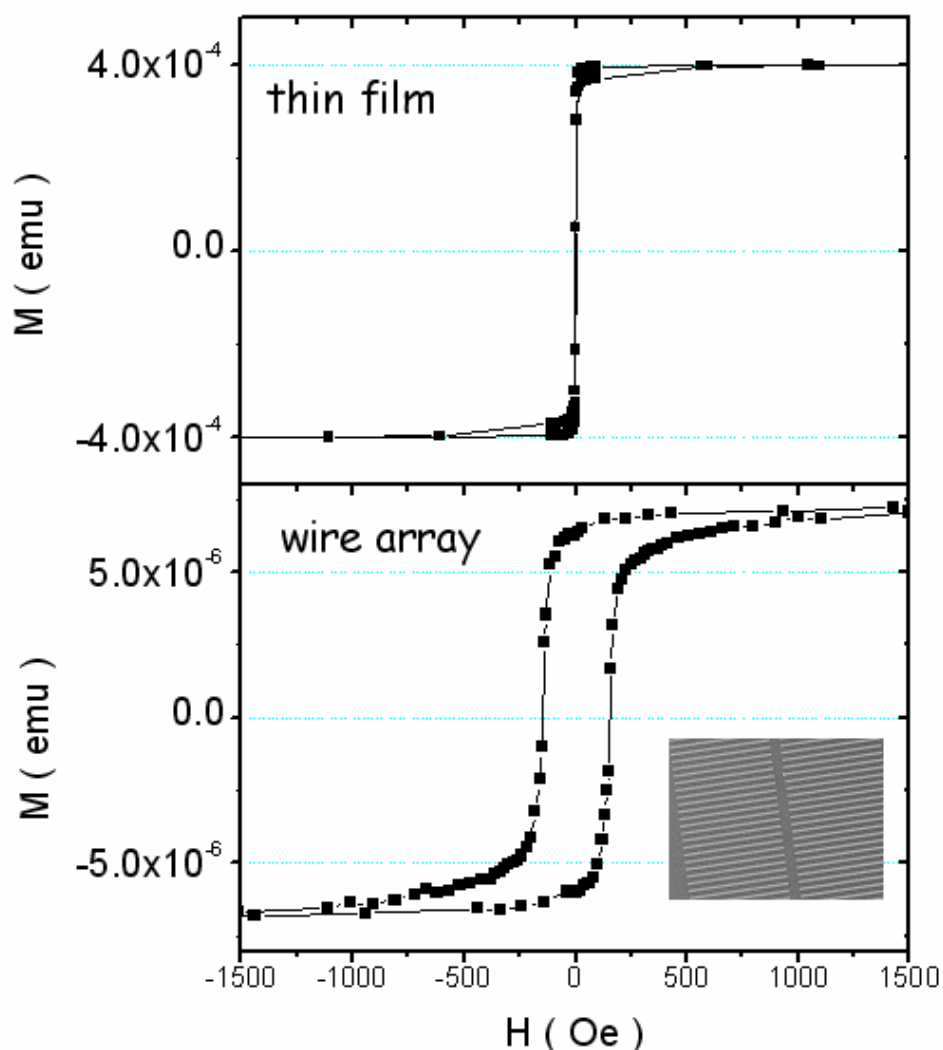


Figure 3-5: Magnetization hysteresis loops for a permalloy thin film (top) and a wire array sample (bottom). Both loops were measured using SQUID at 10K.

3-3-2 Resistivity of permalloy wires

Resistivity in a series of permalloy wires with $20\mu\text{m}$ long, 30nm thick, and various widths from 0.12 to $10\mu\text{m}$ have been measured. Fig. 3-6 illustrates the resistivity as a function of the wire width. When a wire width is larger than $10\mu\text{m}$, the value of resistivity would be close to that of a thin film. While resistivity decreases with increasing wire width for narrow wires. We calculate the mean free path of the thin film sample according to the free-electron model. $\rho = 23.7\mu\Omega\text{cm}$, the carrier

density $n = 1.25 \times 10^{28} m^{-3}$ estimated by one electron per atom, and the Fermi velocity $v_F = 0.22 \times 10^6 m/s$ are used [4], leading to the mean free path $\sim 2.6nm$ which is reasonable for Py [5]. In another series of Py disk samples, we found that the average grain size of Py decreases from 35nm to 20nm when the disk diameter reduces from 5 to $1\mu m$. Comparing to the mean free path, conduction electrons would suffer an increase of scattering events when the grain size reduces with decreasing the dimension of samples. Therefore, we suggest that the relationship of resistivity with wire widths may be due to the boundary scattering or grain boundary scattering [6-9].

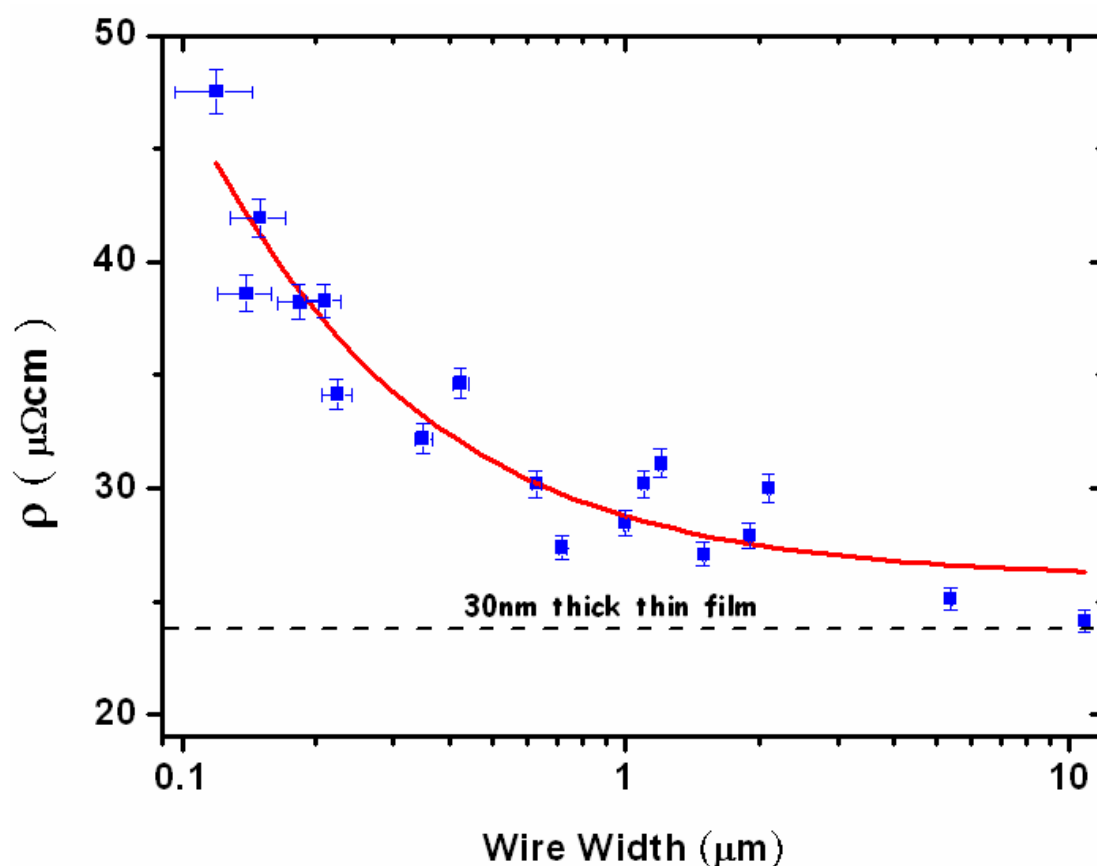


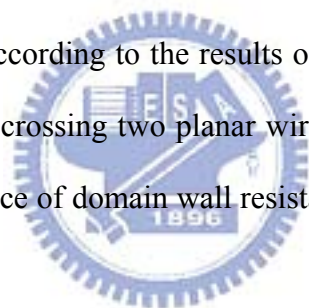
Figure 3-6: Resistivity of 30nm thick permalloy wires as a function of wire width. The square symbol is data measured at 10K. The solid line is a guide to the eye and the dashed line shows the resistivity of a thin film.

References:

1. S. Yasin, D. G. Hasko, M. N. Khalid, D. J. Weaver, and H. Ahmed, *J. Vac. Sci. Technol. B* **22**, 574 (2004).
2. B. D. Cullity, *Introduction to magnetic materials*, Addison-Wesley publishing company, 1972.
3. N. Smith, D. Markharn, and D. LaTourette, *J. Appl. Phys.* **65**, 4362 (1989).
4. D. Y. Petrovykh, K. N. Altmann, H. Hochst, M. Laubscher, S. Maat, G. J. Mankey, and F. J. Himpsel, *Appl. Phys. Lett.* **73**, 3459(1998).
5. S. Dubois, L. Piraux, J. M. George, K. Ounadjela, J. L. Duvail, and A. Fert, *Phys. Rev. B* **60**, 477(1999).
6. K. Fuchs, *Proc. Cambridge Philos. Soc.* **34**, 100 (1938).
7. E. H. Sondheimer, *Adv. Phys.* **1**, 1 (1952).
8. A. F. Mayadas, M. Shatzkes, and M. Janak, *Appl. Phys. Lett.* **14**, 345 (1969).
9. A. F. Mayadas and M. Shatzkes, *Phys. Rev. B* **1**, 1382 (1970).

4 Experimental Results and Discussion

Three related topics have been investigated and will be discussed in this chapter. Initially, the remanent domain structures of planar wires are presented. We will show the influence of the geometrical factor on domain structures and describe the evolution of magnetic domain structure according to the domain theory. Then, the investigation of the magnetization reversal for planar wires has been performed by magneto-transport measurements and domain images. In this part, magnetoresistance of planar wires is analyzed in detail. Furthermore, we make a comparison with the theoretical prediction in the magnetization reversal mode to explore the mechanism for the switching behavior. According to the results of individual wires, we construct the centipede-like patterns of crossing two planar wires to study the intrinsic domain wall resistance. The dependence of domain wall resistance with the relative angle of a domain wall is revealed.



4-1 Remanent domain structure in individual wires

As mentioned in section 2-1-2, the domain structure of a soft magnetic material is dominated by the geometrical factors, such as the shape and the aspect ratio, $m=L/w$. For an elongated ellipsoid, there is a critical size separating the single domain and the multi-domain. As for a planar wire, because of the stray field free consideration, domain structures will be induced naturally by the edge and the corner. A number of groups investigated these edge induced domain patterns using Lorentz microscopy [1] and Magnetic force microscope (MFM) [2,3]. They found that when the aspect ratio of a rectangular element is increased, the domain structure will be varied from the complex multi-domain, through the flux closure patterns, and then the quasingle

domain with flux closure ends, to the single domain [2]. In order to obtain a pure single domain, the edge induced domain at the ends can be eliminated by the shape of a point end or the reduction of a wire width below the single domain limit. Although the domain structure transition has been reported in the polycrystalline Co or permalloy (Py) patterned systems, there is lack of discussion in the several micrometers long as well as high aspect ratio wire system. Here, we discuss the remanent domain structure of Py wires beginning with their geometrical description and then, express their domain structures upon their MFM images.

4-1-1 Geometrical description

Two series of Py wires with 20 and 5 μm long (l) and various widths (w) from 10 to 0.1 μm were fabricated. The topography of wires can be exactly observed using SEM and the profile of wires can be detected via AFM images. For wire widths larger than 0.15 μm , the wires have only marginal edge roughness with no tear-off edges at all and have sharp corners at the ends, as seen in Fig. 4-1(a). In contrast, Fig. 4-1(b) shows a bullet-like end of a 0.1 μm wide wire. The cross-section of wires is demonstrated in Fig. 4-1(c). The gradual profile at the edge is caused by the insufficient amplitude of the oscillated AFM tip when the tip suffers an abrupt difference of height. Although there is a gradual profile at the edge, the cross-section is rectangular when wire widths are larger than 0.15 μm implying that our Py wires belong to the kind of planar wires.

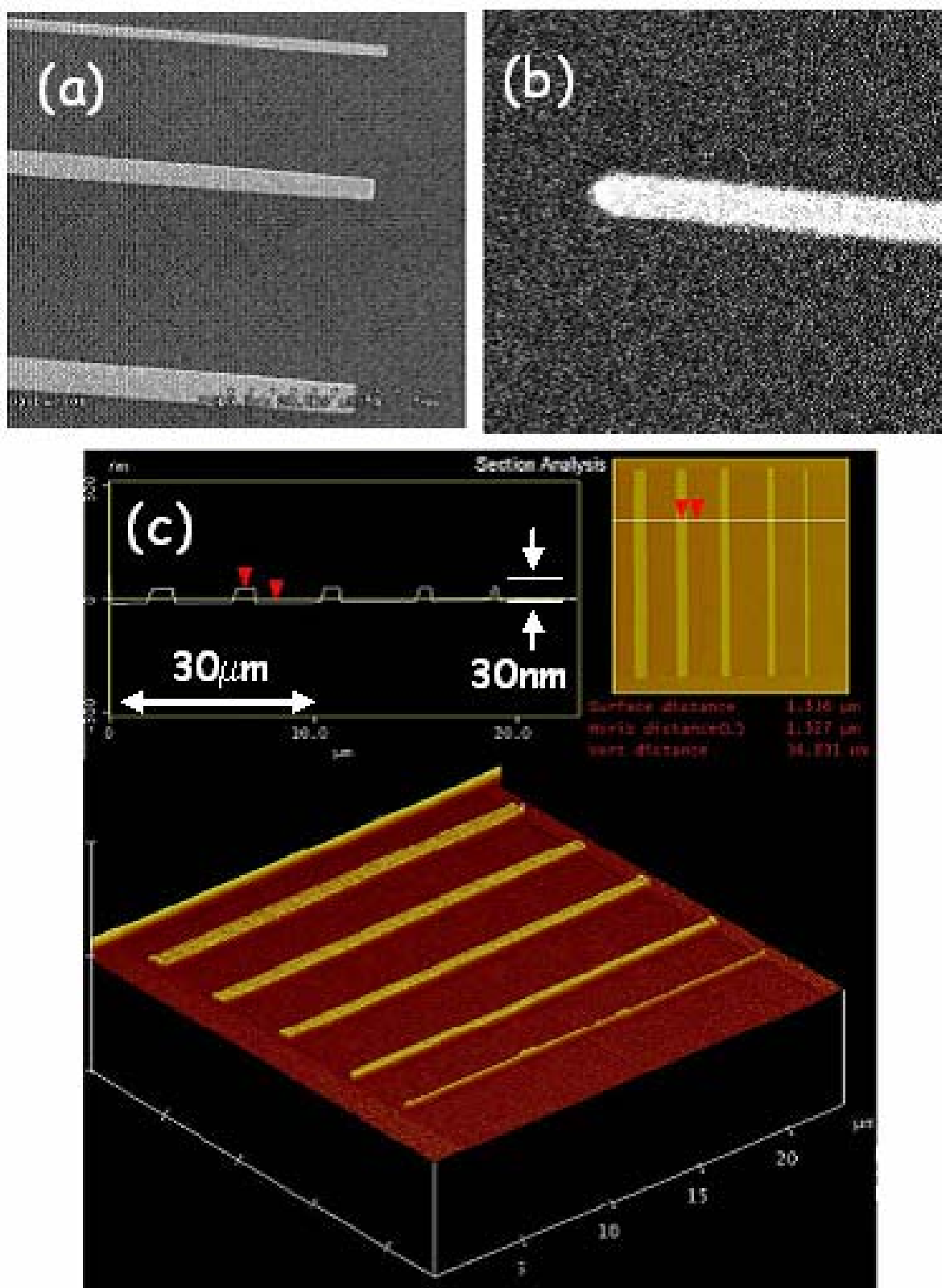


Figure 4-1: The topography of our permalloy wires. (a)(b) SEM images of wires with 0.2, 0.6, and 1.1 μm (a) and 0.1 μm (b) in width. (c) An AFM image of a series of wires.

4-1-2 Domain structure

In order to observe the remanent domain structures of the Py wires, MFM is conducted at room temperature. Before scanning, the sample is exposed to a 1 Tesla magnetic field along the wire axis. As shown in Fig. 4-2(a) for a series of $20\mu\text{m}$ long Py wires, the magnetic contrast configurations in wires obviously indicate the remanent domain structures can be classified into three groups. When the aspect ratio $m(=l/w)<10$, a multi-domain is observed. As seen in Fig. 4-2(a), there are several magnetic contrasts in the three leftmost wires ($w=11, 5.6,$ and $2.4\mu\text{m}$). When $m\geq 40$, the characteristics is the single domain. As seen in Fig. 4-2(a), only two contrasts at both ends appear in the rightmost wire ($w=0.3\mu\text{m}$). Beside the single- and multi-domain states, another magnetic structure is evident. For other two wires ($w=1.3$ and $0.7\mu\text{m}$) in Fig. 4-2(a), there are vortices or partial wall structures located at the ends of wires, but the majority of the wire is composed of the uniform magnetization moment. This vortex structure can be clearly seen in the enlargement of the MFM image, also shown in Fig. 4-2(a).

Clearly, this evolution of the domain structure for Py wires is closely related to m . A schematic of phase diagram determined by MFM images and magneto-transport is presented in Fig. 4-2(c). The remanent magnetic structure indeed depends on the aspect ratio(m) of the wire. Furthermore, the other set of Py wires of $5\mu\text{m}$ long, 30nm thick, and various widths, was prepared to check the consistency. As shown in Fig. 4-2(b), the same scenario is observed that a multi-domain structure for $m<5$, a single domain for $m>20$, and the intermediate region in between them ($5<m<20$). These results are roughly in agreement with the theoretical prediction which considers the lowest free energy state for prolate spheroids at remanence. The details of this theory

can be found in section 2-1-2. The dashed line in Fig. 4-2(c) is obtained by Eq. (2-14).

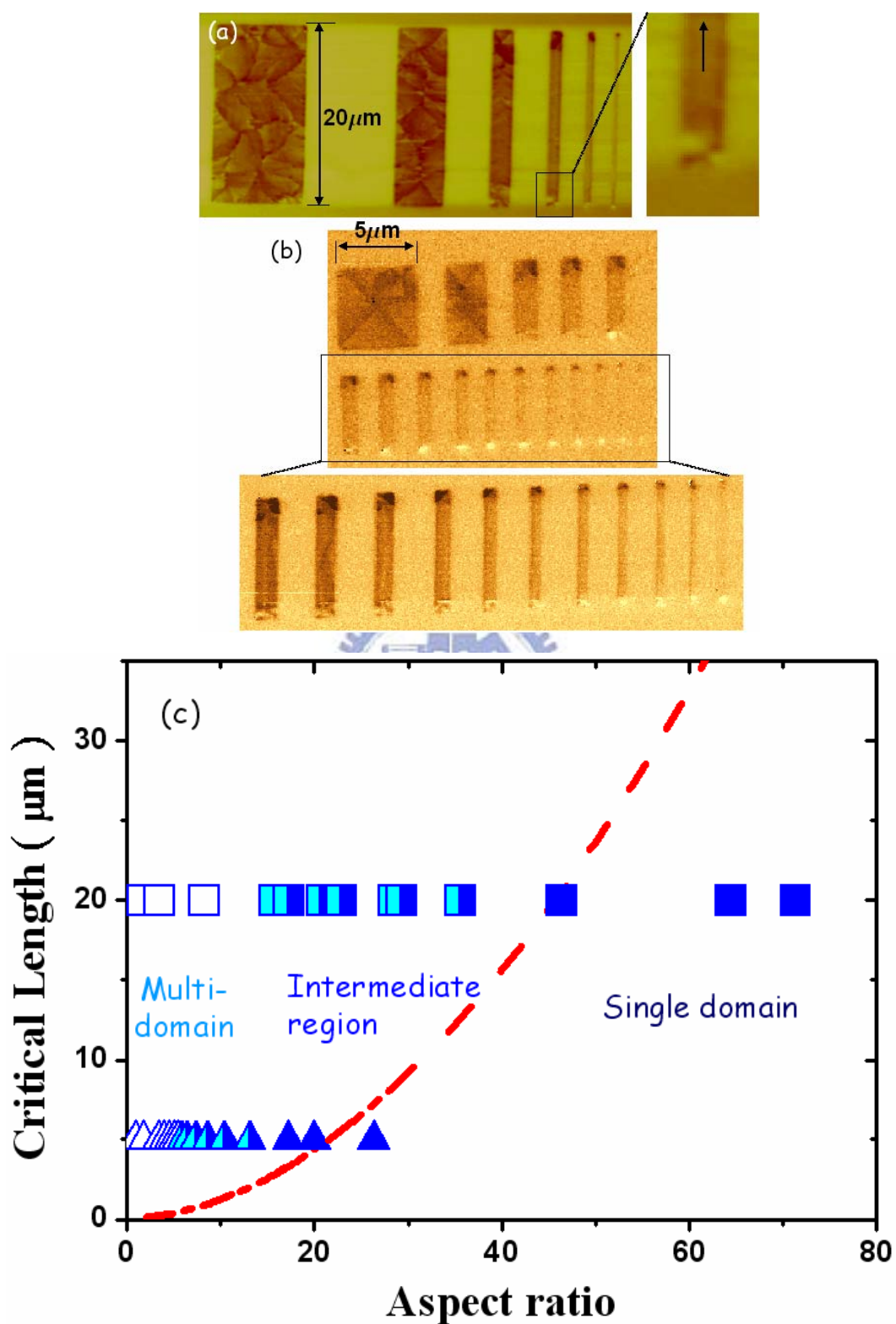


Figure 4-2: (a)(b) Remanent MFM images of two series of Py wires with 20 and 5 μm long and various widths. (c) The remanent domain structure as a function of the aspect ratio m and the length l . The dashed line is the theoretical prediction according to the Aharoni model.

4-2 Magnetization reversal in individual wires

Magnetization reversal of a wire consists of the following two processes: the dynamic behavior at the switching field (H_{sw}) where the magnetization has a significant change in an instant ($<\mu\text{sec}$), and the time-independent behavior elsewhere. The former has been investigated using time-resolved scanning Kerr microscopy, allowing direct insight into the spatiotemporal evolution of the switching process [4,5]. A precessional magnetization motion and a domain wall oscillation were observed soon after the magnetization was reversed at the H_{sw} for a Py planar wire by Freeman *et al.* [5]. The dynamic behavior is of fundamental interest, but is not the purpose of our investigation in this thesis. Until now, there is still argument about the time-independent behavior of magnetization reversal. What mechanism such as coherent rotation, magnetization curling, magnetization buckling, and the propagation of domain walls dominate the reversal in various systems [6-11]. In Py wire systems, Goolaup *et al.* performed the angular dependence of magnetization hysteresis loop measurements for a series of Py wire array formed by photolithography and claimed that the reversal mechanisms will be changed from the coherent rotation to the magnetization curling with increasing thickness of wires [8]. Oliveira *et al.* performed the angular dependence of MR measurements for Py dumbbell-like structures fabricated by AFM mechanically transfer [11]. The reversal process of the rod of this structure was attributed to the magnetization buckling mode by analyzing the angular dependence of the switching field. In Ni wire systems, Wegrowe *et al.* also analyzed the relationship of switching field with angle for individual wires fabricated by electrochemical deposition [6]. They pointed out that the reversal is dominated by the magnetization curling but is through the local curling. This aspect was confirmed in

the hysteresis loop measurements by Wernsdorfer *et al.*, using micro-SQUID [12]. In Co wire systems, Leven *et al.* carried out MR measurements and micromagnetic simulation in a series of planar Co wires [7]. They argued that the magnetization reversal is completed via the propagation of domain walls. However, the irreversible MR curve does not follow this reversal. In addition, Gao *et al.* declared that the wire width dependence on the H_{sw} can be well described according to the magnetization buckling for Fe₃Pt wires [9].

On the other hand, the formation of the end domain due to the stray field free consideration for a planar wire is claimed to influence the reversal [13,14]. For a wide wire, a flux closure structure presents a reversed domain, even in the absence of a reversing field, and growth of this domain plays a major role in the reversal process. By contrast, there is no end domain in a narrow wire but the magnetization close to the wire ends is nearly orthogonal to the wire axis, forming a transverse domain structure. The propagation of this structure is suggested as being an important mechanism in the reversal process. Later, several reports [15-17] using the micro-magnetic simulation method show that for an elongated particle or a planar wire, the complete magnetization moment rotation during the reversal is not always uniform. The magnetization reversal can occur through a creation of domain wall pairs and then sweep across a wire. Another approach [18,19] was based on the spin transfer effect, where a small torque applied using a pulse current or a pulse field was expected to excite the magnetization and create a metastable state during reversal. This method allows direct images of the domain walls within a wire. However, there may be variations when applying uniform magnetic fields during the reversal, due to the fewer amounts of torque and the local thermal heating.

In the experiments, magnetic powders [20,21] were initially used.

Electrochemical deposition [6,12,15] then enabled the production of extended cylinders with a diameter of less than 100nm. This process allows the study of the reversal for a single domain element. However, comparing with the e-beam lithography [7,22], there are some intrinsic problems need to be concerned such as the interaction between the wires and the spatial alignment with the external field in the use of nanoporous membrane for electrochemical deposition [6]. The reversal properties of an individual nanowire have been investigated using several methods, such as micro-SQUID [12], electron Lorentz microscopy or holography [14,23], Kerr microscopy, MFM [24-27], and magnetoresistance (MR) measurement [6,7]. Most of the previous experiments focus on the behavior exhibited by the entire wire. Only a few experiments were performed to study the reversal by examining different parts of a wire [10,27-29].

Our work is mainly devoted to study the magnetization reversal processes in a series of micron and submicron wide Py planar wires. The low temperature magnetoresistance measurements, together with the MFM image performed in magnetic fields, were carried out.

4-2-1 Magnetoresistance and in field MFM images

As mentioned previously, shape anisotropy plays a crucial role in domain structure of a wire. The remanent domain structure is decided by the aspect ratio and the length of a wire. Our Py wires are classified into three categories, regarding their remanent domain structures. The reversal mechanisms for all wires were investigated using low temperature MR measurements. The MR curves together with the MFM images are demonstrated to explore the magnetization reversal in turn upon their

classifications. In this section, we initially introduce the pattern designed to carry out the MR measurement. Then, MR curves for wires in multi-domain, cross-over region, and single domain are described.

In order to exclude the influence of magnetic contacts on the reversal process of Py wires, two-step e-beam lithography was used to fabricate the non-magnetic gold contacts that are attached to the wires. The details of the fabrication process can be found in section 3-1-2. Fig. 4-3 shows a SEM image of one typical wire structure. The high contrast gold contacts are used for the four-terminal ac MR measurements. A number of contacts are designed for the investigation of the different segments of the wire. The distance between voltage contacts is 4, 4, and $3\mu\text{m}$ at the center (C), arm (A) and near-end (E) of a wire, respectively.

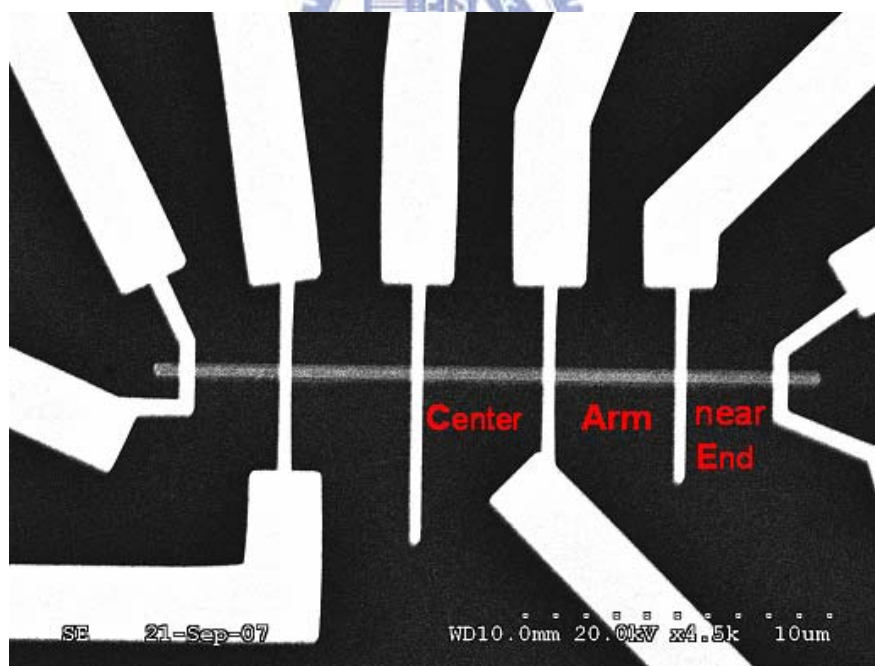


Figure 4-3: A SEM image of a typical Py wire device. The gray wire is Py and the brighter area is Au. Three segments of a wire are labeled by C, A, and E from the center to end.

In Py wires, anisotropic magnetoresistance (AMR) provides the most contribution to MR. AMR resulted from the anisotropic spin-orbital scattering causes the dependence of the resistance on the angle between the current and the magnetization. For a wire, the expression of AMR can be written as:

$$R(H, \phi) = R_{\perp} + \Delta R_{AMR} \cos^2(\phi(H, \theta)) \quad (4-1)$$

where θ and ϕ are the angles of applied field and magnetization, respectively, with respect to the axis of a wire. $\Delta R_{AMR} = R_{//} - R_{\perp}$, where $R_{//}$ and R_{\perp} are the resistances when the saturated magnetization is parallel and perpendicular to the current, respectively. In our study, the direction of the current is always along the axis of a wire. At a saturation field (H_{sat}), the entire magnetic moment lies parallel to the direction of the field, resulting in the situation where $\theta = \phi$, and hence, AMR is expected to be proportional to $\cos^2\theta$. Fig. 4-4 shows three saturated resistances against θ for wires with widths of 10, 2, and 0.7 μm . All data have an uncertainty in angle within 1.5°. As can be seen, three curves satisfy the relationship of $\cos^2\theta$ plotted as the dashed lines. As for narrower wires ($w \leq 0.5 \mu\text{m}$), although the H_{sat} increases rapidly and may be larger than 2.3kOe, which our electromagnet can supply, their MR curves are within our expectation. The saturated resistances obtained by the extrapolation of MR curves are still consistent with the $\cos^2\theta$ relation and the AMR ratio of 1-2% holds.

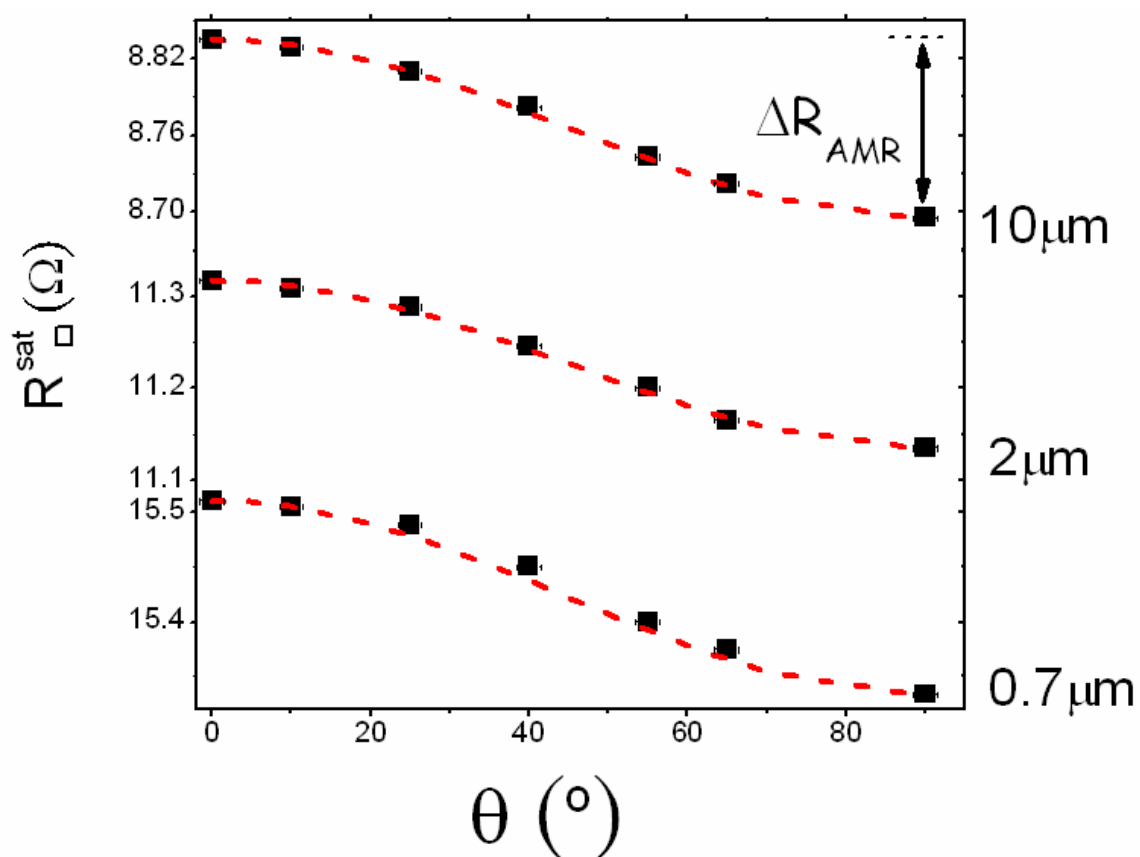


Figure 4-4: The saturated sheet resistance as a function of θ for three wires with widths of $w=10$, 2 , and $0.7\mu\text{m}$. The data follows the relationship of $\cos^2\theta$ presented as the dashed lines.

Multi-domain wires

The typical LMR and TMR curves of a sample with a multi-domain state are demonstrated in Fig. 4-5(a). For the LMR ($\theta=0^\circ$), the resistance is almost constant until the magnetic field is reduced close to zero. When the field is switched to the opposite direction, the resistance decreases rapidly and there is a clear hysteresis loop, forming a butterfly-like pattern. As for the TMR ($\theta=90^\circ$), the resistance increases with decreasing magnetic field, forming a volcano-like shape. The minima of the

LMR curve are comparable to the maxima of the TMR curve, indicating that there is a similar magnetic configuration at the coercive field (H_c) corresponding to the reversal behavior in the magnetization hysteresis loop. Although the remanent domain structure of a $10\mu\text{m}$ wide wire is a multi-domain, a weak shape anisotropy causes an ordered multi-domain state, resulting in that the remanent resistance is slightly less than the saturated resistance for LMR and is a maximum of each MR curve for any θ except for $\theta = 90^\circ$, as seen in Fig. 4-5(b). The reversal process will be discussed in more detail below.

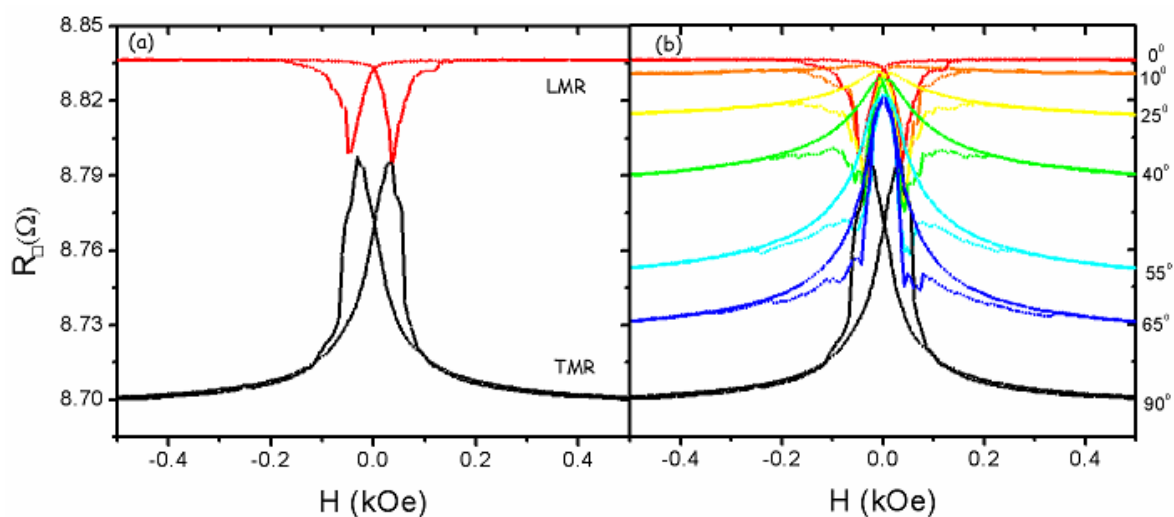


Figure 4-5: (a) The LMR and TMR curves of a $10\mu\text{m}$ wide wire. (b) The MR curves of various angle θ from 0° to 90° .

MFM images of the same sized wire were taken at some characteristic points on the hysteresis loop of MR to examine the reversal process. As seen in Fig. 4-6, when the direction of a magnetic field is parallel to the wire axis ($\theta = 0^\circ$), all magnetic moments are forced in the direction of the field at H_{sat} resulting in a single domain with the largest magnetostatic energy and the maximum resistance (point i). As the strength of the magnetic field is decreased toward zero, in order to reduce the magnetostatic energy, certain moments should start to rotate away from the direction

of the field resulting in a multi-domain state with less resistance (point ii). When the field is changed to the opposite direction, the domain expansion causes more magnetic moments perpendicular to the direction of the field resulting in an ordered multi-domain state with much less resistance (point iii). Until the field is beyond the coercive field (H_c) the amount of moment along the field direction increases resulting in a rapid increase in resistance. Then, as the field approaches H_{sat} , the propagation of domain walls and the rotation of magnetic moment are accompanied by an irregular increase in resistance characterized by pinning plateaus (point iv). Until the field is increased to beyond H_{sat} , all moments are forced to align with the field and the sample returns to the single domain state (point v). The MR curve in company with MFM images can well describe the magnetization reversal process of multi-domain wires. Consequently, a departure ratio for a MR curve can be written as: $\Delta R(= R(H) - R(H_{sat})) / \Delta R_{AMR}$. This ratio reflects the effective percentage of magnetic moments deviating from the axis of a wire. Here, the ratio of LMR is about 2.5% at remanence and 38% at H_c . The hysteresis loops of the center and near-end parts of the wire are plotted as the solid and open symbols in Fig. 4-6. Both curves are very alike indicating that the multi-domain state could be a macroscopically homogeneous. Samples wider than $2\mu\text{m}$ show similar behaviors symbolized as a multi-domain state.

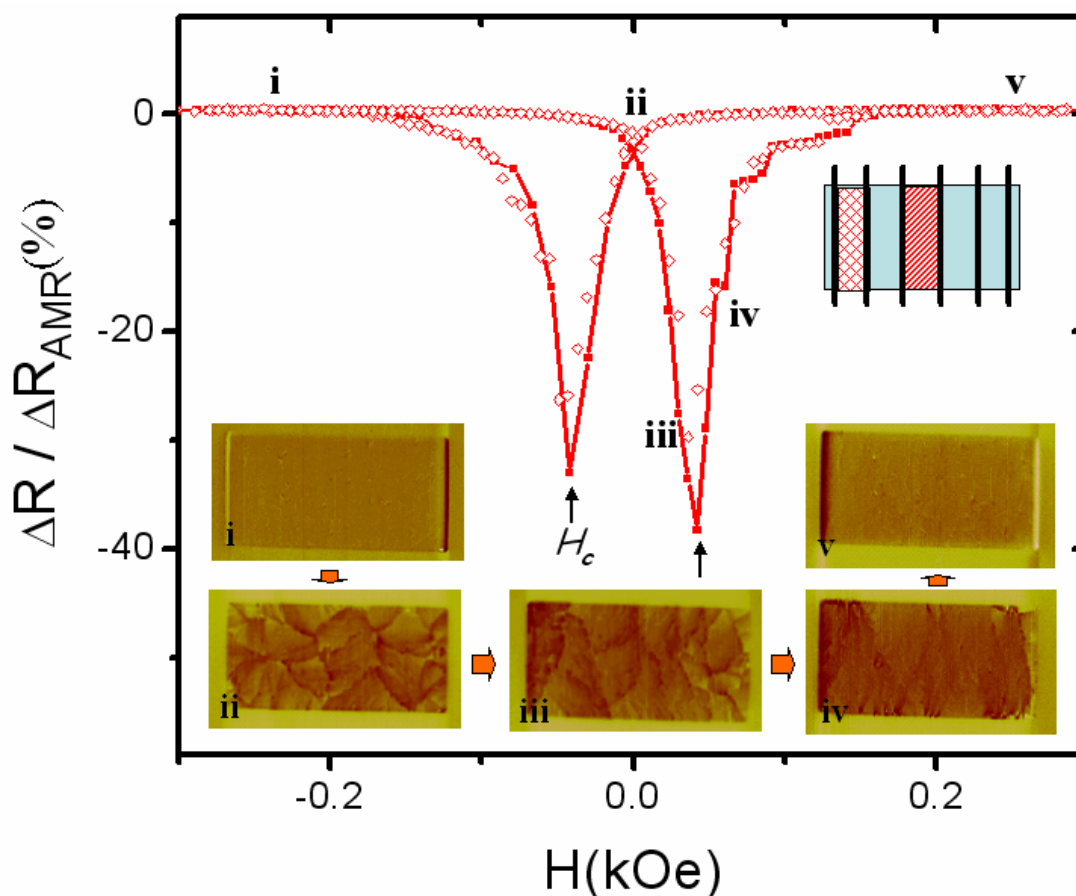


Figure 4-6: The enlargement of LMR curves of a $10\mu\text{m}$ wide wire. The open and solid symbols are data for the near-end and center regions, respectively. Inset: MFM images labeled by (i)-(v) describe domain structure at the characteristic points on the hysteresis loop.

Single domain wires

When wire width is less than $0.5\mu\text{m}$, corresponding to the aspect ratio larger than 40, the wire is in the single domain state. The typical MR curves of a single domain wire at different angles θ are demonstrated in Fig. 4-7. Overall, there are large reversibly bell-shaped negative MR curves. For TMR ($\theta = 90^\circ$), the MR decreases with magnetic field in a parabolic behavior. When the field is decreased from saturation the resistance increases smoothly. The resistance is a maximum as the magnetic field is reduced to zero and remains the same despite of angles θ . A slight

increase of the field in the opposite direction leads to the hysteresis in the curve. Here, in addition to the reversible MR, there is an irreversible jump in low magnetic field. As shown in Fig. 4-7(a), zoom of the low field MR, an irreversibly V-shaped discontinuity in low field, can be clearly found for all angles $\theta < 90^\circ$. Compared to the MR curves of multi-domain samples, beside a rather small hysteresis loop in low magnetic fields, the MR curve is almost reversible elsewhere. The remanent resistance is constantly equal to the saturated resistance of LMR ($\theta = 0^\circ$) for different magnetic field directions (θ).

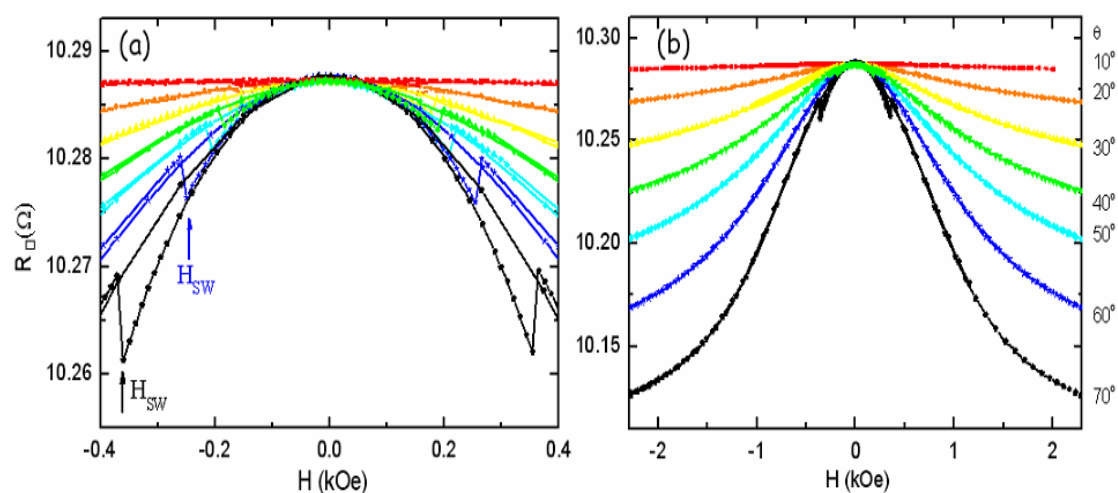


Figure 4-7: The MR curves of a $0.43\mu\text{m}$ wide wire for different magnetic field directions at $T=10\text{ K}$. (a) The enlargement of MR curves at low magnetic field. (b) The MR curves at $\theta = 10, 20, 30, 40, 50, 60,$ and 70 in degrees from top to bottom, respectively.

MR curves together with MFM images of the same sized wire taken at the characteristic points on the hysteresis loops are used to examine the reversal process. For clarity, Fig. 4-8 illustrates the enlargement of MR curves in low magnetic field for a wire with $w=0.35\mu\text{m}$ at $\theta = 70^\circ$. There is a single jump in the MR curve, signifying that the reversal of a single domain sample is completed in an abrupt action. Furthermore, a small ΔR , corresponding to a little departure ratio, suggests that

magnetic moments lie along the easy axis very well during the reversal. The insets of Fig. 4-8 show a series of MFM images labeled as (i)-(v). There is no formation of domain structures in the main body but only the switch in the magnetic contrast at both ends of the wire. Occurrence of the switching is very abrupt, within 10e in magnetic state. No static domain structures are observed during the reversal. MR curves measured at different parts of the wire are almost the same as shown in Fig. 4-8. Three MR curves have a low departure ratio of magnetoresistance $\sim 5\%$ at $H_{sw} \pm 0.63\text{kOe}$ suggesting that there is a collective motion of the whole moment during the reversal.

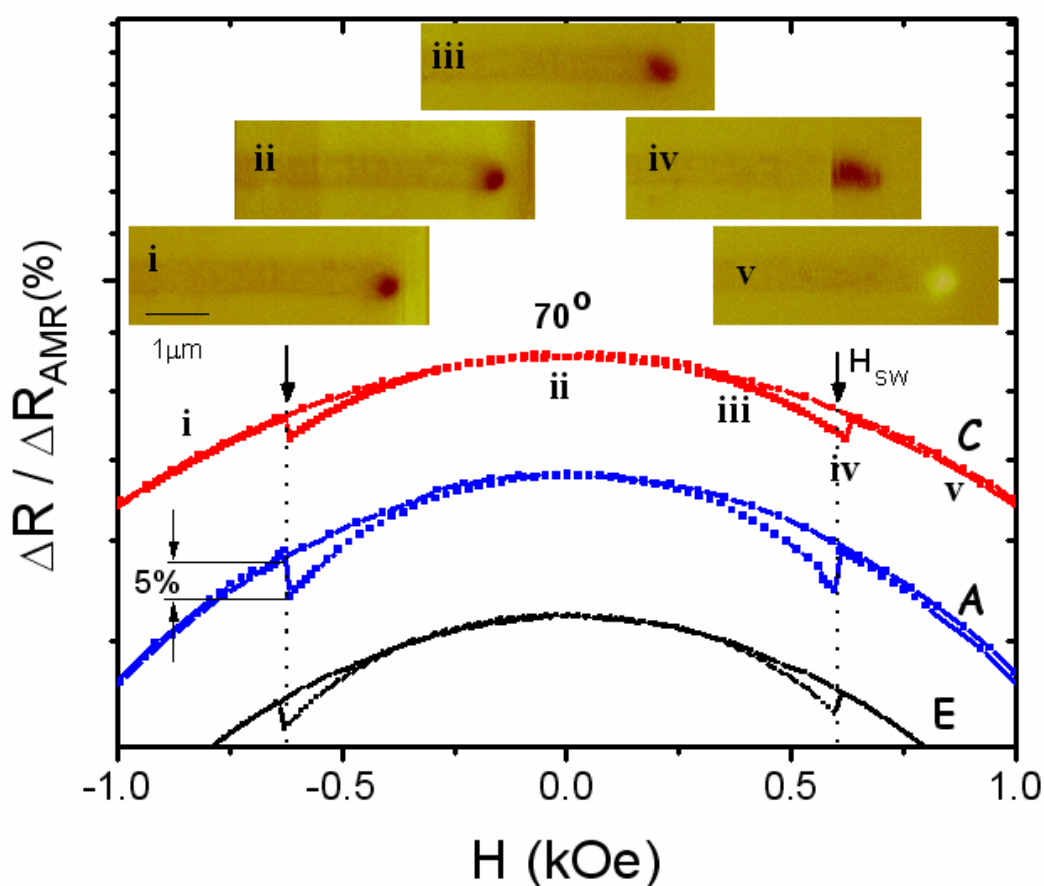


Figure 4-8: Three MR curves measured at C, A, and E regions for a $0.35\mu\text{m}$ wide wire at $\theta = 70^\circ$. MFM images labeled by (i)-(v) describe domain structure at the characteristic points on the hysteresis loop.

4-2-2 Analysis of Magnetoresistance

In this section, we analyze the MR curves for the wire which is not in the multi-domain state. The MR curves, except for $\theta = 90^\circ$, consist of two parts: the reversible and irreversible parts. Fig. 4-9 shows two MR curves of a $1.9\mu\text{m}$ wide wire for $\theta = 30^\circ$ and 60° . Both curves exhibit a bell shape background and a certain deviation in low fields. The bell shape background which is reversible as the field is swept from H_{sat} to zero indicates the reversal process for the rotation of magnetization to the easy axis. When the field is swept from zero to H_{sw} , the departure of MR curves from the background, which is called an irreversible part, specifies the reversal process for the magnetization to overcome an anisotropy induced barrier.

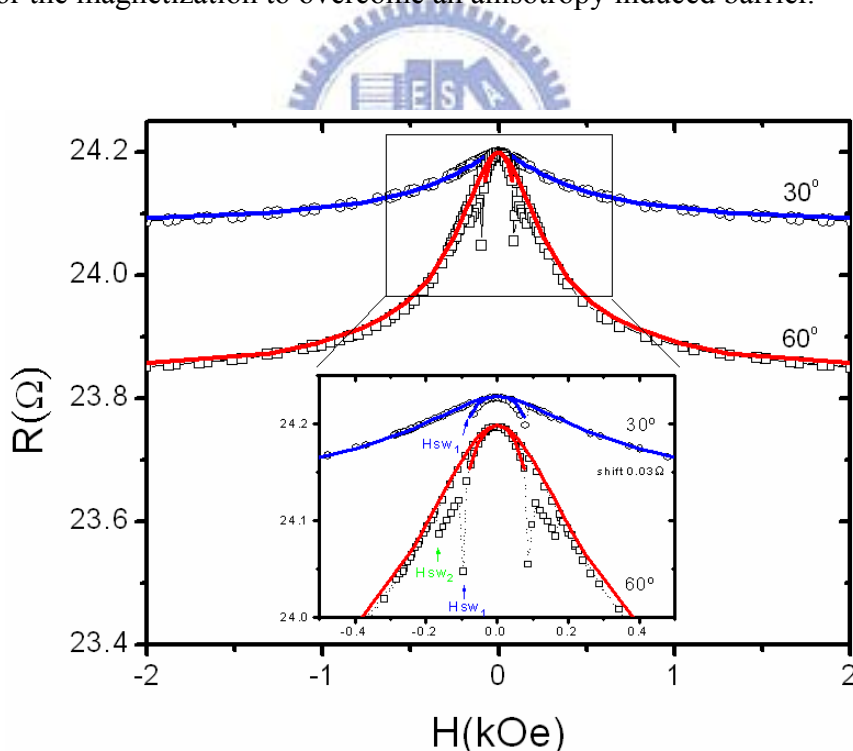


Figure 4-9: Two magnetoresistance curves of a $1.9\mu\text{m}$ wide wire for $\theta = 30^\circ$ and 60° . The solid lines are the fit of MR curves according to the coherent rotation as well as AMR effect. The inset is an enlargement of the MR curves in low field.

Reversible Part

The simple uniform rotation model based on the SW model is developed to analyze MR curves. The SW model has been described in section 2-2-1. Constraint for the equilibrium state of the magnetization in an external field is that the total energy is a minimum leading to the following equation [30]:

$$2h \sin(\theta - \phi) = \sin(2\phi) \quad (4-2)$$

The normalized field $h = \mu_0 H M_s / 2\mu_0 K$, K is the anisotropy constant, M_s is the saturated magnetization. By solving Eq. (4-2) for fixed h and θ values, the relationship between $\cos^2\phi$ and h for a given magnetic field can be obtained. Combining with Eq. (4-1), the resistance as a function of the magnetic field can be developed. In Fig. 4-9, red and blue lines are obtained by the process. As seen, both MR background curves for $\theta = 30^\circ$ and 60° fall on the theoretical curves suggesting that the reversal from saturation to remanence exhibits the expected behavior based on the SW model. This result has also been observed in Ni wire systems [6].

For TMR ($\theta = 90^\circ$), the combined function can be reduced to:

$$R(H) = R_{//} - (R_{//} - R_{\perp}) \left(\frac{M_s H}{2K_u} \right)^2 \quad (4-3)$$

The uniaxial anisotropy constant K_u may be quantified by the fit of TMR to Eq. (4-3). Fig. 4-10(a) shows a TMR curve of a $1\mu\text{m}$ wide wire and the best fit represented as the solid line. K_u was extracted as $1.63 \times 10^5 \text{ erg/cm}^3$. For wire with width smaller than $2\mu\text{m}$, the value of K_u is always larger than $1 \times 10^5 \text{ erg/cm}^3$ which is larger than the crystalline anisotropy constant by two orders of magnitude. As shown in Fig. 4-10(b), K_u rapidly decreases with increasing wire width as $w < 1.2\mu\text{m}$ and has a saturation as $w > 1.2\mu\text{m}$. In a Co wire system, the relationship is claimed to follow the theoretical

description based on elliptically shape anisotropy [31], but the dashed line of this theoretical expectation can not apply to all our data, especially for $w > 1\mu\text{m}$, as seen in Fig. 4-10(b). The dashed line is calculated by the relationship of $K_u \sim N_b M_s^2$, where N_b is obtained by Eq. (2-7). The difference between data and theoretical fit can be clearly displayed in the log-log plot. For wire with medium widths, K_u follows the theoretical prediction and exhibits a gradual rise in a reciprocal relation. Wider wire with $w > 1.2\mu\text{m}$ has a constant K_u ($\sim 1 \times 10^5 \text{ erg/cm}^3$) insensitive to w . For narrower wires, K_u deviates from the dashed line and seems to be less than the theoretical prediction. The deviation of theoretical expectation from data may be due to that our sample is planar instead of ellipsoidal and the elliptical approximation is certainly not good for wider wires.

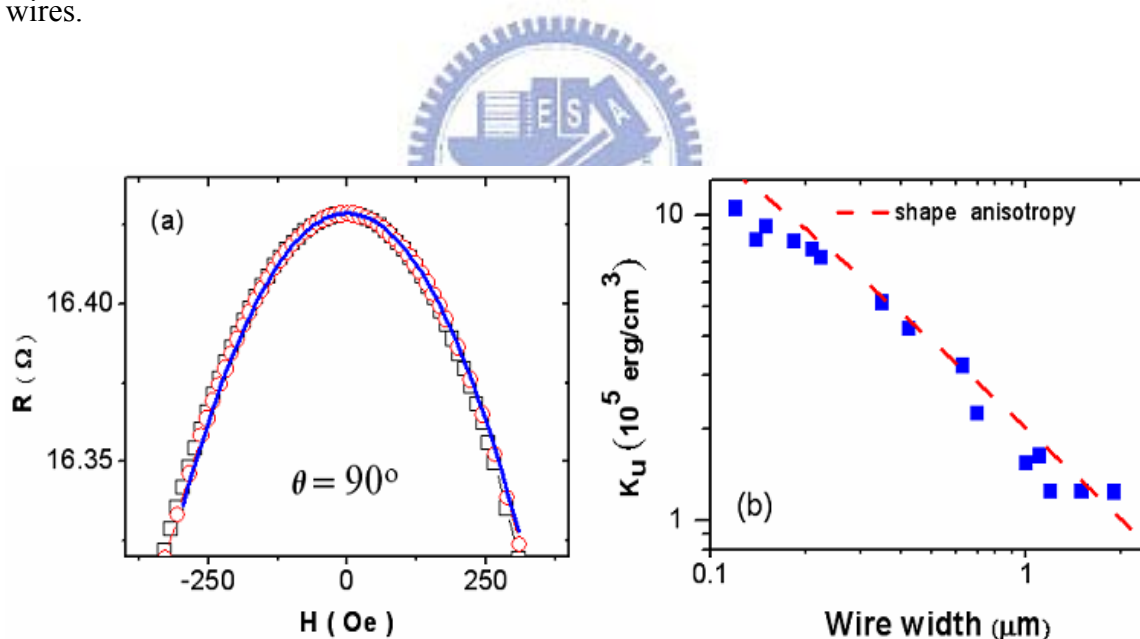


Figure 4-10: (a) TMR curve of a $1\mu\text{m}$ wide Py wire. The solid line is the best fit of TMR curve by Eq. (4-3). (b) The uniaxial anisotropic constants as a function of wire width. The dashed line is the theoretical prediction according to the elliptically shape anisotropy.

Irreversible Part

The irreversible part of the MR curve reveals the reversal process from remanence to H_{sw} . As mentioned in the previous section, the domain expansion and the domain wall propagation causes an irregular irreversible part for a multi-domain sample. In contrast, the reversal is completed via one step leading to a V-shaped discontinuity in small fields for a single domain sample. Fig. 4-11 shows a series of LMR for Py wires of various width ($w < 2\mu\text{m}$). As magnetic field is decreased from saturation to zero, the longitudinal resistance remains the same for such a series of wires while decreases slightly for wider wires of multi-domain structures (see Fig. 4-6). As the magnetic field is reversed and increases to near H_{sw} , the longitudinal resistance starts to have a clearly continuous drop. When the magnetic field reaches H_{sw} , the longitudinal resistance jumps back to the saturation value in an abrupt step. This LMR behavior symbolized for a typical single domain sample. Two topmost wires in Fig. 4-11 have the irreversible behavior of a V-shape discontinuity, however the departure ratios are too small to resolve in this scale here. For the other wide wires, the reversal is even completed via a single jump but there are extra features. As seen in Fig. 4-11, for instant, the irreversible MR curve of a $1.5\mu\text{m}$ wide wire shows a complex behavior, with a gradual decrease when $H < 50\text{Oe}$, a rapid descent when $50 < H < 90\text{Oe}$, and a linear decrease before H_{sw} , implying that additional micro-magnetic domains are formed during the reversal. Would this evolution of domain configuration be the same in different parts of the wire? This spatial dependence of MR behavior and the reversal mechanism will be discussed in detail in the next section.

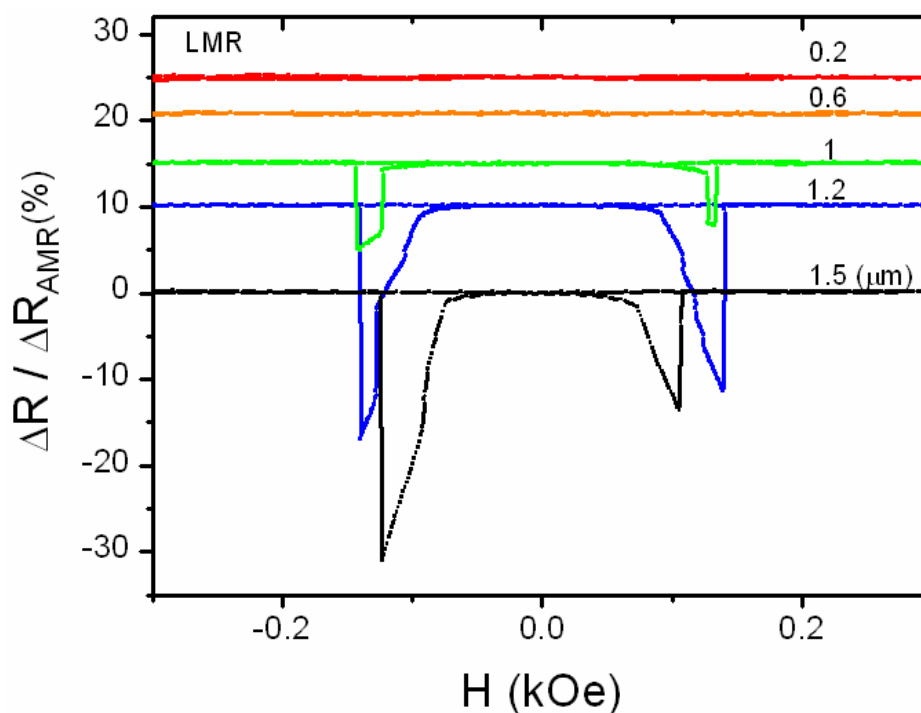
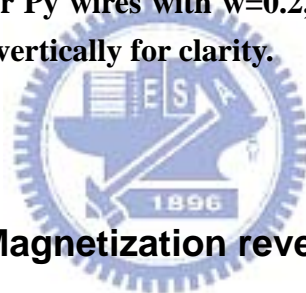


Figure 4-11: LMR curves for Py wires with $w=0.2, 0.6, 1, 1.2,$ and $1.5\mu\text{m}$ (top to bottom). Curves are shifted vertically for clarity.



4-2-3 Discussion of Magnetization reversal Mechanisms

As discussed in previous sections, the magnetization reversal from the saturation to the remanence occurs via the coherent rotation. As to the process from the remanence to switching, the reversal need to be made a further investigation, especially for wires in the intermediate region ($10 < m < 40$). This behavior will be examined by the in field MFM and the MR measurement.

For a series of $20\mu\text{m}$ long Py wires, the remanent domain structures have been shown in Fig. 4-2(a). Subsequently in-field MFM images were taken in the same series of Py wires. Fig. 4-12(a) and (b) exhibit the domain structures at $H=30$ and 50Oe , respectively. The magnetic field is applied in the opposite direction of the remanent magnetization. There are several magnetic contrasts in the three leftmost

wires ($w=11, 5.6, \text{ and } 2.4\mu\text{m}$) in Fig. 4-12(a). As the magnetic field is increased to be close to the coercive field, there is an ordered multi-domain state with a few contrasts as shown in Fig. 4-12(b). This reversal process demonstrates the typical multi-domain reversal behavior. On the other hand, as seen in Fig. 4-12(a) and (b), only two spots at both ends appear in the rightmost wire ($w=0.3\mu\text{m}$). This two end-spot feature will be maintained until the field is beyond 206Oe , H_{sw} of the wire. For other two wires ($w=1.3 \text{ and } 0.7\mu\text{m}$), there is a remarkable domain expansion in Fig. 4-2(a) and (b). As mentioned in section 4-1-2, closure domains already exist at both ends of the wire at remanence. The end domain extends to whole volume for the $1.3\mu\text{m}$ wide wire, but only 23% of the volume for the $0.7\mu\text{m}$ wide wire at $H=50\text{Oe}$. The relationship between the end domain expansion and wire width will be discussed in the following.

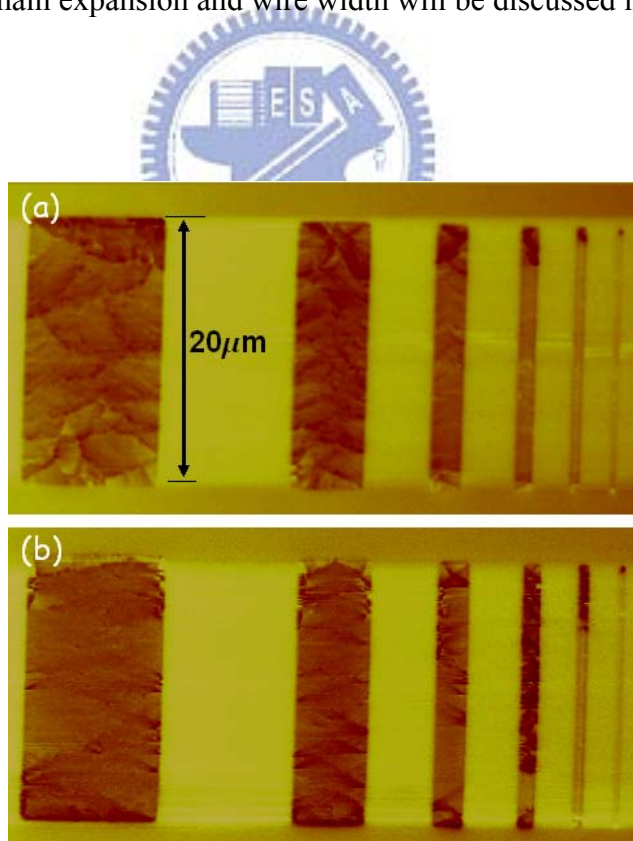


Figure 4-12: In-field MFM images of a series of Py wires with $20\mu\text{m}$ long and various widths ($w=11, 5.6, 2.4, 1.3, 0.7, \text{ and } 0.3\mu\text{m}$) in the magnetic fields of (a) 30Oe and (b) 50Oe .

Wires in the intermediate region

A series of MFM images of about one half of the $1.2\mu\text{m}$ wide sample together with the LMR at different segments of the wire of the same width are shown in Fig. 4-13(a). When the magnetic field sweeps back to zero from the saturation field, the nearly single domain structure is barely changed and resistances of different parts are the same. A vortex-like end is present but persists as shown in MFM image (ii). When the magnetic field is changed to the opposite direction and smoothly increased, the domain of the wire end starts to expand. As we see, at point (iii), the end domain grows slightly ($\sim 2.2\mu\text{m}$ from one end) to cover about 40% of the near-end part and the resistance of this part drops a little more than two other parts of the wire. With a slight increase of magnetic field, from point (iii) to (iv), the end domain expands suddenly and almost through the whole volume. However, the contrast in regions is weak indicating all moments in different regions have slight changes coincidentally. When the magnetic field reaches the H_{sw} , point (iv) to (v), the magnetic state switches suddenly back to the single domain state with the only two contrast spots in both ends. According to the evolution of magnetic configuration obtained from MFM images, the LMRs would be expected. From point (iii) through (iv) to (v) saturation, LMR in different regions have similar behaviors and may change little through several reversals. Meanwhile, in low magnetic field ($<100\text{Oe}$), the resistance of the near-end region always drops a little more than two other regions. Wires with $1.2\leq w < 2\mu\text{m}$, the magnetic reversal behavior is similar. LMR of the $1.5\mu\text{m}$ wide wire is also shown in Fig. 4-13(b). The main feature is analogous to the $1.2\mu\text{m}$ wide wire.

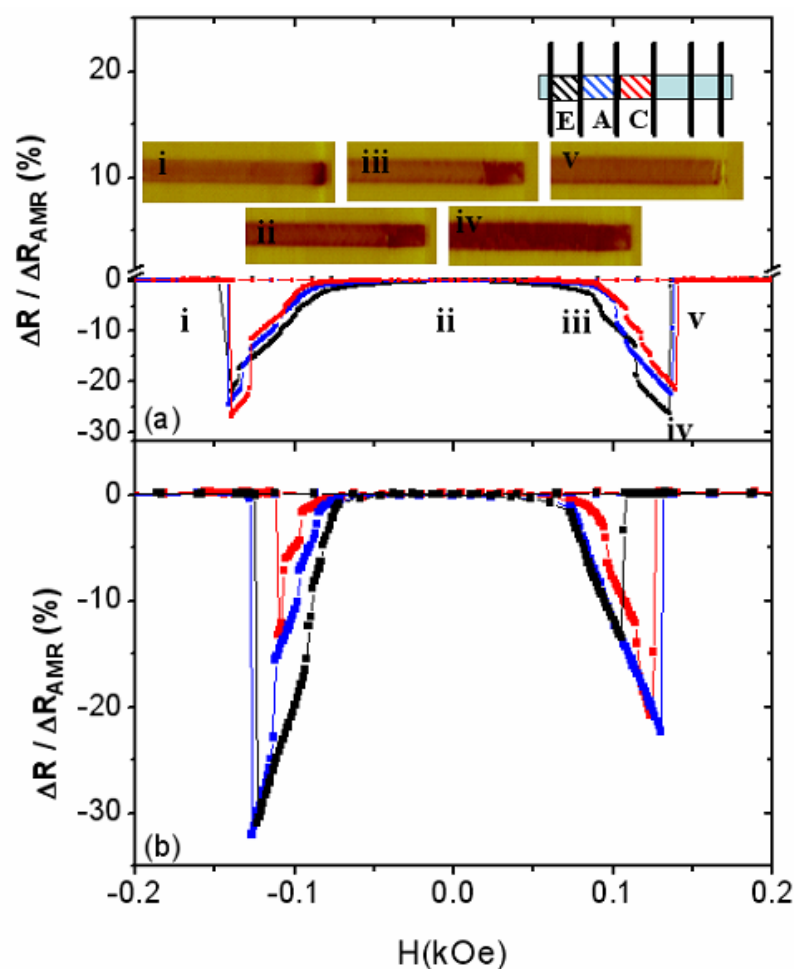


Figure 4-13: The LMR curves of wires with $w=1.2$ (a) and $1.5\mu\text{m}$ (b), respectively. Red, blue, and black symbols are for the center, arm, and near-end parts of the wire, respectively. A series of MFM images of one half of the $1.2\mu\text{m}$ wide wire in some corresponding fields indicated by letters.

For a wire with width less than $1.2\mu\text{m}$, the magnetization reversal is strikingly different from the above picture. We show a series of MFM images of about one half of $0.7\mu\text{m}$ wide wire and the LMR at different segments of the wire of the same geometries in Fig. 4-14(a). Three curves for different parts of the wire are shifted for clarity. All demonstrate the typical hysteresis behaviors of single domain wire. Meanwhile, it is quite striking that magnetoresistance magnitude of the near-end part is more than an order larger ($\sim -14\%$) than other two regions ($-0.4 \sim -0.6\%$) at H_{sw} . The MFM images of one half of this wire in characteristic fields are shown in the

inset of Fig. 4-14(a). The end domain is almost one fifth of the wire, just covering the whole near-end part. Overall, the magnetization reversal is similar to the $1.2\mu\text{m}$ wide sample. Moreover, the growth of the end domain region is limited resulting in the dramatically different resistance changes in different parts of the wire. Wires with $0.6\leq w<1.2\mu\text{m}$, the magnetic reversal behavior is similar. LMR of the $1\mu\text{m}$ wide wire is also shown in Fig. 4-14(b). The main feature is analogous to the $0.7\mu\text{m}$ wide wire.

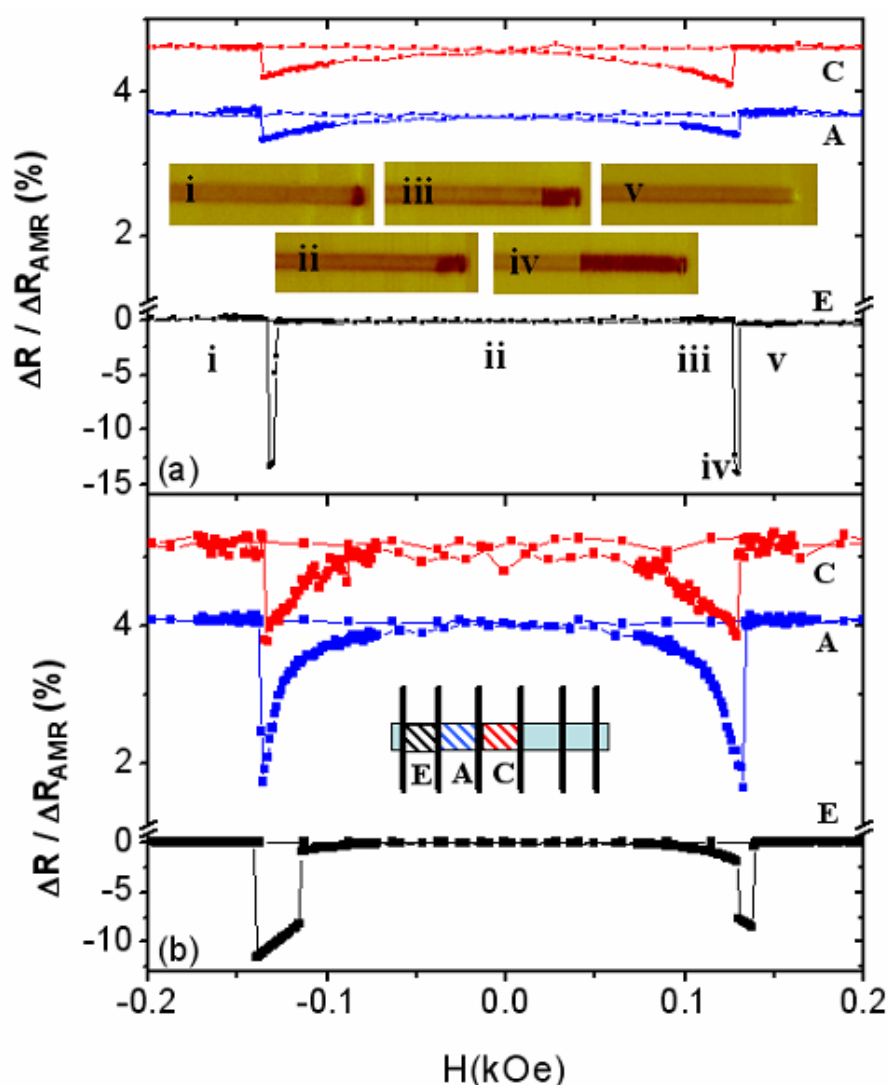


Figure 4-14: The LMR curves of wires with $w=0.7$ (a) and $1\mu\text{m}$ (b), respectively. Red, blue, and black symbols are for the center, arm, and near-end parts of the wire, respectively. A series of MFM images of one half of the $1.2\mu\text{m}$ wide wire in some corresponding fields indicated by letters. Curves are shifted vertically for clarity.

Until now, this spatial dependent MR behavior has not been reported yet. In previously related experiments [6,7,11,22], many series of wires with various geometries and materials have been fabricated to investigate the reversal process. However, most of these experiments focus on the whole volume wire behavior and the relation between switching field and wire geometries. Therefore, this spatial dependent behavior can not be resolved. As far as we know, only one spatial dependent behavior has been recently reported by Endo *et. al.* using the magnetic field sweeping magnetic force microscopy [27]. They applied the magnetic field along the wire axis and observed the magnetic phase change simultaneously at different parts of a series of 10nm thick and $2.1\mu\text{m}$ long Py wire. There is a clear square hysteresis as the moment phase measurement is performed at wire ends and a small v-shaped hysteresis loop as the moment phase measurement is performed elsewhere. Since the magnetic tip is sensitive to moment, data just indicates that there are stray fields (vortex core) at both ends. In fact, there is no detail of micromagnetic configuration. They arbitrarily claimed that this spatial dependent behavior for Py wires with $2.1 \leq m \leq 21$ is the evidence for the nucleation, movement, and annihilation of the vortex core during the reversal. According to Aharoni model, sample with $m=2.1$ and $L=2.1\mu\text{m}$ is in multi-domain state and the reversal process would be strictly different.

We have shown that there is a spatial dependence of MR for the $0.7\mu\text{m}$ wire corresponding to the limited expansion of the end domain before switching. As for the wire of $1.2 \leq w < 2\mu\text{m}$, the end domain extends to the whole volume, resulting in the similar MR behaviors at different parts of a wire. We have used a low moment tip for in-field MFM imaging in some wires of proper width to examine the detailed magnetic configuration during the magnetization reversal in this region. For magnification, the image of only one quarter of the wire is displayed. A series of

in-field MFM images of 1.3 μm wide wire is presented in Fig. 4-15 to provide an insight into the process during the magnetization reversal. For this kind of wire, the dark region of the end domain expands through the whole volume for an interval of magnetic field, as point (iii) ~ point (iv) in Fig. 4-13. Fig. 4-15(b) is similar to Fig. 4-13(iii), right before the sudden expansion of the dark region. Fig. 4-15(c)(d)(e) are three main features of magnetic configuration in the whole wire before switching. With a slight increase of magnetic field, end domain expands over the whole wire and some bright lines appear along the edge, as shown in (c), implying that domain walls form along the edge. With further increasing the magnetic field, bright lines become longer and reach the central line of the wire, as shown in (d). Right before switching, a 180° cross-tie like wall forms with 180° wall line close to the central line as shown in (e). The formation of these remarkable domain walls efficiently reduces the free surface magnetic charges resulting in a low demagnetization energy. In an elliptic and a point-end Py element, the similar cross-tie edge wall has been observed during the reversal [29,32]. However, the shape induced the metastable state should be different from ours. Moreover, the MR behavior is step-like and remanent magnetic state is not single domain regarding the low aspect ratio.

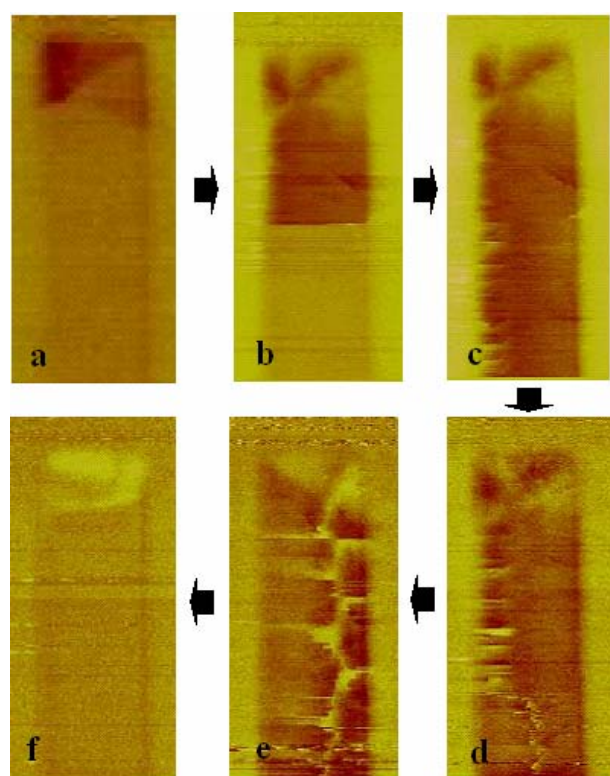


Figure 4-15: A series of MFM images of a $1.3\mu\text{m}$ wide Py wire which has $H_{sw} \sim 30$ Oe at room temperature. Magnetic field (a) 0, (b) 23, (c) 25, (d) 27, (e) 29, (f) 32 Oe.

For a series of Py wires, the above reversal process is obviously found in wires with $1.2 \leq w < 2\mu\text{m}$. As for a narrow wire ($0.6 \leq w < 1.2\mu\text{m}$), the growth of the end domain is still observed during the reversal. However, the expansion of the end domain (ΔL) does not occupy the whole volume of the wire, only by 12-25%. When the wire width is smaller than $0.6\mu\text{m}$, the end domain is reduced to 3-5% and does not reach the near-end region. Therefore, MR is indistinguishable among three segments. The insets in Fig. 4-16(a) demonstrate two sets of MFM images taken at remanence and at the field near H_{sw} for wires with $w = 1.3, 0.7,$ and $0.3\mu\text{m}$ from top to bottom, respectively. Before acquiring images, a magnetic field of 800 Oe was applied along the wire axis to saturate magnetization. Then, MFM images were taken at remanence and at the field just before switching, very close to H_{sw} within 5 Oe. Numerous scanning at different

tracks with low moment tips were performed to make sure that there is no domain distortion and domain wall drag by the stray field induced from magnetic tips. The remanent domain structures are like what has been discussed in section 4-1-2. For a $0.3\mu\text{m}$ wide wire, there is no observable domain wall but only the magnetic contrasts at ends of the wire. As for wires with $w = 1.3$ and $0.7\mu\text{m}$, the flux closure structure was clearly observed and occupies the entire volume of a wire by 8 and 5%, respectively. In Fig. 4-16(a) the length occupation ratio ($\Delta L/L$) of the remanent end domain represented by the black square symbols gradually increases as w is enlarging and saturates as $w > 1\mu\text{m}$. While near H_{sw} , the end domain grows and the length occupation ratio is sensitive to the wire width. For instance, the ratio is about 22% for a $0.7\mu\text{m}$ wire but the end domain punches through the entire volume for a $1.3\mu\text{m}$ wire with ratio of 50%. We find that the evolution of the domain expansion is closely related to the variation of K_u , which is presented in Fig. 4-16(b). The domain expansion is suppressed effectively by the rapid increase of K_u as a wire width is less than $0.6\mu\text{m}$. As the sample width is larger than $0.6\mu\text{m}$ but is smaller than $1\mu\text{m}$, the anisotropy energy keeps the most part of magnetic moment in the single domain state at remanence, but cannot compete with other energy terms as approaching H_{sw} , resulting in the enlargement of the non-uniform domain structure from the end. For more wide wire, the anisotropy energy is rather weak, resulting in the collapse of the particular end domain structure and the distribution of cross-tie like wall over the whole volume. The transverse anisotropy influenced by the dimensions and the shape of the wire dominates the domain expansion which originates from the nucleation of vortex domain at the wire ends.

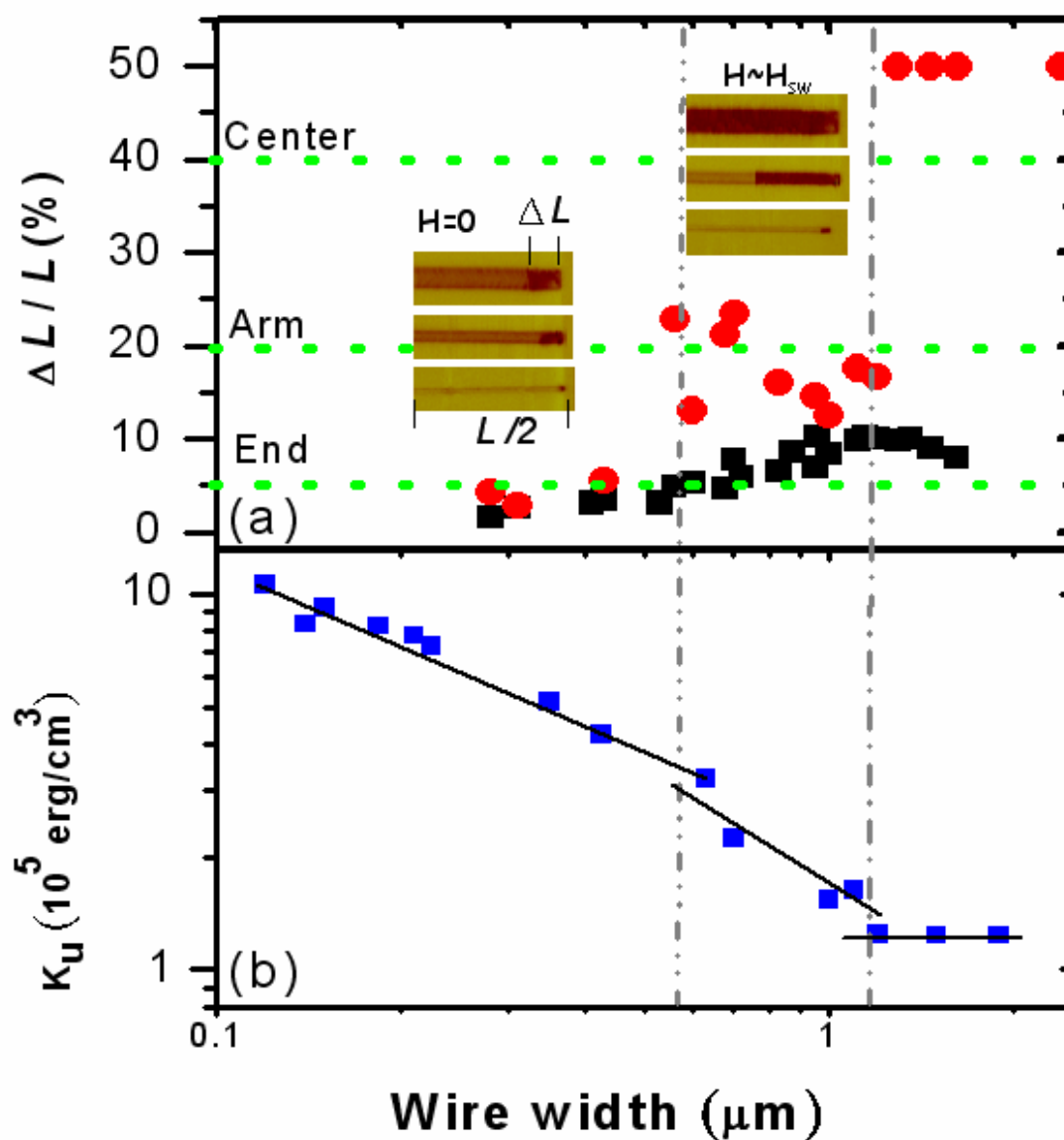


Figure 4-16: (a) The semi-log plot of the length occupation ratio of the end domain versus wire width. The red circles and the black squares indicate the applied field is at remanence and near H_{sw} , respectively. The insets are two sets of MFM images taken at remanence and near H_{sw} for wires with $w = 1.3, 0.7$, and $0.3 \mu\text{m}$ (from top to bottom). (b) The log-log plot of the uniaxial anisotropic constant as a function of wire width. The solid lines are guides to the eye.

As mentioned previously, the expansion of the end domain is attributed to the transverse anisotropy. It plays an important role not only in the determination of the

remanent magnetic structure, but also in the rearrangement of the end domain during the reversal. When wire width is close to thickness, the competition between the transverse and polar anisotropies leads to that magnetic moments are imbedded in the body without the exposure of the stray field during the reversal.

The reversal of an elongated particle is possibly completed via several mechanisms. The SW model predicts that the $H_{sw}(\theta)$ curve is a U-shape and has its nadir at $\theta=45^\circ$ when the reversal occurs via coherent rotation. While when the reversal occurs via magnetization curling or the propagation of domain walls, H_{sw} increases with increasing θ . The curling mode reversal with the analytical model for a prolate spheroid is developed by Aharoni. A relationship of $1/\cos\theta$ for H_{sw} is expected in terms of the propagation of domain wall. The details of these modes have been discussed in section 2-2-2.

The relationship of H_{sw} with θ was obtained using the angular dependence of MR measurement. We compare the obtained H_{sw} with the Aharoni model. Fig. 4-17 shows eight $H_{sw}(\theta)$ curves for Py wires with various widths from 0.14 to $1.9\mu\text{m}$. Except for the $1.9\mu\text{m}$ wide Py wire, each curve demonstrates a concave upward tendency. For all data, H_{sw} has a minimum value at $\theta=0^\circ$ and increases continuously with increasing angle, implying the reversal is not completed via coherent rotation. In addition, fit of $H_{sw}(\theta)$ to the analytical curling reversal model was performed. For a prolate spheroid, the $H_{sw}(\theta)$ is given by

$$H_{sw}(\theta) = 2\pi M_s \frac{(2D_L - \frac{k}{S^2})(2D_r - \frac{k}{S^2})}{\sqrt{(2D_L - \frac{k}{S^2})^2 \sin^2 \theta + (2D_r - \frac{k}{S^2})^2 \cos^2 \theta}} \quad (4-4)$$

where D_L and D_r are the demagnetizing factors of the spheroid along the major and minor axes, respectively. The parameters D_L , D_r , and k are determined by the sample's

dimensions. The parameter S is the reduced radius $2r/\ell_{\text{ex}}$. The only adjustable parameter is the semi-axis r in the fit. The fit is presented as the dashed line in Fig. 4-17 and the value of parameter r is listed in Table 2. It is unforeseeable that the theoretical line describes very well for samples of width $0.35 \leq w < 0.63 \mu\text{m}$. There are some departures at large θ for the wider wires. The deviation is pronounced for the narrower wire. The deviation is frequently attributed to the nucleation sites or the pinning sites created by the edge roughness and structure defects resulting in the local reversal process [6,33,34]. The inference of the local reversal process could be also supported by the fact that the values of r are found to be consistently smaller than the effective radius $r_{\text{eff}} = \sqrt{wt}/2$. The nucleation volume is about 30 ~ 35% of the volume of the wire using the value of r from the fit. Early studies on $H_{\text{sw}}(\theta)$ of Ni cylinders with diameter 80nm concluded that the irreversible reversal nucleates in a volume much smaller than the whole volume of the wire ~ 30% [6,22]. On the other hand, Wernsdorfer *et. al.* measured the switching time of Ni cylinders using micro-SQUID and concluded that the “activation volume” of their wire is two orders of magnitude smaller than the whole wire volume [12]. However, measurements of this are difficult and rare.

In addition, the relationship of $1/\cos\theta$ is also used to make the comparison with the $H_{\text{sw}}(\theta)$ curve and is plotted as the solid line in Fig. 4-17. We find that the solid line is very similar to the dashed line expected by curling reversal model, and can not provide a well description to the experimental data neither. According to the discussion of $H_{\text{sw}}(\theta)$ curves, we suggest that the reversal is completed via the local reversal process together with the propagation of the domain wall.

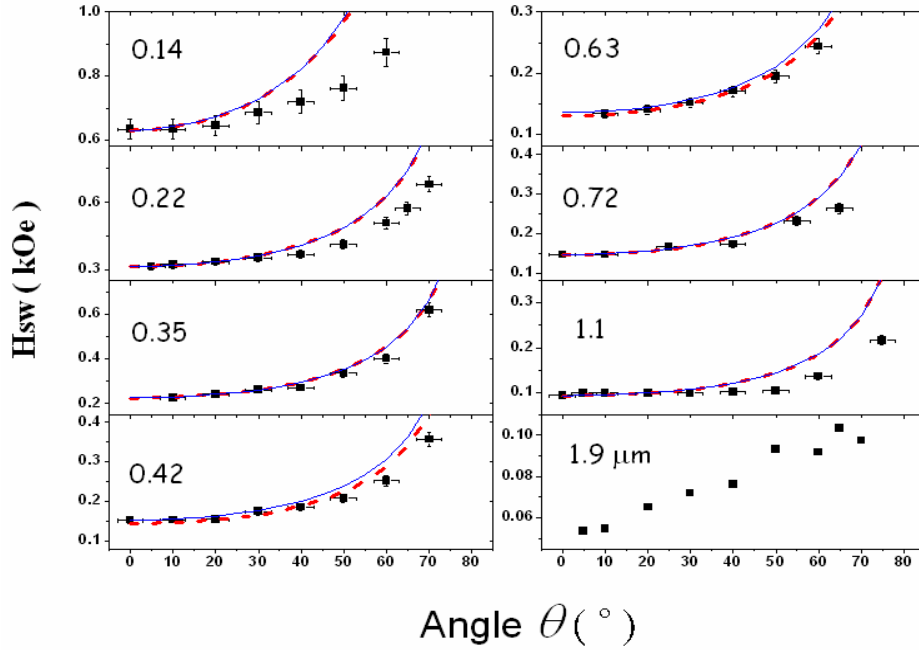


Figure 4-17: The switching field as a function of θ for eight wires with widths $w=0.14, 0.22, 0.35, 0.42, 0.63, 0.72, 1.1,$ and $1.9\mu\text{m}$. The dashed lines are the theoretical predictions according to the magnetization curling. The solid lines demonstrate the relationship of $1/\cos\theta$ for H_{sw} .

Wire width w (μm)	0.14	0.22	0.35	0.42	0.63	0.72	1.1
Aspect ratio m	143	91	57	47	32	28	18
Effective radius r_{eff} (nm)	32	41	51	56	69	73	91
r_{fit} (nm)	18	26	30	38	40	38	47

Table 2. Parameters of numerous samples. r_{fit} is only the adjustable parameter obtained in the best fit of Eq. (4-4) to data.

For magnetic fields applied along the long axis ($\theta=0^\circ$), Eq. (4-4) is reduced to $H_{sw}^{\theta=0} = 2\pi M_s \left(\frac{k}{S^2}\right)$ and $H_{sw}^{\theta=0}$ is expected to increase with $1/r^2$ for a prolate spheroid.

The log-log plot of $H_{sw}^{\theta=0}$ obtained from the LMR ($\theta=0^\circ$) versus the sample's width is shown in Fig. 4-18. The rightmost three data points for multi-domain wires should not be included here. Since the reversal mechanism is completely different from others.

The data of these three wide wires should represent the coercive field instead of the switching field. Here we just show that the values are less 100Oe, quite reasonable for multi-domain Py wires. Despite these three points, $H_{sw}^{\theta=0}$ seems barely change for wire of $0.7 < w < 2\mu\text{m}$ and increases rapidly with decreasing wire width for narrower wires. The linear fit to data points of $w < 0.7\mu\text{m}$ gives a slope of -0.98 ± 0.09 indicating that $H_{sw}^{\theta=0}$ is proportional to $1/w$ [34,35]. Since our samples are orthorhombic with a constant thickness, the effective radius r is $\sqrt{wt}/2$ and hence, our experimental result that $H_{sw}^{\theta=0} \propto w^{-1}$ is in consistence with the theoretical prediction. The scenario confirms that the reversal is caused by the magnetization curling. On the other hand, $H_{sw}^{\theta=0} \sim 0.15\text{kOe}$ and seems to be independent of wire widths with $0.7 < w < 2\mu\text{m}$, implying that there is a different reversal mechanism. The result coincides with the spatial dependence behavior.

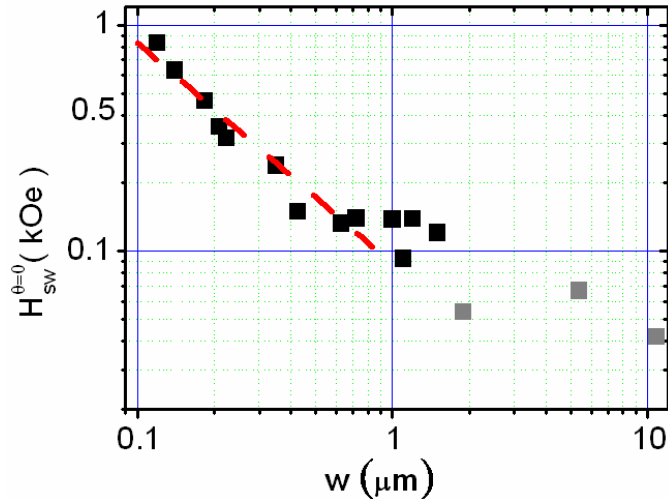


Figure 4-18: The log-log plot of the switching field obtained from the longitudinal MR ($\theta=0^\circ$) versus the permalloy wire's width. The dashed line is the linear fit to the data. The rightmost three points represent the coercive field for the multi-domain configuration.

Many of the earlier experiments in elongated samples fabricated by

electrochemical deposition focused on the study of $H_{sw}(\theta)$ [6,12,15,20,21]. This deposition method enabled the production of extended cylinders with a diameter of less than 100nm in close to a infinitely long cylinder. Wegrowe *et al.* performed the MR measurement in Ni and Co nanowires of about 60nm in diameter and $6\mu\text{m}$ in length to obtain the relationship of H_{sw} with the in-plane field angle [6]. Although their data can be well fitted by the equation derived for the magnetization curling mode, they found that the fitting parameter dose not reflect to the value account for the curling of the whole volume. According to their fitting parameter, the nucleation volume is estimated only about 30% of whole volume. They suggested that the magnetization reversal in Ni wires is completed via the local curling. Comparing with our result, we also find the nucleation volume ranges in 30 ~ 35% of the volume of the wire. However, the deviation of our data from the theoretical expectation at the large angle is different from their case. Their data is larger than the theoretical expectation. In our series of Py planar wires, the deviation is pronounced for the narrower wire. The reason may be the theoretical model used to interpret our data which is based on the nucleation theory developed for ellipsoidal geometries. Recently, Oliveira *et al.* developed the $H_{sw}(\theta)$ relation based on the magnetization buckling mode for planar wires [11]. They found that their data for two Py wires with $w=0.46\mu\text{m}$, $l=10\mu\text{m}$, $t=3.5\text{nm}$ and $w=0.29\mu\text{m}$, $l=6\mu\text{m}$, $t=12\text{nm}$, respectively, can be well described by their model. The fitting parameter, demagnetizing factor along the wire width, is very small in both cases, because the thickness of wires is smaller than wire's width by more than one order of magnitude. In addition, the narrower wire has the larger demagnetizing factor as expected from the behavior of the demagnetizing field. However, their model predicts that the $H_{sw}^{\theta=0}$ only depends on the wire length. The prediction seems to be in conflict with our and other previous results [34,35].

4-3 Domain wall resistance in the centipede-like structures

In general cases, the contribution of DW scattering to the MR is so small that it is easily concealed by conventional sources of low temperature MR such as anisotropic magnetoresistance (AMR) and Lorentz MR in a ferromagnetic system. In order to enhance the domain wall resistance (DWR), the formation of the dense stripe domain is a usual method. When a material has a high uniaxial anisotropy normal to the film plane, well-defined stripe domains appear with a large number of Bloch walls, leading to unambiguously overcome the AMR signals. The selection of such material is the epitaxial hcp Co [36], SrRuO₃ [37] at early experiments and is the FePd [38], CoPt [39] with the L1₀ crystallographic structure. In order to provide well-defined transport measurement geometries and control the placement of domain walls, a large number of experiments for domain wall effects put effort in lithographic devices. Many unique patterns, such as adding a neck to the wires [40], designing zigzag structures [41], and forming a stripe domain by thickness modulation [42] or exchange biases [43], were used to create the artificial domain walls. Therefore, the DWR of individual domain wall is obtained. In addition, the domain wall thickness can be controlled experimentally by the use of hard-soft multilayer exchange spring system [44,45]. In such a system, the domain wall thickness can be changed by varying the applied magnetic field and the dependence of DWR on the domain wall thickness can be revealed.

Many of the earlier experiments in patterned magnetic structures measured a reduction in the resistance when the sample entered a multi-domain state. A negative DWMR was measured in zigzag-shaped Co wires by Taniyama *et al.* [41]. In this geometry it is possible to generate two different forms of 90 degree walls at the zigzag

corners. When demagnetized along the length of the zigzag the magnetization will flow along the wire, however, when demagnetized across the wire a head-to-head or tail-to-tail domain wall will occupy each corner. In this way, it is possible to remove the AMR effect by comparing these two states, resulting in that a negative DWMR was found at helium temperatures. This negative result persisted up to about 200K, meaning that it is difficult to explain via the phase breaking model, destroying weak localization correlations [46]. Later experiments on permalloy zigzag [47,48] seemed to only show AMR effects. The properties of (110) epitaxial Fe films patterned into wires with the (001) easy axis lying across the wire stripe were examined by Parkin *et al.* [49]. This leads to stripe domains lying across the wire. In order to eliminate the AMR effect, the anisotropy of the Lorentz MR becomes more pronounced as the temperature is lowered and is of opposite sign to the AMR, leading to one effect just balances the other at a compensation temperature $\sim 65\text{K}$. At this temperature, the presence of domain walls reduced the resistance of the wire was found. Although domain walls have been predicted to reduce the resistance through phase breaking model, this should not take place much above helium temperatures.

Xu *et al.* fabricated some microscale permalloy crosses [50]. The magnetization at the junction was shown by MFM and micromagnetic simulation. Longitudinal MR showed a contribution only about one third of what would be anticipated for the AMR based on a finite element model. Here the AMR reduces the resistance of the sample, so that a contribution of the domain walls which increase resistance could account for the discrepancy. The magnitude of the effect, around 0.01%, was confirmed in a similar experiment by Yu *et al.*, using partially disconnected cross structures [51]. However, a cross-shaped junction in another similar experiment showed only AMR [52].

Danneau *et al.* fabricated an epitaxial $L1_0$ FePd L-shaped wire to detect and count individual domain walls [53]. In this device, the direction of the probing current could be parallel and perpendicular to the stripe domains created during sample growth. Various voltage probes were formed as part of the patterned device. Discrete jumps in the resistance were observed during the application of magnetic field as the domain walls move. Additional resistance was generated by a single wall at low temperatures corresponding to an extra interface resistance in the current perpendicular to the domain wall (CPW) geometry, corresponding to an MR within the wall of about 10%. This experiment clearly demonstrates the positive domain wall MR in this material, and the difference in the current in the domain wall (CIW) and CPW geometries.

Although the DWR was observed in various systems, both positive and negative values were reported with their theoretical justifications [46,54,55]. We summarize the previous results in Table 3. Up to now, the sign and the magnitude of the DWR and the fundamental mechanism of DW scattering are still controversial. Most investigations to this subject focus on either 90° or 180° DW structures, regardless of the Néel or Bloch wall. In our work, the centipede-like Py structures were fabricated to obtain a series of Néel wall with various relative angles between two domains. The angular dependence of Néel wall resistance is explored by analyzing the longitudinal and transverse MRs based on a simple resistance-in-series model.

In this section, we first present the magnetoresistance of the centipede-like structures. The magnetization reversal in this structure will be explained by MR measurement combined with MFM images. Then, we clarify how the relative angle between two domains is obtained. Finally, a simple resistance-in-series model was developed to reveal the relationship of DWR with the relative angle.

Temp (K)	DWMR(%)	Samples
RT	+1.82	Ni constricted wires [40]
RT	+0.03	Ni films [55]
RT	+1.7	NiFe constricted wires [40]
RT	+0.34	NiFe zigzag wires [47]
RT	+0.3	NiFe crosses [50]
RT	-0.14	NiFe wires [56]
RT	AMR	NiFe rings [57]
RT	AMR	NiFe wires [58]
77	+0.23	NiFe/Gd structures [45]
77	+0.2	Co wires [59]
5	-0.05	Co zigzag wires [41]
85	+0.5	Co films with hcp structures [60]
RT	+0.14	Co films with thickness modulation [42]
5	+0.05	Co films with exchange bias [43]
RT	+1.8	(CoPt) ₇ wires [39]
65	-0.1	Fe wires [49]

Table 3. Summary of other DWMR studies.

4-3-1 Magnetoresistance

The centipede-like Py structures in submicron scale were made using standard e-beam lithography, thermal evaporation, and lift-off techniques. As shown in Fig. 4-19, each structure consists of a central wire and several finger wires that bisect orthogonally the central wire. All wires have a thickness of 30nm. The central wire is $60\mu\text{m}$ long and $1\mu\text{m}$ wide (W). All finger wires are $20\mu\text{m}$ long but have various widths (w : 0.3, 0.4, 0.5, 0.8, 1, and $1.5\mu\text{m}$). For a constant finger width, we made several series of structures with either different pitch l between the neighboring fingers ($1w \leq l \leq 10w$) or number of fingers n systematically. Fig. 4-19 is a SEM picture of one typical sample with $w=l=0.5\mu\text{m}$. Brighter stripes are the nonmagnetic Au contacts serving as the voltage leads for MR measurements.

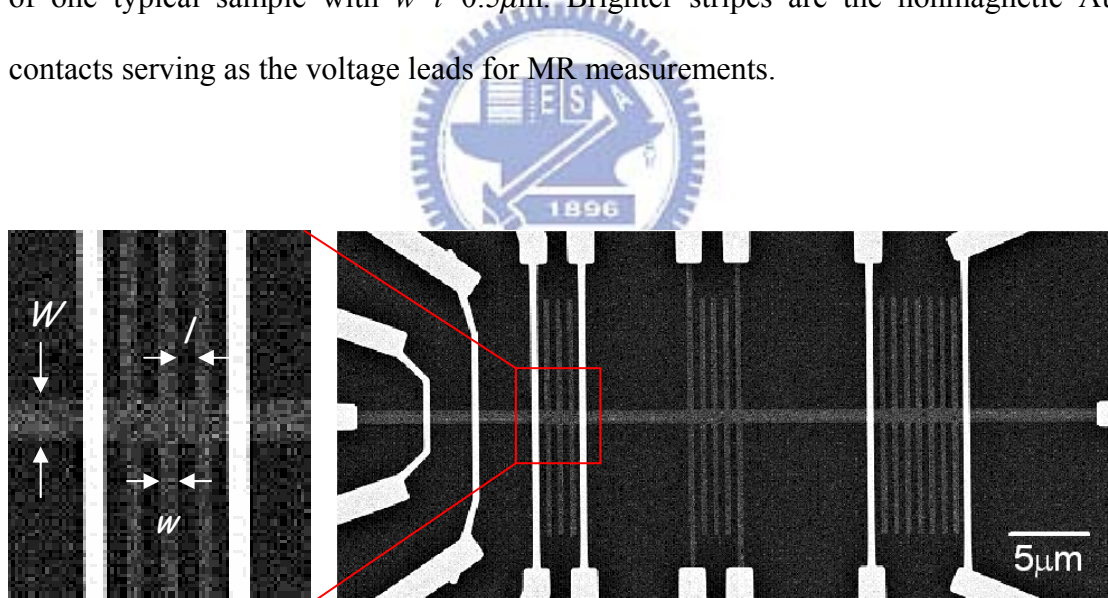


Figure 4-19: Right: A SEM image of one typical sample. The gray pattern is Py and the brighter wires are Au. The central wire of Py is $60\mu\text{m}$ long and $W=1\mu\text{m}$ wide. Two structures of 3 and 7 finger wires are arranged with $w=l=0.5\mu\text{m}$. The other structure at the center is arranged for the Planar Hall effect measurement. Left: An enlargement of the structure with $n=3$.

As discussed in the previous sections, the magnetic configuration in the polycrystalline magnetic wire is dominated by the aspect ratio as a result of shape anisotropy. The uni-axial anisotropy constant (K_u) can be quantified by the fit of TMR to the Stoner–Wohlfarth model. For a $20\mu\text{m}$ long Py wire with width from 0.1 to $2\mu\text{m}$, the remanent magnetic configuration is a single domain and K_u decreases from 10.5 to $1.3 \times 10^5 \text{erg/cm}^3$, respectively. These values are much larger than the magnetocrystalline anisotropic energy density by two orders of magnitude. In our centipede-like structures, the moment of the central wire preferably lies parallel with the axis of the central wire while those of the finger wires preferably lie perpendicularly.

LMR and TMR of one structure with three fingers are plotted in Fig. 4-20(a). The LMR is saturated at 1kOe and slightly decreases as the magnetic field approaches zero due to the coherent rotation of finger wires. When the field sweeps to the opposite direction and about 30Oe , the reversal is completed via a single jump, which is the switching characteristic of the central wire. The TMR has the lowest resistance at saturated field of 1kOe . When the field is reduced to zero, the magnetization of the pitch coherently rotates to the axis of the central wire, while the magnetization of the fingers remains. When the field sweeps to the opposite direction in the range between 110Oe and 130Oe , the MR curve exhibits clearly 3 successive plateaus, a staircase. Fig. 4-20(b) is the magnification of TMR shown in Fig. 4-20(a). The number of steps is the same as the number of fingers. This is confirmed by a systematic investigation in structures which have the same geometries of both wires but different number of fingers ($3 \leq n \leq 40$). The abrupt resistance drop is ascribed to the switching of each finger wire. After the step sequence, all magnetizations almost lie along the field direction and the resistance smoothly back to the saturation value. To further

investigate the TMR curve, a series of MFM images were taken in magnetic fields, as shown in the inset of Fig. 4-20(a). The magnetic field was applied along the axis of the finger wires. At the field of -520Oe , the magnetization of the finger and the central wires are all aligned with the external field, (i). At the zero field, the finger and the central wires have the characteristics of the single domain but there is a regular contrast at each junction, (ii), suggesting an artificial domain pattern was created by delicate arranging the anisotropy. When the magnetic field is applied to the opposite direction and exceeded the switching field of finger wires, the change of magnetic contrast at the ends of the finger wires was observed, (iii) and (iv), implying the switching of the finger wires. The magnetization reversal of the finger wires is completed at $+130\text{Oe}$, (v), and fully saturates again at $+520\text{Oe}$ (vi). Note that the bright areas in the central wire next to 1st and 3rd finger wires are nonmagnetic contact leads ($t \sim 100\text{nm}$).

It is important to note that the resistance at remanence is a constant despite of different field scanning processes. As shown in Fig. 4-20(a), both LMR and TMR have the same value at $H=0$. We believe that there is a very stable remanent magnetic configuration that the moment of the pitch is along the axis of the central wire and the moment of the finger is perpendicular to the axis of the central wire. As to the junction, there are orthogonal moments at its four corners resulting in a tilted moment of the junction.

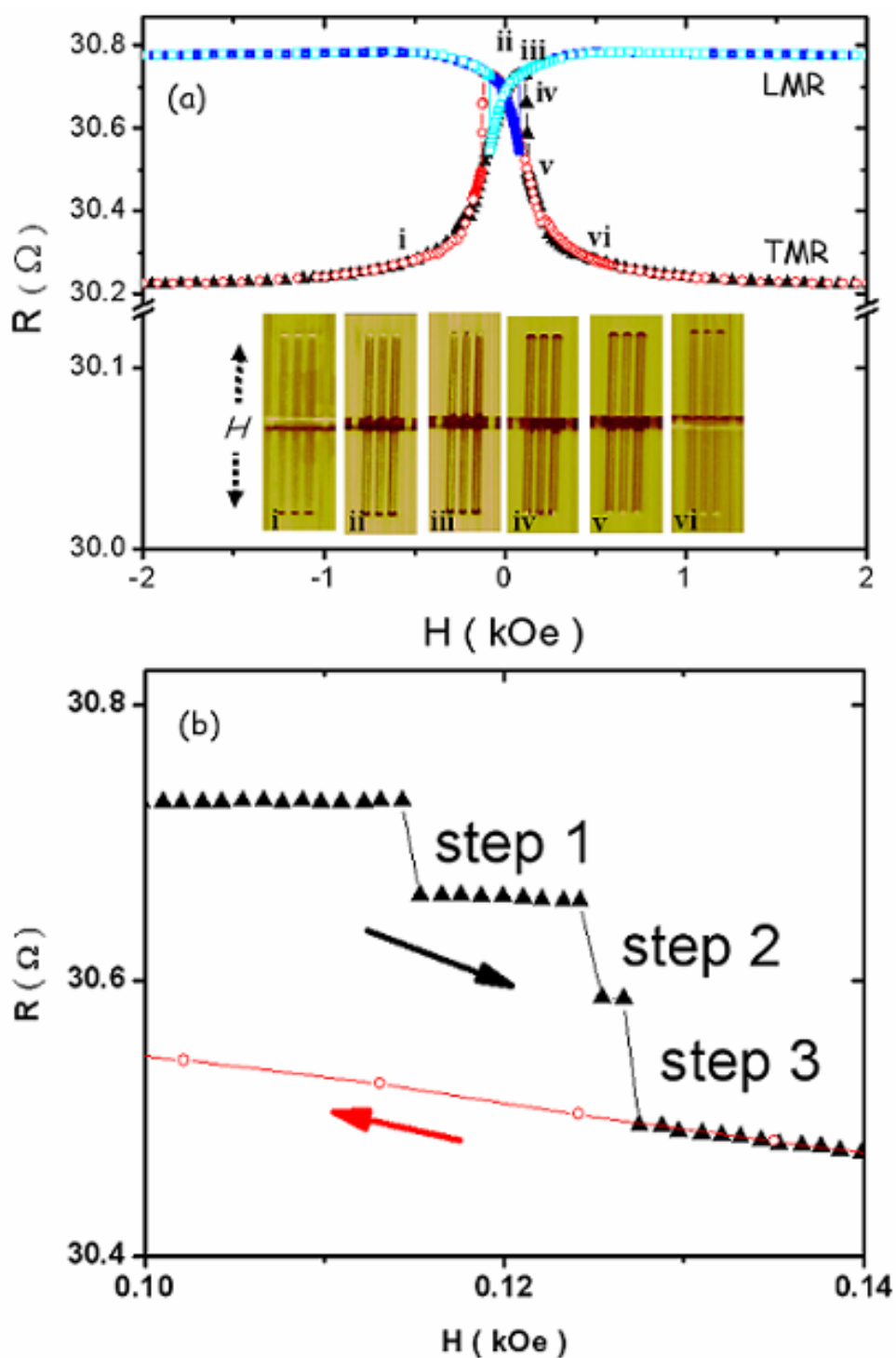


Figure 4-20: (a) LMR and TMR of one sample with $w=l=0.5\mu\text{m}$ and $n=3$. The inset is a series of MFM images labeled by (i)-(vi), describing magnetic configuration at the characteristic points on the hysteresis loop. (b) An enlargement of the TMR at low field.

4-3-2 Planar Hall effect

In order to obtain the tilted angle of the moments at the junction, the transverse voltage V_{xy} across the junction via the orthogonal fingers in the presence of the in-plane magnetic field was measured. The measurement is the so-called planar Hall effect (PHE) which arises from the anisotropy of spin-orbital scattering in magnetic materials, as explained in section 2-3-1. V_{xy} is sensitive to the angle θ between the current density J and magnetization M . Here, the magnetic field is applied along the axis of fingers (the y-axis). Fig. 4-21(a) presents the TMR and the PHE curves for a sample with $n=4$. There are clear four steps in the TMR curve corresponding to the number of fingers. Both TMR and LMR follow our previous statement. The abrupt drops in V_{xy} of fingers 1 and 2 correspond to the dramatic rotations of moments at the junctions 1 and 2 in the coercive fields, 77 and 101Oe, respectively. Both fields of the drops are the same as the first and last steps in the TMR of one centipede-like structure that consists of both fingers indicating the sequentially one-by-one moment switching of fingers. Furthermore, the $\sin 2\theta$ dependence of V_{xy} allows us to estimate the tilted angle of moment at the junction for a series of fingers with various widths. The values obtained from PHE are very close to $\tan^{-1}(K_u^{finger} / K_u^{central})$ within an uncertainty of 3° . K_u^{finger} and $K_u^{central}$ are the anisotropy constants of the finger and central wires, respectively. Therefore, remanent moment direction at the junction is fairly determined by the shape anisotropies of the pair of orthogonal intersecting wires. Here, the tilted angles in this study range from 40° to 80° with decreasing the finger width. Fig. 4-21(b) is a remanent MFM image for one segment of a centipede-like structure. The deviation in contrast of magnetic moments at each junction shows a regular pattern as opposed to showing no contrast at other position in the wires. The

image can be roughly confirmed by a micromagnetic simulation using OOMMF [61] (also see Fig. 4-21(c)).

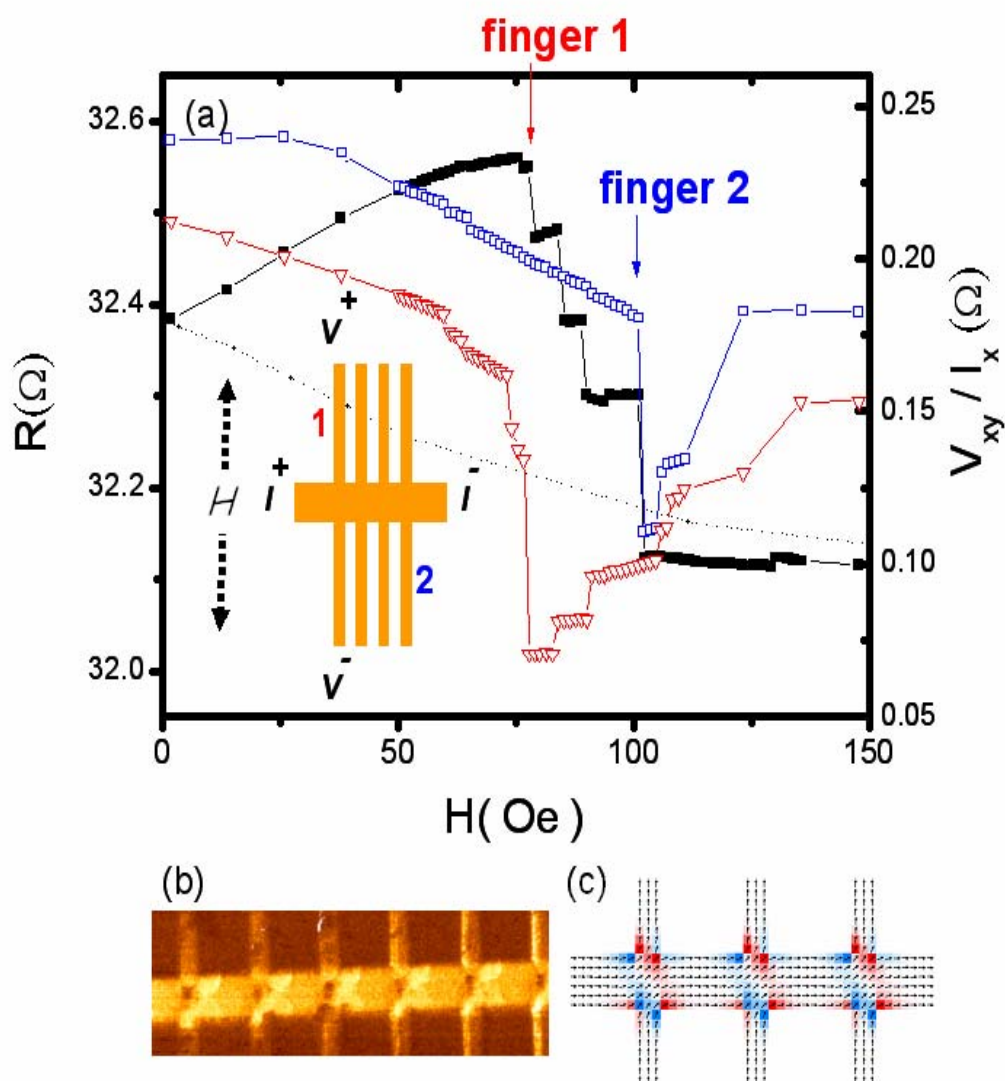


Figure 4-21: (a) TMR at low field for one sample with $w=l=0.8\mu\text{m}$ and $n=4$ (\blacksquare). Field dependence of transverse voltages V_{xy} divided by the current I_x for two fingers labeled as 1 (∇) and 2 (\square) in the scheme. (b) Remanent magnetic force microscopy (MFM) image of one sample with $w=0.5\mu\text{m}$ and $l=1.5\mu\text{m}$. (c) Micromagnetic simulation of the magnetization configuration of the similar sample with the reduced dimensions by a factor of 0.1.

4-3-3 Analysis of domain wall resistance

We have explained the reversal of our centipede-like structures in section 4-3-1. Although the distribution of moments during the field sweeping process is quite complicated, the magnetic configuration at remanence and saturation field can easily be figured out. The tilted angle of the remanent moments at the junction can also be found out by PHE.

For our centipede-like structures, a central wire orthogonally bisects n of individual finger wires as shown in the inset in Fig. 4-24. The whole structure can be divided to n junctions and $n+1$ central wire pitches. Each junction is connected to two central wire pitches. At remanence, the moment of the central wire lies preferably along the wire axis but the moment at the junction tilts due to finger wire. Hence, a Néel domain wall is present between the junction (\nearrow domain) and pitch (\rightarrow domain). Upon these situations, we develop a resistance-in-series model to analyze the DWR. In this model, the MR is composed of the resistances contributed from these three regions and is written as:

$$R(\vec{H}) = \frac{(n+1)l}{W} R_{pitch}(\vec{H}) + \frac{nW}{\alpha W} R_{junction}(\vec{H}) + 2n \left[R_{DW} - \frac{l_{DW}}{W} R_{pitch}(\vec{H}) + R_{DW}^{AMR} \right] \quad (4-5)$$

Here α is the current distribution factor which involves the influence of the non-uniform current density at the junction due to both open ends of a finger wire.

R_{pitch} and $R_{junction}$ are the sheet resistances of the pitch and junction, respectively. At the saturation field ($>1\text{kOe}$), all moments lie along the magnetic field and the domain wall is absent. Only the first two terms contribute the whole resistance with that $R_{pitch} = R_{junction}$. The last term is a correction under the consideration of DWs ($H < H_{sat}$). Linear dependences of saturated LMR and TMR on both l and n

give $R_{pitch}(\vec{H})$, $R_{junction}(\vec{H})$, and α . Fig. 4-22 shows a linear fit to all TMR data for one sample with $w=0.3\mu\text{m}$, $n=3$ and various l from 0.3 to $1.5\mu\text{m}$. $R_{pitch}^T = R_{junction}^T = 8.55\Omega$ and $\alpha=1.36$ were estimated from the values of the slope and the intercept. As for LMR, $R_{pitch}^L = R_{junction}^L = 8.66\Omega$ and $\alpha=1.36$ were obtained. The difference of the two sheet resistances is attributed to AMR effect. The current distribution is the same in two applied field orientation situations.

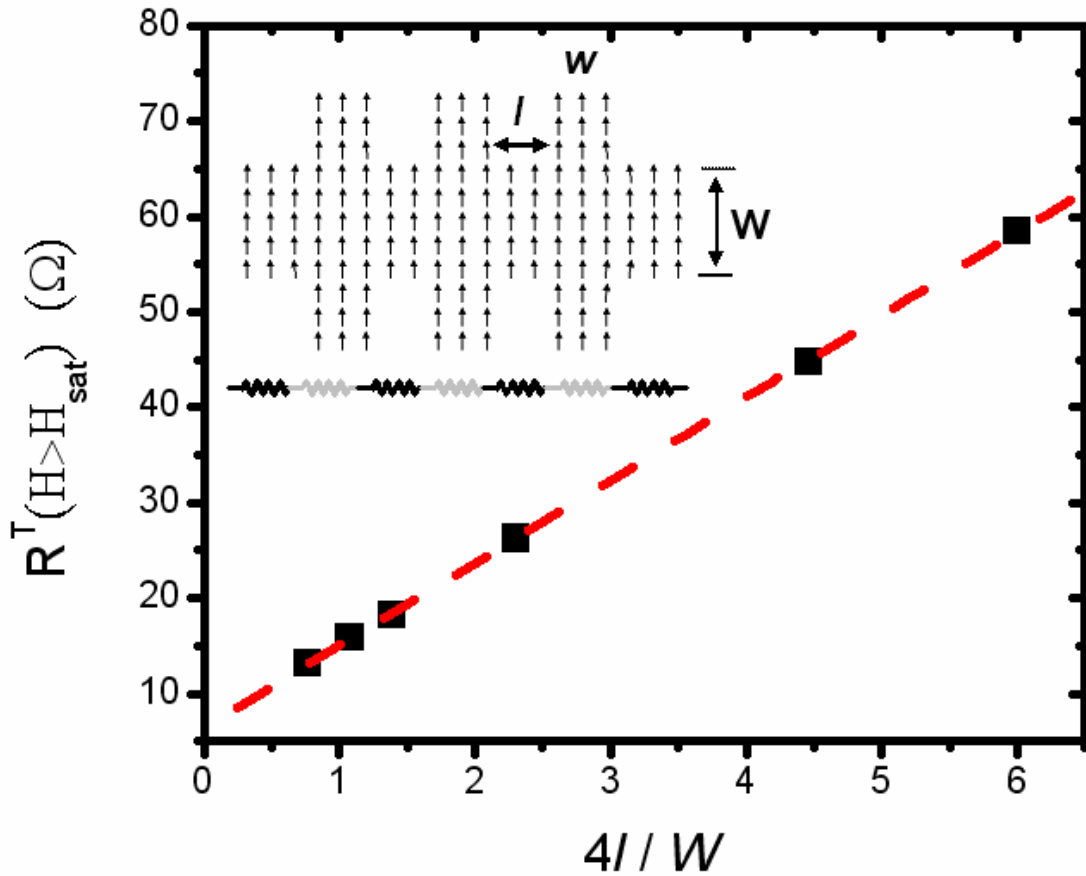


Figure 4-22: The saturated TMR resistance as a function of pitch widths l for the sample with $w=0.3\mu\text{m}$ and $n=3$. l ranges from 0.3 to $1.5\mu\text{m}$. The dashed line is the linear fit to data.

At remanence ($H=0$), the moments at the junction tile at an angle θ_{DW} while those at most area of pitch lie along the axis of the central wire. The domain wall of

length l_{DW} is created at both ends of each pitch. For the structure, there are $2n$ of domain wall and correspondingly, extra contribution of domain wall resistance, $2nR_{DW}$, is expected. Since moments of each domain wall rotate smoothly from angle θ_{DW} to zero relative to the axis of the central wire as shown in the inset of Fig. 4-24, original resistance of the region included in the 1st term of Eq. (4-5) should be deleted and additional AMR resistance should be taken into account. The domain wall width study in T-shaped Py structures by Haug *et al.* gives the rough estimate of l_{DW} [62], as seen in Fig. 4-23(a). He measured the domain wall width using photoemission electron microscope and x-ray magnetic dichroism. He found a decrease in domain wall width with decreasing contact dimension. Reducing contact dimension of T-shaped structure is similar to a decrease of finger widths in our centipede-like structure. The domain wall profile is assumed as a hyperbolic tangent function based on spin-polarized SEM studies in H shaped Py structures by Jubert *et al* [63], as seen in Fig. 4-23(b).

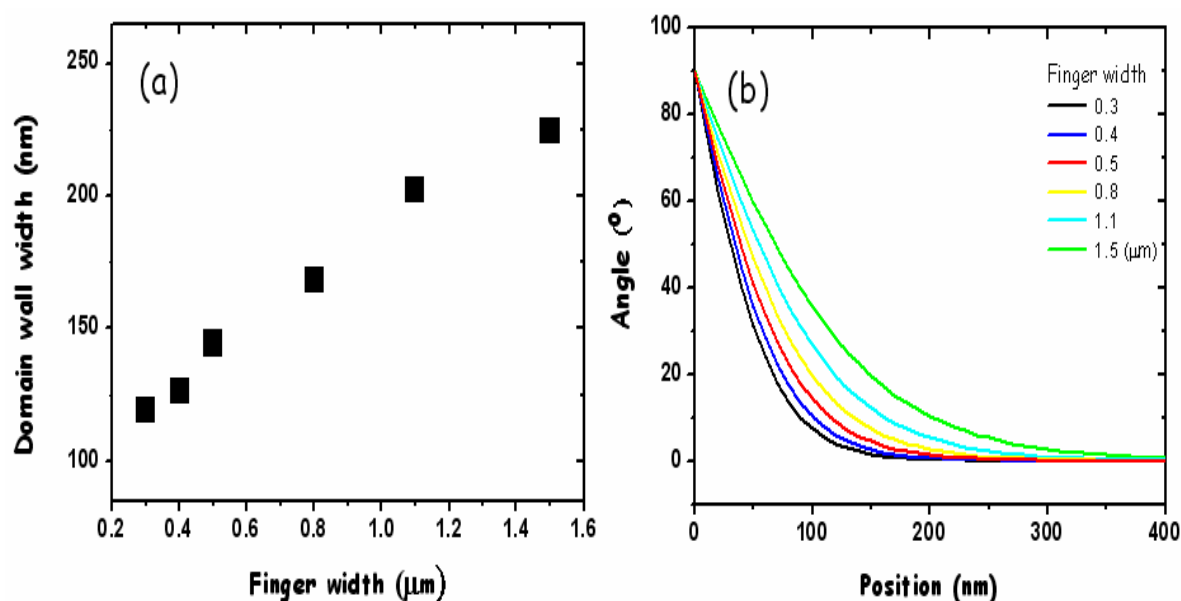


Figure 4-23: (a) The domain wall width as a function of the finger width estimated from the reference [62]. (b) A sketch of the domain wall profile by a hyperbolic tangent function.

Therefore, R_{DW}^{AMR} can be estimated for a given θ_{DW} . A systematic fit of remanent resistance to Eq. (4-5) give the self consistent quantities of R_{DW} . Fig. 4-24 demonstrates the angular dependence of R_{DW} . DWR is positive and increases with increasing θ_{DW} from 42° to 76° . One explanation for the positive DWR is the mistracking effect [55] that DWR results from the scattering between the polarized conduction electrons with the localized magnetic moments and will be enhanced by the large spatial variation of magnetic moments in a DW. Here, l_{DW} increases monotonically from 120 to 220nm when θ_{DW} is changed from 76° to 42° implying a monotonic change in spatial variation of magnetic moments in a DW. Therefore, the result that DWR increases with increasing θ_{DW} can be attributed to the mistracking effect. For large θ_{DW} , the DWMR is about 0.75% close to the theoretical expectation by Levy and Zhang [54].

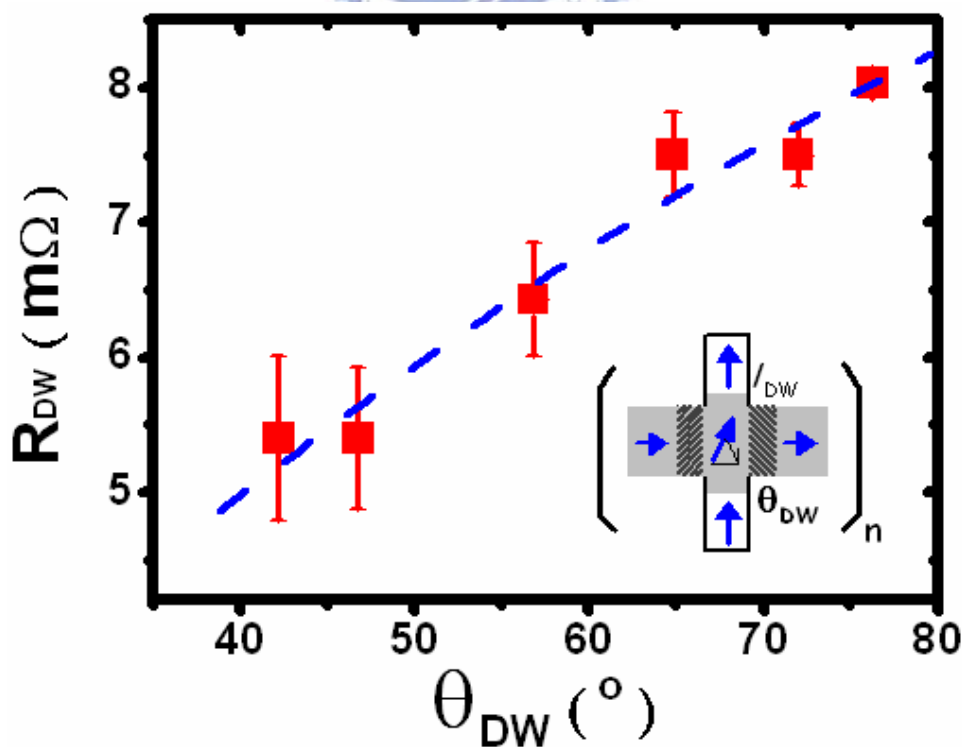


Figure 4-24: The angular dependence of the intrinsic domain wall resistance. The dashed line is a guide to the eye. The moment configuration of one segment of one typical sample is sketched in the inset.

References:

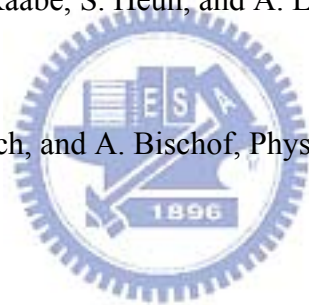
1. S. Thomas, F. Josef, K. J. Kirk, and J. N. Chapman, *J. Magn. Magn. Mat.* **175**, 193 (1997).
2. R. D. Gomez, T. V. Luu, A. O. Pak, K. J. Kirk, and J. N. Chapman, *J. Appl. Phys.* **85**, 6163 (1999).
3. E. Seynaeve, G. Rens, A. V. Volodin, K. Temst, C. Van Haesendonck, and Y. Bruynseraede, *J. Appl. Phys.* **89**, 531 (2001).
4. A.Y. Elezzabi, M. R. Freeman, and M. Johnson, *Phys. Rev. Lett.* **77**, 3220 (1996).
5. B. C. Choi, M. Belov, W. K. Hiebert, G. E. Ballentine, and M. R. Freeman, *Phys. Rev. Lett.* **86**, 728 (2001).
6. J-E. Wegrowe, D. Kelly, A. Franck, S. E. Gilbert, and J.-Ph. Ansermet, *Phys. Rev. Lett.* **82**, 3681 (1999); Y. Jaccard, Ph. Guittienne, D. Kelly, J.-E. Wegrowe, and J.-Ph. Ansermet, *Phys. Rev. B* **62**, 1141 (2000).
7. B. Leven and G. Dumpich, *Phys. Rev. B* **71**, 64411 (2005).
8. S. Goolaup, N. Singh, A. O. Adeyeye, V. Ng, and M. B. A. Jalil, *Eur. Phys. J. B* **44**, 259–264 (2005).
9. J. H. Gao, D. L. Sun, Q. F. Zhan, W. He, and Z. H. Cheng, *Phys. Rev. B* **75**, 64421 (2007).
10. K. Weerts, P. Neutens, L. Lagae, and G. Borghs, *J. Appl. Phys.* **103**, 94307 (2008).
11. R. A. B. Oliveira, S. M. Rezende, and A. Azevedo, *Phys. Rev. B* **78** 24423 (2008).
12. W. Wernsdorfer, B. Doudin, D. Mailly, K. Hasselbach, A. Benoit, J. Meier, J.-Ph. Ansermet, and B. Barbara, *Phys. Rev. Lett.* **77**, 1873 (1996).

13. J. McCord, A. Hubert, G. Schröpfer, and U. Loreit, *IEEE Trans. Magn.* **32**, 4806 (1996).
14. T. Schrefl, J. Fidler, K. J. Kerk, and J. N. Chapman, *J. Magn. Magn. Mat.* **175**, 193 (1997); X. Liu, J. N. Chapman, S. McVitie, and C. D. W. Wilkinson, *Appl. Phys. Lett.* **84**, 4406 (2004).
15. R. Ferre', K. Ounadjela, J. M. George, L. Piraux, and S. Dubois, *Phys. Rev. B* **56**, 14066 (1997).
16. M. Brands, R. Wieser, C. Hassel, D. Hinzke, and G. Dumpich, *Phys. Rev. B* **74**, 174411 (2006).
17. M. T. Bryan, T. Schrefl, D. Atkinson, and D. A. Allwood, *J. Appl. Phys.* **103**, 73906 (2008).
18. S. S. P. Parkin, M. Hayashi, and L. Thomas, *Science* **320**, 190 (2008)
19. G. Meier, M. Bolte, R. Eiselt, B. Krüger, D. H. Kim, and P. Fischer, *Phys. Rev. Lett.* **98**, 187202 (2007).
20. M. E. Sachbes and H. N. Bertram, *J. Appl. Phys.* **64**, 5832 (1988).
21. M. Lederman, R. O'Barr, and S. Schultz, *IEEE Trans. Magn.* **31**, 3793 (1995); R. O'Barr and S. Schultz, *J. Appl. Phys.* **81**, 5458 (1997).
22. M. Steiner, C. Pels, and G. Meier, *J. Appl. Phys.* **95**, 6759 (2004).
23. C. Beeli, B. Doudin, and P. Stadelmann, *Phys. Rev. Lett.* **75**, 4630 (1995).
24. Y. Yokoyama, Y. Suzuki, S. Yuasa, and K. Ando, *J. Appl. Phys.* **87**, 5618 (2000).
25. N. Vernier, D. A. Allwood, D. Atkinson, M. D. Cooke, and R. P. Cowburn, *Europhys. Lett.* **65**, 526 (2004).
26. T. G. Sorop, C. Untiedt, F. Luis, M. Kroll, M. Rasa, and L. J. de Jongh, *Phys. Rev. B* **67**, 14402 (2003).

27. Y. Endo, H. Fujimoto, S. Kumano, Y. Matsumura, I. Sasaki, Y. Kawamura, and M. Yamamoto, *J. Appl. Phys.* **103**, 07D918 (2008).
28. I. C. Lo, J. C. Wu, Lance Horng, Z. H. Wei, M. F. Lai, and C. R. Chang, *J. Appl. Phys.* **97**, 10M102 (2005).
29. C. C. Chang, Y. C. Chang, I. C. Lo, and J. C. Wu, *J. Magn. Magn. Mat.* **310**, 2612 (2007).
30. A. Aharoni, *J. Appl. Phys.* **82**, 1281 (1997).
31. M. Brands and G. Dumpich, *J. Appl. Phys.* **98**, 14309 (2005).
32. J. McCord, A. Hubert, G. Schröpfer, and U. Loreit, *IEEE Trans. Magn.* **32**, 4806 (1996); Alex Hubert, *Magnetic Domains: The Analysis of Magnetic Microstructures* (Springer-Verlag Berlin Heidelberg New York, 2000), p.462-475.
33. R. P. Cowburn, D. K. Koltsov, A. O. Adeyeye, and M. E. Welland, *J. Appl. Phys.* **87**, 7067 (2000).
34. W. C. Uhlig and J. Shi, *Appl. Phys. Lett.* **84**, 759 (2004).
35. W. Y. Lee et al., *IEEE Trans. Mag.* **35**, 3883 (1999).
36. J. F. Gregg, W. Allen, K. Ounadjela, M. Viret, M. Hehn, S. M. Thompson, and J. M. D. Coey, *Phys. Rev. Lett.* **77**, 1580 (1996).
37. L. Klein, Y. Kats, A. F. Marshall, J. W. Reiner, T. H. Geballe, M. R. Beasley, and A. Kapitulnik, *Phys. Rev. Lett.* **84**, 6090 (2000).
38. V. Gehanno, A. Marty, B. Gilles, and Y. Samson, *Phys. Rev. B* **55**, 12552 (1997).
39. C. Hassel, M. Brands, F. Y. Lo, A. D. Wieck, and G. Dumpich, *Phys. Rev. Lett.* **97**, 226805 (2006).
40. S. Lepadatu and Y. B. Xu, *Phys. Rev. Lett.* **92**, 127201 (2004).
41. T. Taniyama, I. Nalatani, T. Namikawa, and Y. Yamazaki, *Phys. Rev. Lett.* **82**,

- 2780 (1999).
42. W. L. Lee, F. Q. Zhu, and C. L. Chien, *Appl. Phys. Lett.* **88**, 122503 (2006).
 43. D. Buntinx, S. Brems, A. Volodin, K. Temst, and C. V. Haesendonck, *Phys. Rev. Lett.* **94**, 17204 (2005).
 44. K. Mibu, T. Nagahama, T. Shinjo, and T. Ono, *Phys. Rev. B* **58**, 6442 (1998).
 45. J. L. Prieto, M. G. Blamire, and J. E. Evetts, *Phys. Rev. Lett.* **90**, 027201 (2003).
 46. G. Tataru and H. Fukuyama, *Phys. Rev. Lett.* **78**, 3773 (1997).
 47. J. L. Tsai, S. F. Lee, Y. D. Yao, C. Yu, and S. H. Liou, *J. Appl. Phys.* **91**, 7983 (2002).
 48. J. L. Tsai, J. H. Hsieh, T. Y. Chen, S. H. Liou, S. F. Lee, and Y. D. Yao, *Phys. Stat. Sol b* **241** 1581 (2004).
 49. U. Rüdiger, J. Yu, S. Zhang, A. D. Kent, and S. S. P. Parkin, *Phys. Rev. Lett.* **80**, 5639 (1998).
 50. Y. B. Xu, C. A. F. Vaz, A. Hirohata, H. T. Leung, C. C. Yao, and J. A. C. Bland, *Phys. Rev. B* **61**, R14901 (2000).
 51. C. Yu, S. F. Lee, J. L. Tsai, E. W. Huang, T. Y. Chen, Y. D. Yao, Y. Liou, and C. R. Chang, *J. Appl. Phys.* **93** 8761 (2003).
 52. A. O. Adeyeye, and M. E. Welland, *J. Appl. Phys.* **92** 3896 (2002).
 53. R. Danneau, P. Warin, J. P. Attane', I. Petej, C. Beigne', C. Fermon, O. Klein, A. Marty, F. Ott, Y. Samson, and M. Viret, *Phys. Rev. Lett.* **88** 157201 (2002).
 54. P. M. Levy and S. Zhang, *Phys. Rev. Lett.* **79**, 5110 (1997).
 55. J. F. Gregg, W. Allen, K. Ounadjela, M. Viret, M. Hehn, S. M. Thompson, and J. M. D. Coey, *Phys. Rev. Lett.* **77**, 1580 (1996).
 56. H. Sato, R. Hanada, H. Sugawara, Y. Aoki, T. Ono, H. Miyajima, and T. Shinjo, *Phys. Rev. B* **61**, 3227 (2000).

57. M. Kläui, C. A. F. Vaz, J. Rothman, J. A. C. Bland, W. Wernsdorfer, G. Faini, and E. Cambril, *Phys. Rev. Lett.* **90**, 97202 (2003).
58. M. Hayashi, L. Thomas, Ya. B. Bazaliy, C. Rettner, R. Moriya, X. Jiang, and S. S. P. Parkin, *Phys. Rev. Lett.* **96**, 197207 (2006).
59. U. Ebels, A. Radulescu, Y. Henry, L. Piraux, and K. Ounadjela, *Phys. Rev. Lett.* **84**, 983 (2000).
60. U. Rüdiger, J. Yu, L. Thomas, S. S. P. Parkin, and A. D. Kent, *Phys. Rev. B* **59**, 11914 (1999).
61. This code to calculate the magnetization configuration is described on <http://math.nist.gov/oommf>.
62. T. Haug, C. H. Back, J. Raabe, S. Heun, and A. Locatelli, *Appl. Phys. Lett.* **86**, 152503 (2005).
63. P. O. Jubert, R. Allenspach, and A. Bischof, *Phys. Rev. B* **69**, 220410 (2004).



5 Conclusions and Future work

5-1 Summary

We have studied two related topics in a ferromagnetic mesoscopic system. First one is the magnetization reversal process of an individual wire and second one is the intrinsic scattering in domain wall regions.

In the first topic, magnetization reversal process and domain structure in Permalloy (Py) planar wires were systematically investigated using magnetoresistance (MR) measurement and in-field magnetic force microscopy (MFM). According to remanent domain structure, samples could be classified to three groups in terms of geometrical parameters such as the length and the aspect ratio. For wires of $20\mu\text{m}$ long, a multi-domain is observed as the aspect ratio is smaller than 10. When the aspect ratio is larger than 40, the characteristics of the single domain are present. Between them, an intermediate region that two closure domains form in both ends in addition to the most main body of single domain is evident. Their geometrical factors induced remanent configuration transition is roughly in agreement with the Aharoni model. Subsequently, we show a close relationship between magneto-transport and domain structure in Py wires. We find that anisotropic magnetoresistance (AMR) plays a major role in magneto-transport of Py wires.

We analyzed the angular dependent MR curves for wires in single domain states. In the process from the saturation to the remanence, the reversibly bell shaped MR curve can be well described by combining AMR and coherent rotation. The uniaxial anisotropy constant (K_u) can be quantified by the fit of transverse magnetoresistance (TMR) to the Stoner–Wohlfarth model. For a $20\mu\text{m}$ long Py wire with widths from 0.1

to $2\mu\text{m}$, K_u decreases from 10.5 to $1.3 \times 10^5 \text{erg/cm}^3$. For a wire of width $1.2 < w < 2\mu\text{m}$, K_u is about the same $\sim 1.3 \times 10^5 \text{erg/cm}^3$. With decreasing wire width, K_u increases rapidly for $w < 1.2\mu\text{m}$. It seems that there are two distinct regimes. For the regime where K_u is independent of wire width, in-field MFM images indicate that closure domains in both ends expand through the whole volume with a slight increase of magnetic field in the opposite direction. Before reaching H_{sw} , the magnetic configuration of the whole wire is mesoscopically homogeneous, confirmed by the MR behaviors in different segments of the wire. A 180° cross-tie like wall appears near H_{sw} in consistence with the maximum deviation of LMR is almost 20~30% of AMR effect at H_{sw} . For a very narrow wire ($w < 0.5\mu\text{m}$), remanent state is a single domain with moments along the long axis and two stray fields at end points only (two contrast spots shown in the MFM images). MFM images show that the moment of the whole wire always lies along the easy axis and the only change of the moment is the 180° rotation at the switching. The LMR is almost zero and the maximum deviation at H_{sw} is less than 0.5%. For an intermediate wire ($0.6 < w < 1.2\mu\text{m}$), there are closure domains in both ends similar to the wider one and the end domain does not extend to the whole wire unlike the wider one. In-field MFM images indicate that the end domain extends at most about one quarter of the wire before H_{sw} in consistence with the spatial dependent LMR. The maximum deviation of LMR in the near-end regime is about 15% while about 0.5% in the center and arm regimes.

The reversal behavior at the switching field (H_{sw}) has been investigated using angular dependence of MR measurement. Comparing with the Aharoni models, the reversal of a single domain state for wire of $w < 1.2\mu\text{m}$ is found to be completed via the local nucleation together with the propagation of the domain wall.

The aim of the second topic is to study the intrinsic scattering when electrons

pass through a domain wall. For this purpose, the artificial Néel walls were created in the centipede-like Py structures which consist of a central wire with numerous orthogonally bisecting finger wires. Longitudinal magnetoresistance (LMR) shows a single jump characterizing the switching of the central wire. TMR curve demonstrates a number of steps, which is the same as the number of fingers. The abrupt resistance drop is ascribed to the switching of each finger wire, which is confirmed by the in-field MFM images and the Planar Hall effect measurement. Due to the shape anisotropy, there is a stable periodic domain configuration of alternating pitch and junction. In order to obtain the tilted angle of the moments at the junction, the Planar Hall effect measurement was employed. The obtained tilted angle is close to that determined by anisotropy constants of both wires. A model of resistance-in-series was developed to analyze both MRs and the intrinsic domain wall resistance can be estimated. We find that domain wall resistance is positive and decreases with decreasing the angle. The result is indeed consistent with the prediction by consideration of the spin-mistracking effect.

5-2 Future work

The investigation of mesoscopically ferromagnetic systems with magnetization reversal process and magneto-transport properties is far from over. A fundamental desire to understand the picture of the reversal process and the physics which influences the transport properties have brought us a remarkable way over the past decades. In this work we have found that the anisotropic energy plays a major role in the reversal process. Following would be asked the question that what happen in other materials or different shape of wire ends. For a polycrystalline soft magnetic material,

the shape anisotropy dominates the anisotropic energy. The phenomenon of the end domain expansion during the reversal may be expected in the low saturated magnetization material such as Ni. In contrast, the end domain expansion is expected to be suppressed in the high saturated magnetization material such as Co. In addition, the nucleation of the end domain is strongly affected by the shape of wire ends. There have been a few studies of the effects of the shape and size of elements on switching properties [1-3]. However, there is lack of a complete discussion in the nucleation of the end domain.

In recent years, much effort has been put into the identification of the spin torque effect in small magnetic elements since it is a potential candidate for the next generation of magnetic memory. Parkin has demonstrated a practical pattern using the pulse spin-polarized current to move domain walls to realize that [4]. However, In order to build a stable bit, domain walls are located at the periodic pinning sites, meaning the critical current densities needed to move the domain wall might be too high for practical use. Thomas reported that a domain wall can be described as if the domain wall has a mass [5,6]. Then, domain walls are grabbed by pinning sites, just like an oscillator confined in a potential well resonates at a natural frequency. When passing a current pulse with particular duration time matched to this frequency, the domain wall can be excited out of the pinning sites by resonance with the significant avoidance of high critical current.

In our centipede like structure, the moment at the junction is influenced by the induced anisotropy generated from the finger wires. The strength of pinning potentials can be determined by comparing the temperature dependence of switching fields with the thermal assisted model. In addition, for one sample moments at the junction have been successfully switched by passing a steady current through the central wire.

Because the central wire is so wide that the required strength of passing current is too large even if an external magnetic field is applied to assist switching. The large current induced joule heating would raise sample's temperature up, leading to the confusion of spin torque effect with thermal activation. Therefore, in order to efficiently eliminate the thermal problem, decreasing wire widths and passing a pulse current are practicable in the further study. Furthermore, the influence of the duration of a pulse current on the domain wall resonance is worth to study.



References:

1. K. Shigeto, T. Shinjo, and T. Ono, *Appl. Phys. Lett.* **75**, 2815 (1999).
2. M. Herrmann, S. McVitie, and J. N. Chapman, *J. Appl. Phys.* **87**, 2994 (2000).
3. X. Liu, J. N. Chapman, S. McVitie, and C. D. W. Wilkinson, *J. Appl. Phys.* **96**, 5173 (2004).
4. S. S. P. Parkin, M. Hayashi, and L. Thomas, *Science* **320**, 190 (2008).
5. L. Thomas, M. Hayashi, X. Jiang, R. Moriya, C. Rettner, and S. S. P. Parkin, *Nature* **433**, 197 (2006).
6. L. Thomas, M. Hayashi, X. Jiang, R. Moriya, C. Rettner, and S. S. P. Parkin, *Science* **315**, 1553 (2007).



Curriculum Vitae

Personal Data

Name: Ting-Yi Chung (鍾廷翊)

Day of Birth: 1979/04/19

Gender: Male

E-mail address: siky.ep86@nctu.edu.tw

Education

- ◆ 1997/09~2001/06: B. S. degree in Electrophysics, National Chiao Tung University, Hsinchu, Taiwan.
- ◆ 2001/09~2003/06: M. S. degree in Electrophysics, National Chiao Tung University, Hsinchu, Taiwan.
- ◆ 2003/09~2009/05: Ph. D. degree in Electrophysics, National Chiao Tung University, Hsinchu, Taiwan.

Publications

- T. Y. Chung and S.Y. Hsu, "Magneto-transport flipping induced by surface oxidation in Co films", *Journal of Physics: conf. ser.* **150**, 042063 (2009).
- T. Y. Chung and S.Y. Hsu, "The angular dependence of Néel wall resistance by magnetotransport in the centipedelike Permalloy structures", *Journal of Applied physics* **105**, 07D123 (2009).
- T. Y. Chung and S.Y. Hsu, "Magnetization reversal in single domain Permalloy wires probed by magnetotransport", *Journal of Applied physics* **103**, 07C506 (2008).
- W. J. Chang, C. C. Hsieh, T. Y. Chung, S. Y. Hsu, K. H. Wu, T. M. Uen, Y. S. Gou, and J. Y. Juang, "Fabrication and X-ray absorption Na_xCoO_2 spectroscopy in layered cobaltate thin films", *Journal of Magnetism and Magnetic Materials* **310**, E335 (2007).
- W. J. Chang, C. C. Hsieh, T. Y. Chung, S. Y. Hsu, K. H. Wu, T. M. Uen, Y. S. Gou, and J. Y. Juang, "Fabrication and Low Temperature Thermoelectric Properties of Na_xCoO_2 ($x=0.68$ and 0.75) Epitaxial Films by the Reactive Solid-Phase Epitaxy", *Applied Physics Letter* **90**, 061917 (2007).
- T. Y. Chung and S.Y. Hsu, "Detection of the domain structure change using magnetotransport for a series of circular Permalloy dots", *Journal of Applied physics* **99**, 08B707 (2006).